UNIVERSIDAD
NACIONAL
DE COLOMBIA

INTEGRATED PHOTONIC CIRCUITS BASED ON PLASMONIC MODES IN MICROSTRUCTURED OPTICAL FIBERS

Nelson Darío Gómez Cardona

Universidad Nacional de Colombia – Sede Medellín
Facultad de Ciencias
Escuela de Física
Medellín, Colombia
2020

INTEGRATED PHOTONIC CIRCUITS BASED ON PLASMONIC MODES IN MICROSTRUCTURED OPTICAL FIBERS

CIRCUITOS FOTÓNICOS INTEGRADOS BASADOS EN MODOS PLASMONICOS EN FIBRAS ÓPTICAS MICRO-ESTRUCTURADAS.

Nelson Darío Gómez Cardona

Tesis presentada como requisito parcial para optar al título de:
Doctor en Ciencias -Física

Director:
Ph.D. Pedro Ignacio Torres Trujillo

Grupo de Investigación:
Fotónica y Optoelectrónica

Universidad Nacional de Colombia – Sede Medellín
Facultad de Ciencias
Escuela de Física
Medellín, Colombia
2020

Resumen

Título en español: Circuitos Fotónicos Integrados Basados en Modos Plasmónicos en Fibras Ópticas Micro-Estructuradas.

Esta tesis se consideran los fenómenos asociados con los modos de plasmón excitados en fibras ópticas micro-estructuradas recubiertas con películas metálicas de espesor nanométrico, con un interés particular en los modos de plasmón de orden superior excitados en la película metálica y su acoplamiento con los modos de propagación de la fibra óptica. También se aborda el estudio de estructuras simétricas, en las que el medio que rodea la película metálica es homogéneo, y de estructuras antisimétricas, en las que el medio superior e inferior son diferentes. En este último caso se utilizaron estructuras multicapa porque ofrecen la posibilidad de modificar las propiedades de propagación de los modos plasmón excitados y de sintonizar la condición de resonancia, mejorando el rendimiento de los dispositivos. También se consideró la excitación de los modos plasmónicos en fibras ópticas micro-estructuradas que contienen agujeros llenos de metal, con paredes alisadas, evitando la presencia de modos localizados en esquinas formadas por inhomogeneidades. El modelado y la comprensión de estas estructuras facilita tener las condiciones para excitar modos plasmónicos híbridos, que parecen ser ideales para los circuitos fotónicos.

Palabras clave: fibra óptica micro-estructurada; fibra de cristal fotónico; guía de ondas ópticas; polaritón de plasmón de superficie; resonancia de plasmón de superficie; sensor de fibra óptica; dispositivos de fibra óptica.

Abstract

Título en inglés: Integrated Photonic Circuits Based on Plasmonic Modes in Microstructured Optical Fibers.

This thesis considers the phenomena associated with plasmon modes excited in MOFs, with a particular interest in higher-order plasmon modes and their coupling with propagation modes of the MOF. These multiple couplings, according to our prior knowledge, are the cause of the multiple resonances that occur in the transmittance spectrum of the SC-MOF. At this point, the study of symmetrical structures, in which the medium surrounding the metal film is homogeneous, and antisymmetric structures, in which the upper and lower media are different, was also addressed, but in these cases, multilayer structures were used because of it offers the possibility of modifying the propagation properties of the excited plasmon modes and tuning the resonance condition, improving the performance of the devices. Following this line of analysis, the excitation of plasmon modes in MOFs containing metal-filled holes was also considered. To facilitate the modeling of the structure and a better understanding of the associated phenomena the metal-filled holes were considered as nanowires with smoothed walls, avoiding the presence of localized modes in corners formed by inhomogeneities. Overall, modeling and understanding these structures was possible obtaining conditions for exciting hybrid modes, which appear to be ideal for photonic circuits.

Keywords: microstructured optical fiber; photonic crystal fiber; optical waveguide; surface plasmon polariton; surface plasmon resonance; optical fiber sensor; optical fiber devices.

List of symbols and abbreviations

Latin character

Symbol	Quantity	Unit SI
a	Fiber core radius	m
A	Area	m^2
B	Magnetic induction	N/A.m
c	Speed of light in vacuum	m/s
d	Thickness of waveguide	m
D	Electric displacement	C/m^2
E	Electric Field	V/m
E_z	The longitudinal component of the electric field	V/m
H	Magnetic Field	A/m
H_z	The longitudinal component of the magnetic field	A/m
i	The imaginary number	dimensionless
k	Wavevector	m^{-1}
k_{sp}^{r}	Resonance condition	m^{-1}
L_{SP}	Length of propagation	m
L_{pd}	Length of penetration into the dielectric	m
L_{pm}	Length of penetration into the metal	m
M	Magnetization vector	A/m
n	Refractive index, real part	1

Symbol	Quantity	Unit SI
n_{eff}	Effective refractive index	1
r	Position	m
R	Reflectance	1
r_{lj}	Reflection coefficients	1
S_n	Sensitivity	nm/RIU
T	Transmittance	1
t	Time	s

Greek character

Symbol	Quantity	Unit SI
α	Attenuation factor	dB/km
β	Propagation constant	m^{-1}
ε	Dielectric permittivity	F/m
ε_0	Vacuum permittivity	F/m
ε_r	Relative permittivity	1
λ	Wavelength	m
μ_0	Magnetic permeability	N/A^2
μ_0	Vacuum permeability	N/A^2
μ_0	Relative permeability	1
θ	Incidence angle	rad
ω	Angular frequency	Hz
χ_e	Electric susceptibility	dimensionless
χ_m	Magnetic susceptibility	dimensionless

1. INTRODUCTION

The emergence of optical fibers and their extensive use in the transmission of light signals through them brought new areas of research. Analytical models had been obtained that explain the properties of light propagation in optical waveguides, particularly where its cross-section has special shapes: planar [1], rectangular [2], and circular [3]. With these models, it is possible to predict, for each type of waveguide, the spatial distributions of electric and magnetic fields, known as propagation modes. In particular, these models allow us to know the modes that are excited by the electromagnetic field of the light beam coupled to the waveguide [4]. The complex propagation constant of each mode provides information about their optical properties [4], including the main linear phenomena, attenuation and dispersion [5], and other higher-order dispersive phenomena that cause the appearance of non-linear effects [5]. Knowing and understanding the main characteristics of waveguides have allowed the development, in recent decades, of a high number of photonic devices used in optical communications technology such as directional couplers [6], [7], circulators [8], [9], optical filters [10], polarizers [11]–[13], array waveguides [14], multiplexers [15], [16]; and as transducer medium, intrinsic or extrinsic, in sensors applied to the measurement of physical parameters. These sensors use the fact that the variations in the shape of waveguide [17] (deformations, macro-bendings), localized pressure [18] (micro-bendings), or pressure distributed over the outside area of waveguide [19], create losses because the light is radiated out of the waveguide, enabling to measure parameters such as strength [20], pressure [21], displacement [22], and vibration [23], among others.

A major advance in the technology of the waveguides consists of adding a metal layer that has a thickness of some nanometers near to the waveguide core. This film, generally made of noble metals such as gold (Au), silver (Ag), aluminum (Al), platinum (Pt), among others, facilitates the emergence of other phenomena known as Surface Plasmon Polariton (SPP), which can be modeled as propagation modes in a metal film "sandwiched" between two dielectrics and Surface Plasmons (SPs) [24]. Unlike SPs, SPPs are surface waves confined close to a metal/dielectric interface. Due to the complex dielectric constant of metal, the modal propagation constants in the waveguide will have a real part, which accounts for the phase shifts, and the imaginary part which contains the information about attenuation [25]. Besides, the SPPs may be short or long, depending on how strong is their confinement and the value of the attenuation parameter [25]. Recently, it has been proposed structures capable of combining the properties of confinement beyond the limit of diffraction of the SPP with

low levels of attenuation. In this case, the resulting propagation modes are called Hybrid Plasmonic-Photonic Modes, or simply Hybrid Plasmonics Modes (HPM) [25]. The properties of these modes have been explored and two key performance factors were established: propagation distance and confinement factor [26]; this last one is defined as the lateral penetration for integrated optics devices and the vertical penetration length for devices used as sensors.

To reduce the propagation losses of plasmon modes and to make them interact with the modes of the waveguides, several structures have been proposed, such as plasmonic waveguides [27], [28], channel plasmon polariton waveguides [29]–[32], edge plasmonic waveguides [33], [34], metal-dielectric-metal waveguides [35], and hybrid long-range surface plasmon waveguides [25]. Hybrid modes in waveguides reach propagation lengths close to 1 mm, which are mainly used in couplers [36], polarizers [37], modulators [38]. Because the hybrid modes have large penetration lengths, they can reach regions beyond the propagation region, so they are also used in sensors [39]–[42]. These kinds of modes also possess a unique feature: metallic waveguide also can be used to transmit electrical signals and modulating the intensity of the light, that is engineering completely integrated photonic circuits, avoiding the problems of attenuation and losses of conventional devices. With the help of other phenomena, as nonlinearities [43], the electro-optic effect [44], and thermo-optic effect, devices as switches and modulators to encoding optical signals have been built [45]. All this is accompanied by low power consumption and a significant reduction in the size of the devices.

However, most of the schemes proposed, both on optical communications and optical sensing, are based on planar waveguides, requiring the use of complicated mechanical systems for coupling the light into devices. One way to overcome this problem is to use micro-structured optical fibers (MOFs). These fibers, unlike optical photonic crystal fibers, have larger holes whose dimensions have an order of magnitude higher the wavelength of interest; for example, in fibers with circular holes used for optical communications, the radius is a few tens of micrometers [46]. Recent works reported suspended core MOFs (SC-MOFs) with two holes [47], three holes [48], and four holes [49], in which have been excited surface plasmon. Because in the SC-MOF the modal field is highly confined and that in principle the surfaces adjacent to the core can be considered approximately flat, these are susceptible to be used as support for the design and manufacture of devices based on plasmonic modes of short and long-range, and hybrid plasmonic-photonic modes of long-range. To the best of our knowledge, these new structures have not been explored yet.

According to the above, this thesis considers the phenomena associated with plasmon modes excited in MOFs, with a particular interest in higher-order plasmon modes and their coupling with propagation modes of the MOF. These multiple couplings, according to our prior knowledge [49], are the cause of the multiple resonances that occur in the transmittance spectrum of the SC-MOF. At this point, the study of symmetrical structures, in which the medium surrounding the metal film is homogeneous, and antisymmetric structures, in which the upper and lower media are different, was also addressed, but in these cases, multilayer structures were used because of it offers the possibility of modifying the propagation properties of the excited plasmon modes and tuning the resonance condition, improving the performance of the devices. Following this line of analysis, the excitation of plasmon modes in MOFs containing metal-filled holes was also considered. To facilitate the modeling of the structure and a better understanding of the associated phenomena the metal-filled holes were considered as nanowires with smoothed walls, avoiding the presence of localized modes in corners formed by inhomogeneities. Overall, modeling and understanding these structures was possible obtaining conditions for exciting hybrid modes, which appear to be ideal for photonic circuits [50], [51].

2. STATE OF THE ART

2.1 Microstructured Optical Fibers

Photonic Crystal Fibers (PCF) [46] are a class of optical fiber in which the central region (solid or hollow) is surrounded by an array of air holes. In the first case, with a solid central region, the confinement mechanism of the light is the same index-guiding principle of the conventional fibers; while in the second case with the hollow central region, the confinement mechanism of the light is given by bandgap effects [52], see Figure 2-1 (a). Of course, the propagation properties of light in these types of fibers are determined by the refractive index of the solid region (in the case of the solid core PCF), the geometric properties of the micro holes, and its distribution over the fiber cross-section.

Now, the concept of the PCFs has evolved to new structures and distributions of the micro holes, which currently are called microstructured optical fibers, see Figure 2-1 (b). Due to the complexity of these structures and their lack of azimuthal symmetry, it is impossible to separate the states of polarization and found an analytical solution similar to that obtained for optical fibers with cylindrical symmetry [5], [53].

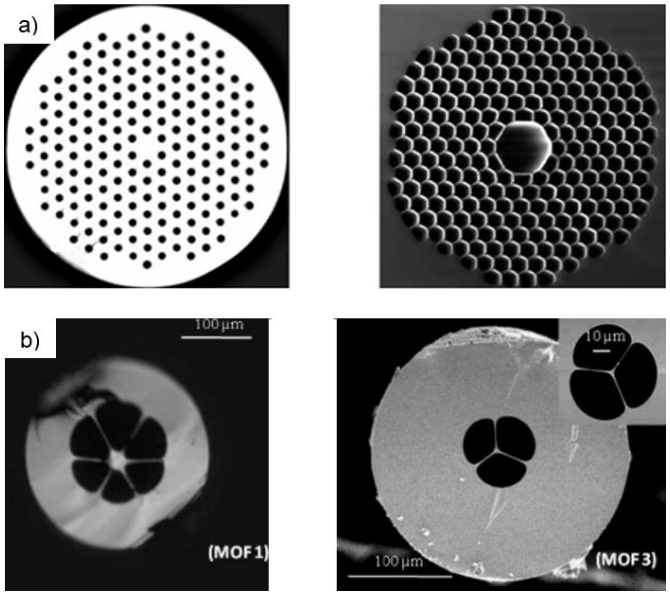

Figure 2-1. a) Photonic Crystal Fiber PCF [64]; b) Microstructured Optical Fiber MOF [65]

To find the propagation constants of modes in this type of fiber, it is necessary to do approaches based on equivalent structures such as the approximation of effective refractive index [54], [55], or techniques of modal decomposition based on basic functions like sine functions, Hermite-Gauss functions and cylindrical functions [56]–[60]. Models based on modal decomposition are effective if the holes are circular and with some type of symmetry on the transversal axis *(x, y)* of the fiber. More complex structures require the use of numerical methods such as the finite element method, FEM [61], [62]. This method discretizes the cross-section into small regions (elements), and each one of the variables is evaluated in the nodes (points of the union of the elements). Thus, the contributions of all elements are assembled in a sparse matrix whose eigenvalues correspond to the propagation constants of the bounded modes of the structure. To evaluate the resonance condition and how it is affected by external disturbances, one must carry out a transmittance spectrum at the output end of the fiber. As the wavelength of resonance is characterized by having an attenuation band, changes in the external environment are determined indirectly from the shifts of the attenuation band, as shown in Figure 2-2.

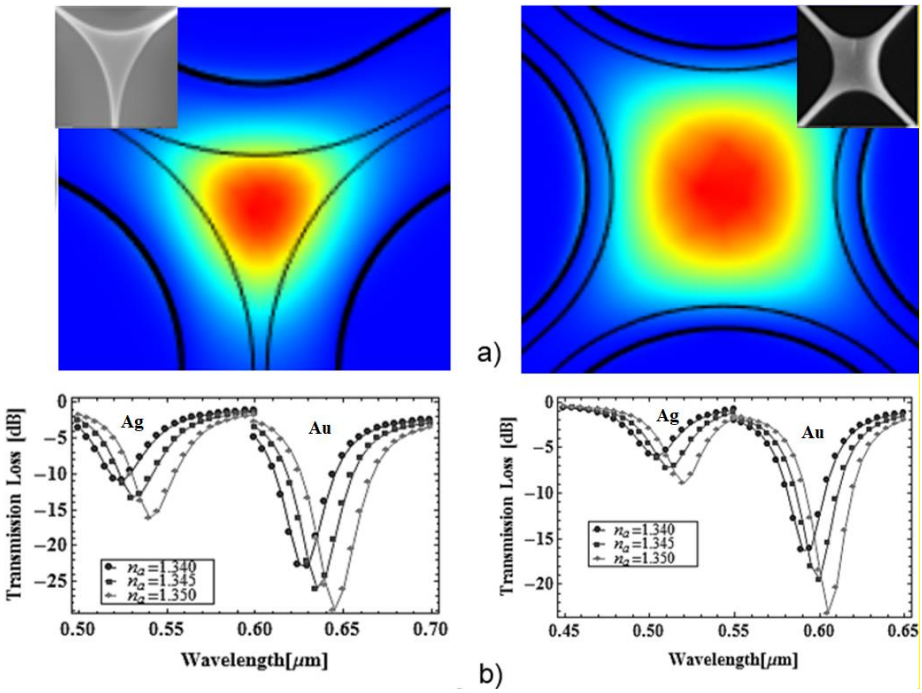

Figure 2-2. a) Three-hole and four-hole MOFs and b) SPR transmission loss [49] (Comsol ®) [63]

2.2 Hybrid Long Range Surface Plasmon Polaritons H-LRSPPs.

When we have a metal film (nanometer in thickness) confined by two dielectrics, as is shown in Figure 2-3, it is possible to excite two modes, known as symmetrical (short-range) and antisymmetric (long-range) surface plasmons, SRSPP and LRSPP, respectively. The main problem with this 1-D structure is that since the metal film has an infinite width *w*, the SPP modes will spread laterally from the excitation point [64], [65]. However, when *w* is finite, the SPPs are strongly confined in both directions [50], [51], [66], i.e, in the transverse plane to the direction of propagation. In this 2-D structure, known as a strip, the plasmon modes travel confined without variations in the direction of propagation, therefore their properties and characteristics remain invariant. Excited plasmon modes in the symmetrical structure, i.e., when the dielectric surrounding the metallic waveguide is equal on both sides, $\varepsilon_1 = \varepsilon_3$, have been extensively studied. It has been shown experimentally the existence of LRSPP modes with attenuation close to 1.0 dB/cm [67].

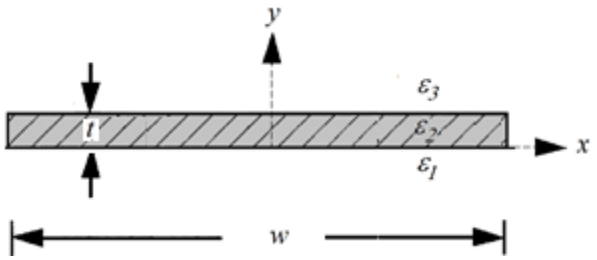

Figure 2-3. Strip metallic waveguide. Adapted from [50]

Symmetric structures supporting LRSPP modes are used with dielectric guides for processing [68], routing [69], and transmitting optical communications signals [70]. However, the coupling length of the dielectric waveguides is high when is compared to the propagation length of the LRSPP. This, together with the strong confinement of the LRSPP, leads to low coupling energy between modes. Asymmetric structures, where $\varepsilon_1 \neq \varepsilon_3$, have been also studied theoretically and experimentally [71], [72].

If the metal waveguide is immersed into or close to a dielectric medium that behaves as an optical waveguide, then the propagation constant of modes could match the propagation constant of the SPP modes, forming hybrid modes [73]–[75]. This kind of modes have two important features: it is able to confine the light beyond the diffraction limit and also to have low attenuation, therefore they have high potential in the construction of integrated photonic circuits for the transmission of optical signals, and to build active devices such as amplifiers [76] and lasers [36], [77]–[81], and passive devices for example splitters [37], [82], polarizers

[40], [83], sensors [84], among others. To find the hybrid modes in planar structures it is possible to use scalar numerical methods as the approximation of equivalent effective refractive index [85], Marcatili method [50], [86]; or vector numerical methods such as the method of lines MoL described in [61], [87] and the finite element method [74], [88], [89].

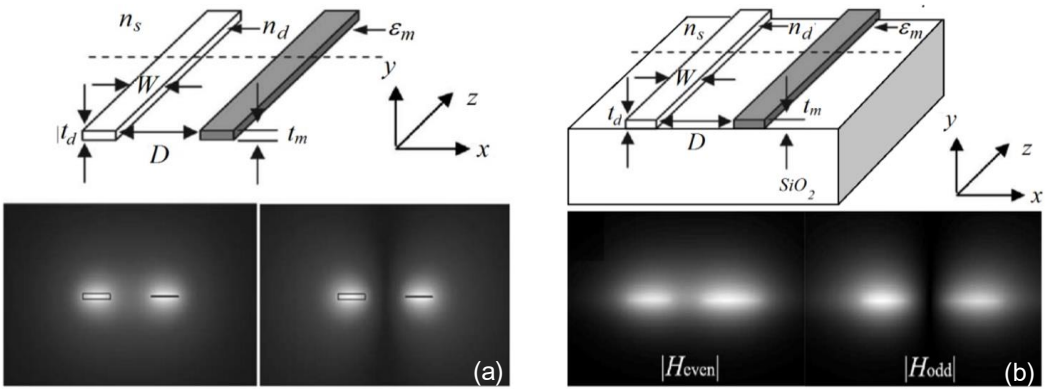

Figure 2-4. Hybrid couplers (top) and magnetic field amplitude (bottom). a) symmetric structure. Adapted from [70]. b) asymmetric structure. Adapted from [80]

2.3 Channel Plasmon Polaritons CPPs

In this kind of structure, the radiation is concentrated in a V-shaped channel [88]. Figure 2-5 shows the two basic structures, V groove channels of metallic materials coated with a thin dielectric film over which are deposited the nanoparticles, nano-wires or nano-strips or air-filled metal channels.

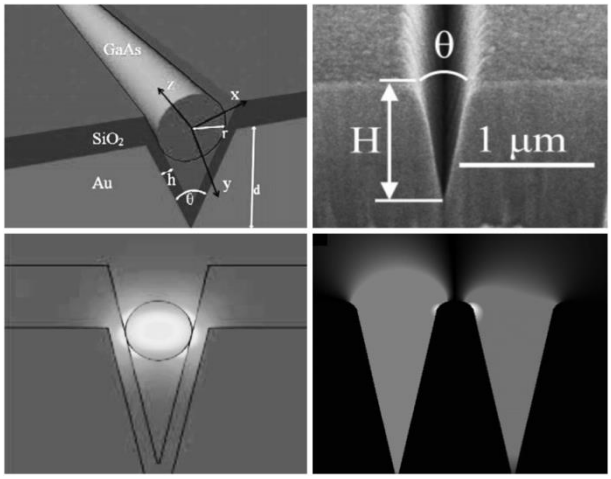

Figure 2-5. Channel waveguides (top).Magnetic field amplitude (bottom). Adapted from [84], [90]

2.4 Dielectric Loaded Surface Plasmon Polaritons DLSPPs

They are H-LRSPPs formed by planar waveguides with abrupt variations in the transverse plane to the direction of propagation, for example, combinations of endless films with rectangles, either metal, as in Figure 2-6(a), or dielectrics with high refractive index value as in Figure 2-6(b). In this type of structure, the radiation is confined in the metallic region with greater thickness and coupled to the dielectric material. H-LRSPP excitations have greater propagation length and better properties of confinement than structures such as nano-strips [91], so they support bendings or other modifications in the direction of propagation. Because of these characteristics, they are ideals for applications in photonic circuits [92].

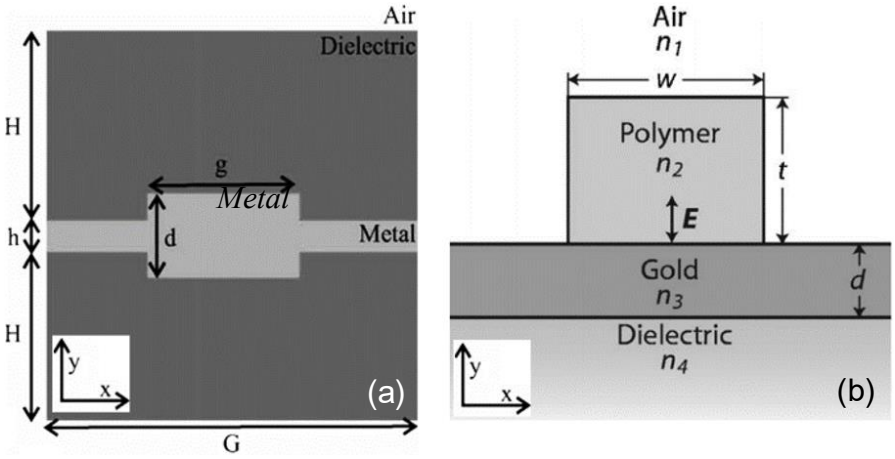

Figure 2-6. Dielectric Loaded Surface Plasmon Polaritons DLSPPs. Adapted from [84]

3. THEORETICAL BACKGROUND

3.1 Maxwell Equations

In a dielectric medium, the Maxwell equations for time-varying fields formulated in the differential form are given by:

$$\nabla \cdot \mathbf{D} = 0 \tag{3.1a}$$

$$\nabla \cdot \mathbf{B} = 0 \tag{3.1b}$$

$$\nabla \times \mathbf{H} = \mathbf{J} + \frac{\partial \mathbf{D}}{\partial t} \tag{3.1c}$$

$$\nabla \times \mathbf{E} = -\frac{\partial \mathbf{B}}{\partial t} \tag{3.1d}$$

For a complete formulation, the following expressions are needed for describing the macroscopic properties of a medium under the influence of an applied electromagnetic field:

$$\mathbf{D} = \varepsilon_0 \mathbf{E} + \mathbf{P} \tag{3.2a}$$

$$\mathbf{B} = \mu_0 \left(\mathbf{H} + \mathbf{M} \right) \tag{3.2b}$$

$$\mathbf{J} = \sigma \mathbf{E} \tag{3.2c}$$

The electric displacement vector **D** describes the changes of the Electric field **E** within the medium because of the presence of free and bound charges. **P** is the electric polarization vector, which describes how the medium is polarized under an electric field. The Magnetic flux density denoted by **B** shows as the medium is permeated by the magnetic field intensity **H**. **M** is the magnetization vector describing how the medium is magnetized. If the medium is linear, the polarization and magnetization vectors are linear relations on the electric field and magnetic field and are given as, $\mathbf{P} = \chi_e \mathbf{E}$ and $\mathbf{M} = \chi_m \mathbf{H}$. The adimensional parameters χ_e and χ_m are, respectively, the electric susceptibility and the magnetic susceptibility. Thus, in a linear media, the relations described above can be re-written as:

$$\mathbf{D} = \left(1 + \chi_e\right) \varepsilon_0 \mathbf{E} = \varepsilon_r \varepsilon_0 \mathbf{E} \tag{3.3a}$$

$$\mathbf{B} = \left(1 + \chi_m\right) \mu_0 \mathbf{H} = \mu_r \mu_0 \mathbf{H} \tag{3.3b}$$

ε_0 = is the dielectric permittivity of vacuum, μ_0 = the magnetic permeability of vacuum, ε_r is the relative dielectric permittivity, μ_r the relative magnetic permeability, and σ the electric conductivity.

Assuming that electric and magnetic fields can be written as:

$$\mathbf{E} = \mathbf{E}_0(\mathbf{r}) e^{i\mathbf{k}.\mathbf{r}} e^{-j\omega t} \tag{3.4a}$$

$$\mathbf{H} = \mathbf{H}_0(\mathbf{r}) e^{i\mathbf{k}.\mathbf{r}} e^{-j\omega t} \tag{3.4b}$$

Besides, taking into account that in a dielectric material $\varepsilon_r = n^2$ and by using the Maxwell equations is possible to get the Helmholtz equation:

$$\nabla \times (\nabla \times \mathbf{E}) - k_0^2 n^2 \mathbf{E} = 0 \tag{3.5}$$

In the modal analysis, the complex eigenvalues of this equation describe the complex propagation constant $\Gamma = i\beta - \delta$. where $\beta = k_0 \operatorname{Re}\{n_{eff}\}$ is the phase constant, and $\delta = k_0 \operatorname{Im}\{n_{eff}\}$ describe the confinement losses.

3.1.1 Sellmeier coefficients

Often, it is convenient to express the optical properties of materials by using dispersion equations. The well known Sellmeier equations, describe the refractive index $n(\lambda)$ of a transparent material as a function of wavelength λ, it can be written in the general form as [93]:

$$n(\lambda) = \sqrt{1 + \sum_i \frac{A_i \lambda^2}{\lambda^2 - B_i^2}} \tag{3.6}$$

where λ is the wavelength of vacuum expressed in μm. The terms A_i and B_i are named the Sellmeier coefficients. Sellmeier coefficients for fused silica and water used in this thesis are listed in Table 3-1.

Table 3-1. Sellmeier Coefficients for Fused Silica and water.

Sellmeier Coefficients	Fused Silica	Water
A_1	0.696166300	0.56670
A_2	0.407942600	0.17320
A_3	0.897479400	0.020995
A_4	--	0.11252
B_1	0.0684043	$(5.08415\text{x}10^{-3})^{1/2}$
B_2	0.1162414	$(1.81848\text{x}10^{-2})^{1/2}$
B_3	9.896161	$(2.62544\text{x}10^{-2})^{1/2}$
B_4	--	$(1.07384\text{x}10^{1})^{1/2}$

Table 3-2. Drude-Lorentz parameters for gold

Parameter [Unity]	Value
ε_∞	1.54
λ_p [nm]	143
γ_p [nm]	14500
A_1	1.27
ϕ_1 [rad]	$-\pi/4$
λ_1 [nm]	470
γ_1 [nm]	1900
A_2	1.1
ϕ_2 [rad]	$-\pi/4$
λ_2 [nm]	325
γ_2 [nm]	1060

On the other hand, in a metallic material, the Drude-Lorentz model is used to obtain the relationship between the relative permittivity $\varepsilon_r(\lambda)$ an the wavelength λ [94]:

$$\varepsilon_{\mathrm{Au}}(\lambda)=\varepsilon_{\infty}-\frac{1}{\lambda_p^2\left(1/\lambda^2+i/\gamma_p\lambda\right)}+\sum_{j=1,2}\frac{A_j}{\lambda_j}\left\{\frac{\exp\left(i\varphi_j\right)}{\left(1/\lambda_j-1/\lambda-i/\gamma_j\right)}+\frac{\exp\left(-i\varphi_j\right)}{\left(1/\lambda_j+1/\lambda+i/\gamma_j\right)}\right\} \tag{3.7}$$

The right term describes the Drude contributions and the second the interband transitions. The complex refraction index is obtained through the relationship $\sqrt{\varepsilon_r}=n+ik$. Table 3-2 shows the parameters used to obtain the optical properties of gold.

3.2 Finite Element Method

The finite element method assumes that the dependent variable *u* in a partial differential equation can be written as a linear combination of function basis ψ and know position *r* in a domain Ω [94]:

$$u_h=\sum_j u_j\psi_j(r) \quad \in \Omega \tag{3.8}$$

As shown in fig. 3-1, the first step consists of discretizing the domain Ω in a set of elements Ω_e. The join points between elements are called nodes and the group of elements and nodes within the domain is named the mesh. The polynomial approximation of the equation within a typical element is assumed to be written in the form:

$$u_h^e=\sum_j u_j^e\psi_j^e(r) \tag{3.9}$$

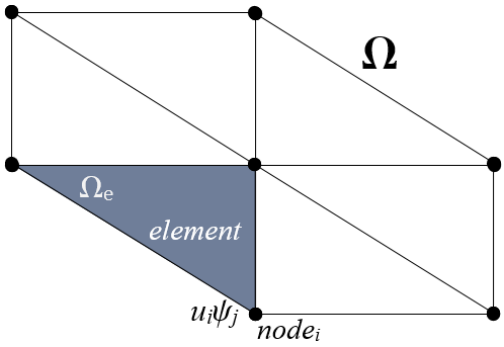

Figure 3-1. Representation of a discretized 2D domain Ω.

Under these considerations the Helmholtz equation can be approximated as [24]:

$$-\nabla^2 u + cu = 0 \tag{3.10}$$

The finite element method solution of this equation, for each element, is found by the minimization of a function in the integral form given by:

$$\frac{1}{2}\iint_{\Omega^e}\left\{-\nabla^2\sum_j u_j^e\psi_j^e + c\sum_j u_j^e\psi_j^e\right\}d\Omega^e = 0 \tag{3.11}$$

For the whole domain, the integral form is expressed as:

$$\sum_l^{N-1}\frac{1}{2}\iint_{\Omega^e}\left\{-\sum_j \nabla^2 u_j^e\psi_l^e + c\sum_j u_j^e\psi_l^e\right\}d\Omega^e = 0 \tag{3.12}$$

The function u on nodes of the elements of the domain is expressed in linear terms as $u_j^e = a + bx_j^e + cy_j^e$. The order of this polynomial approximation can be increased to improve the accuracy.

In the weak formulation, the above equation is converted to a weighted integral in the form:

$$\sum_l^{N-1}\frac{1}{2}\iint_{\Omega^e} w\left\{-\sum_j \nabla^2 u_j^e\psi_l^e + c\sum_j u_j^e\psi_l^e\right\}d\Omega^e = 0 \tag{3.13}$$

where *w(r)* denotes the weight of the function. By using this formulation the above equation can be recast and written as:

$$\sum_l^N K_{l,j}^e u_j^e - f_l^e = 0 \tag{3.14}$$

Or in matrix notation:

$$\left[K^e\right]\left[u^e\right] = \left[f^e\right] \tag{3.15}$$

K^e is a square matrix of order $2N$ and u^e is a $2N$x1 vector. It is worth noting that the eqn. 3.15 is an eigenvalue and several linear algebra solvers could be used to obtain the numerical solutions.

3.3 Surface Plasmon Polaritons

Surface Plasmons Polaritons are oscillations of charge confined at the interface formed by a metal and a dielectric medium. As only TM-polarized waves can excite the SPPs, only this polarization will be taken into account. Considering a waveguide with thickness *d* and infinite

width *w*, then the propagation constant and, consequently, the spatial components of the **E** and **H** fields are determined by solving the dispersion equation [95]:

$$\tan(\kappa_2\, d) = \frac{\kappa_1\, \varepsilon_2/\kappa_2\, \varepsilon_1 + \kappa_3\, \varepsilon_2/\kappa_2\, \varepsilon_3}{1+(\kappa_1\, \varepsilon_2/\kappa_2\, \varepsilon_1)(\kappa_3\, \varepsilon_2/\kappa_2\, \varepsilon_3)}, \tag{3.16}$$

where, $\kappa_{1,3} = \sqrt{\beta^2 - k^2\varepsilon_{1,3}}$, $\kappa_2 = \sqrt{k^2\varepsilon_2 - \beta^2}$. The effective refractive index n_{eff} and the attenuation parameter α are related with propagation constant β through the following expressions [95]:

$$n_{eff} = \frac{\mathrm{Re}\{\beta\}}{k} \tag{3.17a}$$

$$\alpha[\mathrm{dB/cm}] = \mathrm{Im}\{\beta\}\frac{0.2}{\ln 10}, \tag{3.17b}$$

where Re{} and Im{} are the real and imaginary parts, respectively

3.4 Surface Plasmons in a metal/dielectric interface

Now it is considered an interface between a semi-infinite metallic medium and a semi-infinite dielectric medium. The thickness is equal to zero and, therefore, the equation of TM-mode dispersion may be rewritten as follows :

$$\frac{\kappa_1}{\varepsilon_1} = -\frac{\kappa_3}{\varepsilon_3}, \tag{3.18}$$

Solving for β [95]:

$$\beta = k\sqrt{\frac{\varepsilon_m\, \varepsilon_d}{\varepsilon_m + \varepsilon_d}}, \tag{3.19}$$

The expression in (3.19) is known as the dispersión relation of the surface plasmon. This expression represents a guided mode if the real part of the dielectric constant of the metal is negative and its absolute value is greater than the real part of the permittivity of the dielectric, i.e., if $-\mathrm{Re}\{\varepsilon_m\} > \mathrm{Re}\{\varepsilon_d\}$.

The amplitude of the electromagnetic field surface plasmon has a maximum at the interface and decays on both media. Defining the length of penetration L_p as the distance from the interface to which the amplitude of the field has decreased by a factor of $1/e$ [96]–[98]:

$$L_{pm} = \frac{1}{\mathrm{Re}\{\kappa_m\}}, \tag{3.20a}$$

$$L_{pd} = \frac{1}{\mathrm{Re}\{\kappa_d\}}, \tag{3.20b}$$

L_{pm} and L_{pd} are the penetration lengths in metal and dielectric, respectively.

3.5 Kretschmann Configuration

The first experimental configurations for the excitation of surface plasmons were proposed in the 70s by Otto [6] and Kretschmann [7]. Both systems are based on the principle of total internal reflection (TIR) and are modeled mathematically using the expressions of Fresnel reflection coefficients for TM polarization.

As we can see in Figure 3-2, the Otto and Kretschmann configurations use a prism so that the wave vector *k* reaching the prism/dielectric interface in the Otto configuration, or the prism/metal interface in the Kretschmann configuration, comes into resonance with the real part of the constant propagation β of the surface plasmon that is traveling confined at the dielectric/metal interface.

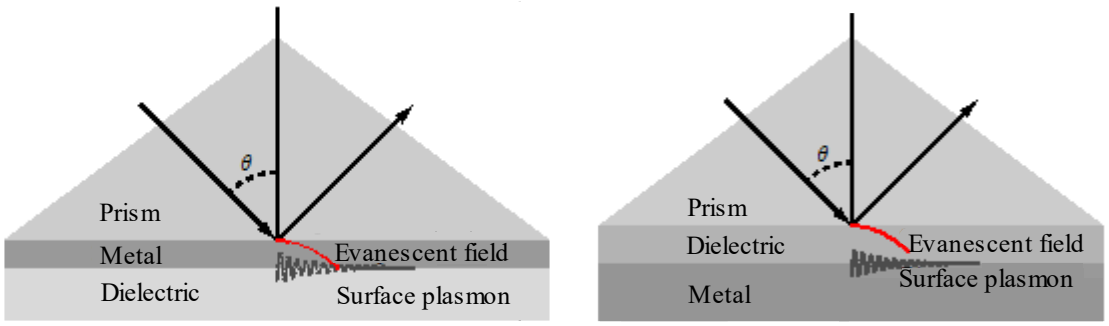

Figure 3-2. a) Kretschmann-Raether y b) Otto configuration to excite surface plasmons [99].

The tangential component of the wave vector of a photon at an interface between two media is:

$$k = \frac{\omega}{c}\sqrt{\varepsilon_d}\ , \tag{3.21}$$

it is always less than the wave vector wave plasmon traveling between the same medium and the metal, see Figure 3-3.

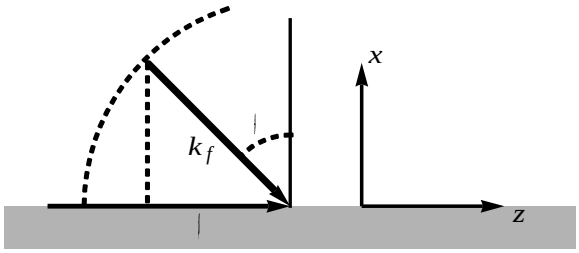

Figure 3-3. Wave vector $\vec{k}_f$ and incidence angle θ of a photon and a surface plasmon traveling in the x-direction in the dielectric-metal interface.

As shown in Figure 3-4, the surface plasmon excitation occurs when the tangential component of the wave vector of the incident photon matches the wave vector of the surface plasmon. In a case of simple reflection, i.e., when the dielectric/metal interface is illuminated with a laser, this condition occurs if the angle of incidence θ measured from the normal is tuned, i.e.:

$$\beta = k \operatorname{sen}\theta \tag{3.22}$$

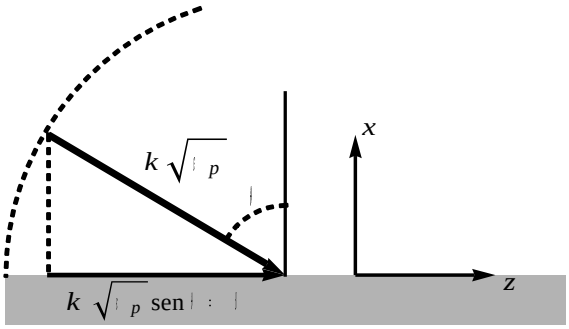

Figure 3-4. Resonance condition of Surface plasmon. The tangential component of the wave vector of the incident photon $\vec{k}_f^{\,z}$ matches the wave vector of Surface plasmon $\vec{k}_{sp}$.

The reflectance for a TM electromagnetic wave in a three-layer system, as used in Kretschmann and Otto configurations and shown in Figure 3-4, is given by [100]

$$R = |r_{123}|^2 = \left| \frac{r_{12} + r_{23} \exp(2jk_2 d_2)}{1 + r_{12} r_{23} \exp(2jk_2 d_2)} \right|^2, \tag{3.23}$$

where,

$$r_{lj} = \left(\frac{\varepsilon_j k_l - \varepsilon_l k_j}{\varepsilon_j k_l + \varepsilon_l k_j} \right), \tag{3.24a}$$

$$k_{l,j} = \frac{\omega}{c} \left[\varepsilon_{l,j} - n^2 sen^2 \theta \right]^{1/2}, \quad l\, j = 1,2,3, \tag{3.24b}$$

In Kretschmann configuration, subscripts 1, 2, 3, refer to the prism, the metal, and the dielectric, respectively. The parameter d_2 in equation (3.23) is the thickness of the metal film between medium 1 and medium 3. According to Figure 3-5, where the reflectance R is plotted against the angle of incidence θ, it is observed that for a given value of θ, R is almost zero. This angle satisfies the aforementioned coupling conditions necessary for the SPR excitation.

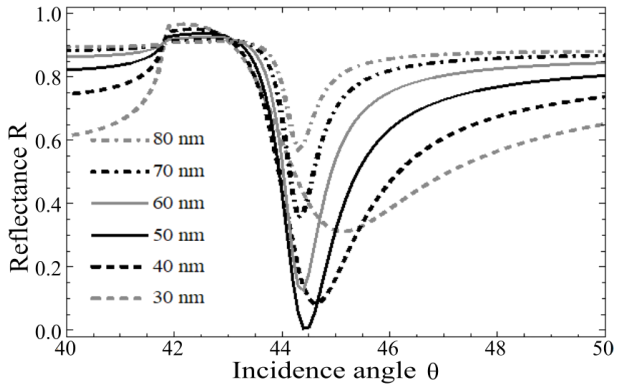

Figure 3-5. Reflectivity, R, vs. Incidence angle, θ, Ag; ε_2 =-18.3+0.45*i*, n_p = 1.515, λ = 632.8 nm and five values of d = 30nm, 40nm, 50nm, 60nm, 70nm.

3.6 Surface Plasmons Polaritons in dielectric/metal/dielectric waveguides

In this case, the waveguide is formed by a metallic medium with dielectric constant ε_m and thickness *2d*, which have a few dozens of nanometers of thickness, inserted between two semi-infinite dielectrics with dielectric constants $\varepsilon_1 = n_1^2$ and $\varepsilon_2 = n_2^2$.

The solution of the dispersion relation for the TM modes shows that this structure supports two different modes of propagation. Depending on the spatial distribution of the *y*-component of the magnetic field, these solutions are known as the symmetric and antisymmetric surface plasmons. Figure 3-6 and 7 show simulations where one can see that the effective refractive index and the attenuation of the symmetrical surface plasmon increase with the thickness of the waveguide. Otherwise, it happens with the effective refractive index and the attenuation of the antisymmetric plasmon, which decreases.

The antisymmetric plasmon is known as Long Range Surface Plasmon Polariton (LR-SPP) due to its low attenuation. This property is exploited in devices for communications [4] and sensors [5]. The propagation length L_{SP} is the distance that the surface plasmon travels until its amplitude decays by a factor *1/e* and is defined as [66], [101]:

$$L_{SP} = \frac{1}{\mathrm{Im}\{\beta\}}, \tag{3.25}$$

Figure 3-6 shows a comparison between the propagation lengths of the symmetric and antisymmetric SPP for a gold film inserted between two layers of silica glass. It can be observed that for a certain range of the metal film thickness, the antisymmetric SPP has a length of up to 50 times the propagation length of the symmetrical SPP.

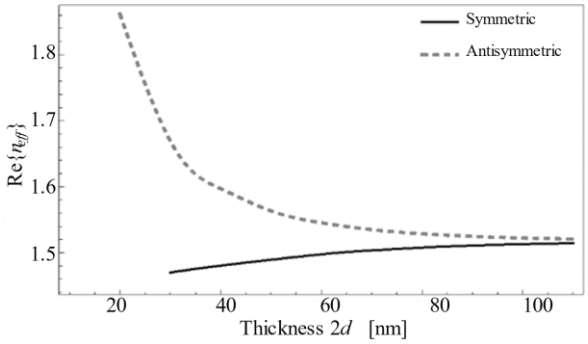

Figure 3-6. Effective refractive index of symmetric and antisymmetric surface plasmon polaritons.

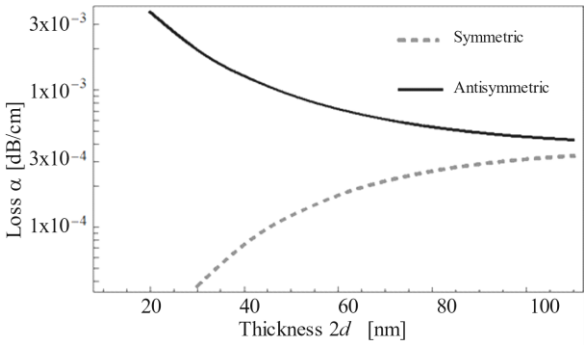

Figure 3-7. Attenuation of symmetric and antisymmetric surface plasmon polaritons.

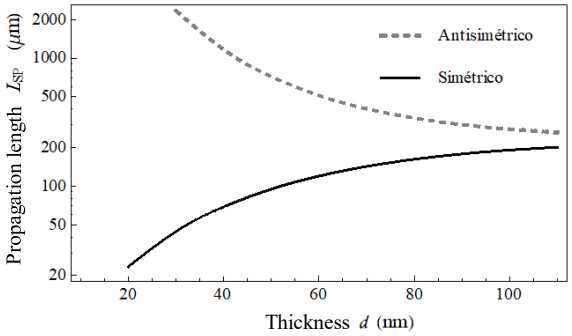

Figure 3-8. Propagation length of symmetric and antisymmetric surface plasmon polaritons.

3.7 Surface Plasmon Polaritons in metal nano-strips

Unlike infinite metal slab, which is considered to have a finite thickness and infinite width, a metal strip waveguide is a structure bounded in both directions, i.e. with finite width *w* and thickness *d*. There is no exact expression for the dispersion equation for this kind of structure because the width is inhomogeneous in one direction. Because of this inhomogeneity, the modes supported by the structure are hybrid and formed by the superposition of TE and TM fields. Furthermore, the strip corners facilitate the excitation of localized modes that could be coupled to surface modes. As a first approximation, the field components for the TE and TM are [102]–[105]:

$$\frac{d^2E_y}{dx^2}+\frac{d^2E_y}{dy^2}+\left(n_1^2k_0^2+\beta^2\right)E_y=0 \tag{3.26a}$$

$$\varepsilon(x)\frac{\partial}{\partial x}\left(\frac{1}{\varepsilon(x)}\frac{dH_y}{dx}\right)+\frac{d^2H_y}{dy^2}+\left(n_1^2k_0^2+\beta^2\right)H_y=0 \tag{3.26b}$$

Remaining components of electric (E_x, E_z) and magnetic (H_x, H_z) fields are derived in terms of E_y and H_y:

$$E_x = \frac{i}{\omega\beta}\left(\frac{1}{\varepsilon_r}\frac{\partial^2 H_y}{\partial x^2} + \omega^2\varepsilon_0\mu H_y\right) \tag{3.27a}$$

$$E_z = \frac{1}{\beta}\frac{\partial E_y}{\partial y} - \frac{i}{\omega^2\varepsilon_0\varepsilon_r}\frac{\partial H_y}{\partial x} \tag{3.27b}$$

$$H_x = \frac{i}{\omega\beta}\left(\frac{1}{\mu}\frac{\partial^2 E_y}{\partial x^2} + \omega^2\varepsilon_0\varepsilon_r E_y\right) \tag{3.27c}$$

$$H_z = \frac{1}{\beta}\frac{\partial H_y}{\partial y^2} + \frac{i}{\omega\mu}\frac{\partial E_y}{\partial x} \tag{3.27d}$$

The solution of equations 3.27 leads to four bound modes named according to their spatial distribution. Two letters, *a* and *s*, are used for denoting the symmetry or asymmetry of the spatial distribution of the electric field of the mode with respect to *y* and *x*-axes, respectively. A superscript *m* is used to help identify the *m-th* order of each mode, while a subscript *b* or *l* is used to identify if the *mth* mode is bound or leaky. For example, ss_0^b denotes the fundamental bound mode ($m = 0$) having symmetry with both axes.

The aspect ratio between width *w* and thickness *t* spatial determine which component of electric fields is predominant in the mode. If *w/t <1, E_x* is the dominant component. On the other hand, *w/t >1, E_y* dominates.

Cut off wavelength for the existence of *m* mode is given as:

$$\lambda_m = \mathrm{Re}\left\{\frac{2\pi w\sqrt{n_1^2 - n_2^2}}{(m/2)}\right\} \tag{3.28}$$

Nevertheless, it is often helpful to estimate the number of surface modes supported by the strip. In these cases, the cut-off width w_m could be expressed as:

$$w_m = \lambda_0\,\mathrm{Re}\left\{\sqrt{\frac{\varepsilon_m + \varepsilon_d}{\varepsilon_m \times \varepsilon_d}}\right\} m \tag{3.29}$$

Equation 3.29 shows that in a finite strip the width *w* also acts as a waveguide (in which the thickness $t \to 0$), thus, only the modes that met the condition, imposed by the equation (3.29) are supported by the strip. As can be seen in Figure 3-9, when the materials that surround the metal strip have different optical properties, $as_{b,i}$ modes are excited.

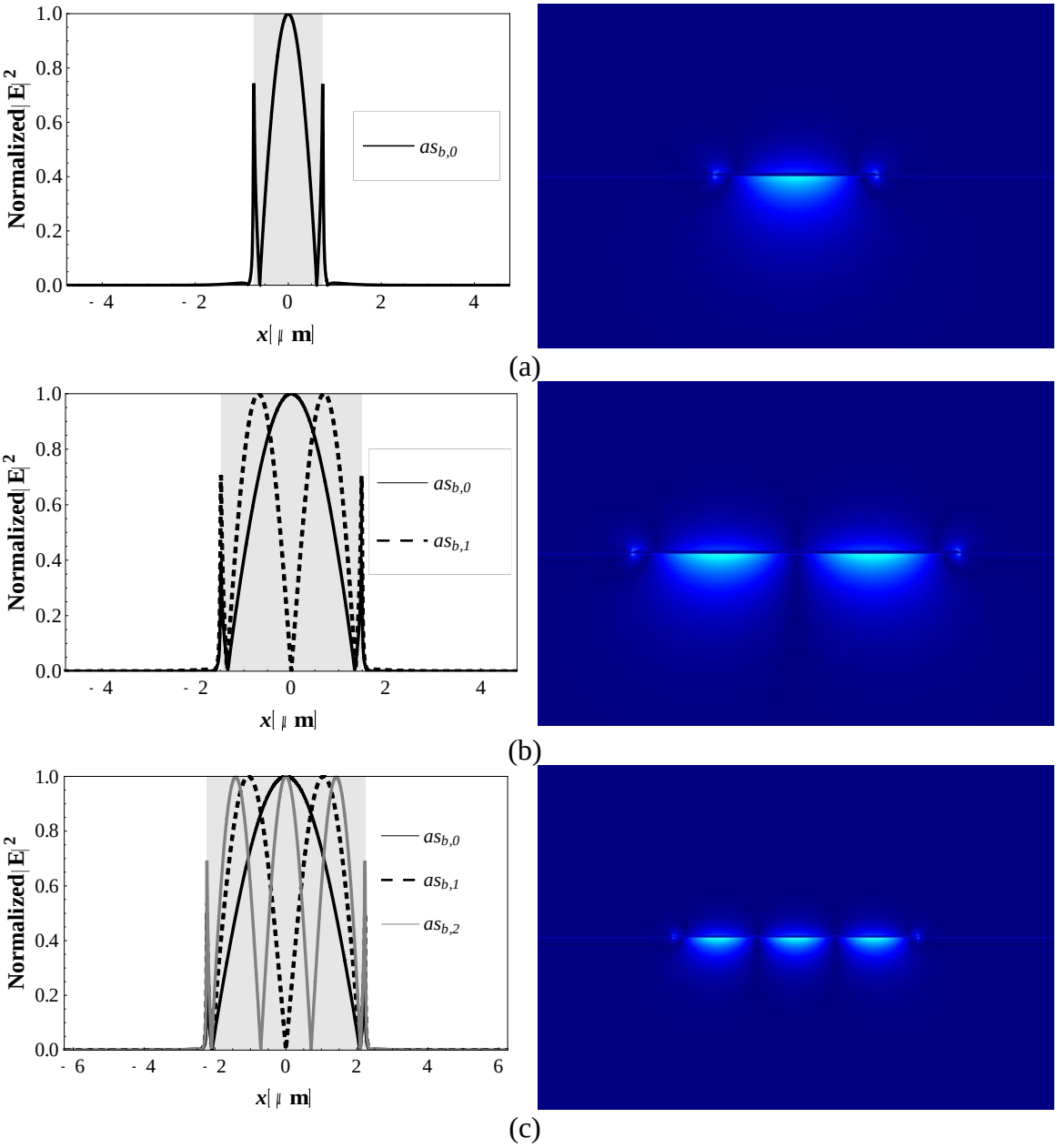

Figure 3-9. (left) Normalized magnitude of the **E** and **(right)** Transverse field distribution for assymetric bound modes a) $as_{b,0}$, b) $as_{b,1}$, and c) $as_{b,2}$ λ=1.0μm, ε_m=-41.2838+2.4611*i*, n_1=1.3249, n_2=1.4504.

The dependences of the real and imaginary part of the effective refractive index on the width w, for the first three modes, are shown in Figure 3-10.

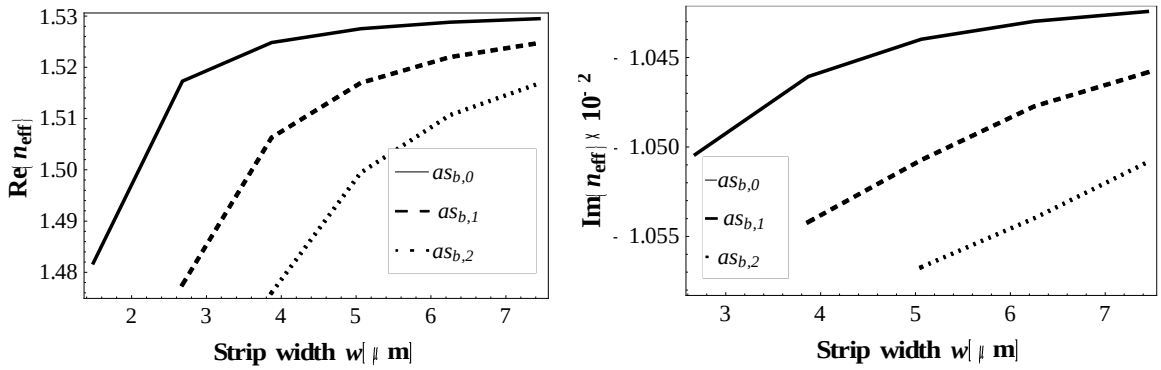

Figure 3-10. Re{n_{eff} }and Im{n_{eff}}as a function of w. λ=1.0μm, ε_m=-41.2838+2.4611i, n_1=1.3249, n_2=1.4504.

3.8 Surface Plasmon Resonance in multilayer stacks

Most mathematical models used for calculating the complex propagation constants are based on the transfer matrix method (TMM) combined with contour integrals in the complex plane for finding the zeros of the resultant dispersion equation [106]. In a multilayer structure, as is shown in Figure 3-11, electric and magnetic fields could be expressed as [107]:

$$\vec{\Phi}(y,z) = \hat{x}\,\mathrm{Re}\left\{\Phi(y)\exp\left[i(\beta z - \omega t)\right]\right\} \tag{3.30}$$

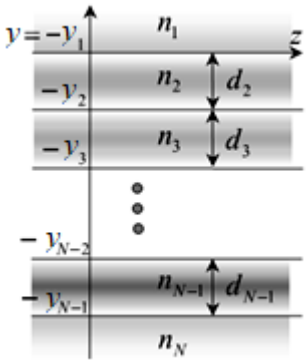

Figure 3-11. Multilayer structure

$$\begin{aligned}
&\varphi_x(y) = \exp\{-\gamma_1(y-d)\}; && y \le 0 \\
&\varphi_x(y) = \varphi_{i,1}\cos\{\kappa_i(y+y_{i-1})\} + \varphi_{i,2}\frac{m_i}{\kappa_i}\operatorname{sen}\{\kappa_i(y+y_{i-1})\}; && -y_{i-1} > y > y_i \\
&\varphi_x(y) = B\exp\{\gamma_N(y+y_{N-1})\}; && y < -y_{N-1} \\
&i = 2,...,N-1
\end{aligned} \tag{3.31}$$

where, $\gamma_{1,N} = \sqrt{\beta^2 - k^2\varepsilon_{1,N}}$, $\kappa_i = \sqrt{k^2\varepsilon_j - \beta^2}$, $\Phi_x(x)$ expresses indistinctly to $E_x(y)$ or $H_x(y)$; $m_i = 1$ for TE modes and $m_i = \varepsilon_i$ for TM modes. Moreover, the time dependence $\exp\{i\omega t\}$, and the propagation term $\exp\{-i\beta z\}$, were omitted. The exponential decay on the outer layers implies that the solution corresponds to bounded *b* or leaky modes *l*. In the above equation $(\varphi_{j,1}, \varphi_{j,2})$ are founded using the following relation,

$$\begin{bmatrix} \varphi_{j+1,1} \\ \varphi_{j+1,2} \end{bmatrix} = M_i \begin{bmatrix} \varphi_{j,1} \\ \varphi_{j,2} \end{bmatrix} \qquad j = 2,....., N-1 \tag{3.32}$$

M_i is the well-known transfer matrix,

$$\begin{bmatrix} \cos(\kappa_j d_j) & \dfrac{m_j}{\kappa_j}\operatorname{sen}(\kappa_j d_j) \\ \dfrac{\kappa_j}{m_j}\operatorname{sen}(\kappa_j d_j) & \cos(\kappa_j d_j) \end{bmatrix} \tag{3.33}$$

From the boundary conditions in y=0 $(\varphi_{j,1}, \varphi_{j,2})$ are calculated as,

$$\begin{bmatrix} \varphi_{2,1} \\ \varphi_{2,2} \end{bmatrix} = \begin{bmatrix} 1 \\ -\dfrac{\gamma_1}{m_1} \end{bmatrix} \tag{3.34}$$

The dispersion equation is obtained applying the boundary conditions for non-magnetical materials in the interfaces $y = -y_j \quad j = 1,...., N-1$, which require the continuity of the tangential components for $\varphi_y(y)$ and $\frac{1}{m_j}\frac{d}{dy}\{\varphi_x(y)\}$, and using recursively the equation 3.29 [29],

$$F\left(\beta^2\right)=\phi_{N,2}-\frac{\gamma_N}{m_N}\phi_{N,1} \tag{3.35}$$

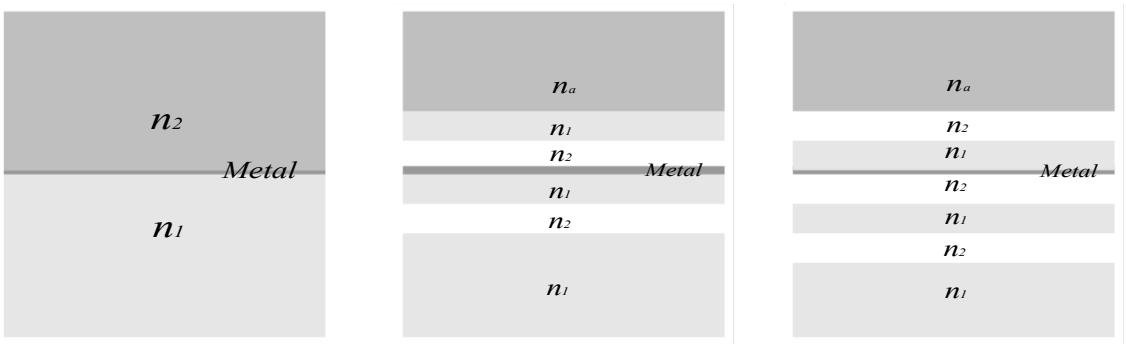

Figure 3-12. Analyzed structures. (a) basic structure. Asymmetric dielectric-metal-dielectric (DMD) waveguide (b) n_1 on top of the metal layer (c) n_1 underneath of the metal layer. n_a=1.3249, n_1=1.4504, n_2=1.4004. ε_m=-41.2838+2.4611i.

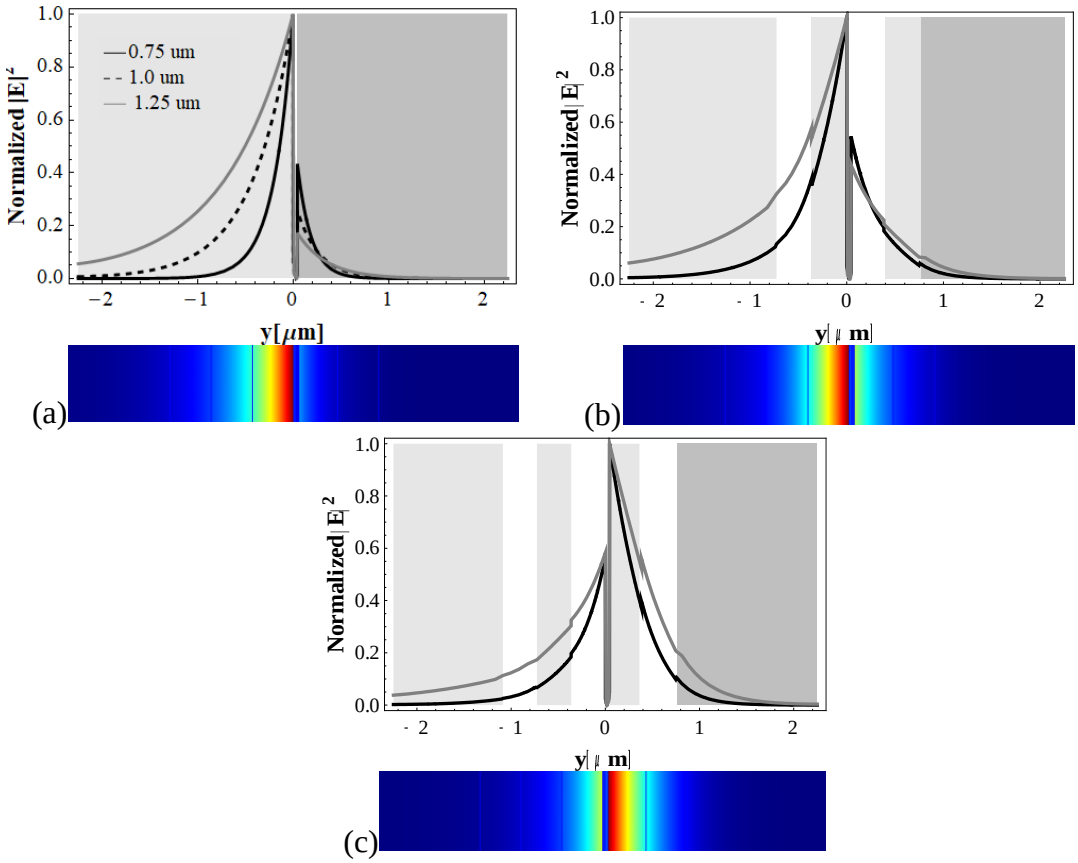

Figure 3-13. The normalized magnitude of the **E**. (a) no multilayer structure. (b) n_1 on top of the metal layer. (c) n_1 underneath of the metal layer. n_a=1.3249, n_1=1.4504, n_2=1.4004. ε_m=-41.2838+2.4611i.

The structures depicted in Figures 3-12(a) and 3-12(b) can be used for modifying the optical properties of the excited SPP mode, and how it interacts with the outer mediums. For instance, as can be shown in Figure 3-13, the position of the dielectric n_1 with respect to the metal layer determines the side in which the SPP mode should have a longer penetration length.

3.9 SPP in Metal Nano-wires

Metal nanowire could be modeled as a straight and long cylinder of radius a with relative permittivity ε_m surrounded by an infinite dielectric medium with relative permittivity ε_d. Under these assumptions, the longitudinal components of the magnetic field can be written as [107]:

$$H_z = H_z(x,y)e^{-i\beta z} \tag{3.36b}$$

Within the metal, $r<a$, and dielectric, $r>a$ the longitudinal components of the magnetic field fulfills the following equations nanowires [93]:

$0 < r < a$,

$$\frac{d^2H_{zm}}{dr^2}+\frac{1}{r}\frac{dH_{zm}}{dr}+\left(n_1^2k_0^2-\beta^2-\frac{m^2}{r^2}\right)H_{zm}=0 \tag{3.37a}$$

$r > a$,

$$\frac{d^2H_{zd}}{dr^2}+\frac{1}{r}\frac{dH_{zd}}{dr}+\left(n_2^2k_0^2-\beta^2-\frac{m^2}{r^2}\right)H_{zd}=0 \tag{3.37b}$$

Taking into consideration the boundary conditions in $r=a$ ($H_{zm}=H_{zd}|_{r=a}$) and that $H \to 0$ when $r \to \infty$, the solutions of the above equations are:

$$H_{zm} = B\frac{I_m\left(\frac{U_1}{a}r\right)}{I_m(U_1)}e^{im\varphi}e^{-i\beta z} \tag{3.38a}$$

$$H_{zd} = B\frac{K_m\left(\frac{U_1}{a}r\right)}{K_m(U_1)}e^{im\varphi}e^{-i\beta z} \tag{3.38b}$$

$$H_{\varphi m}=\left[-\frac{\beta Bma^2}{U_1^2 r}\frac{I_m\left(\frac{U_1}{a}r\right)}{I_m\left(U_1\right)}+\frac{i\omega\varepsilon_0 n_1^2 Aa}{U_1^2}\frac{I'_m\left(\frac{U_1}{a}r\right)}{I_m\left(U_1\right)}\right]e^{im\varphi}e^{-i\beta z} \tag{3.38c}$$

$$H_{\varphi d}=\left[-\frac{\beta Bma^2}{U_2^2 r}\frac{K_m\left(\frac{U_2}{a}r\right)}{K_m\left(U_2\right)}+\frac{i\omega\varepsilon_0 n_2^2 Aa}{U_2^2}\frac{K'_m\left(\frac{U_2}{a}r\right)}{K_m\left(U_2\right)}\right]e^{im\varphi}e^{-i\beta z} \tag{3.38d}$$

where A and B are constants, $U_1=a\sqrt{\beta^2-k_0^2n_1^2}$ and $U_2=a\sqrt{\beta^2-k_0^2n_2^2}$, furthermore, $U_1^2>0$, $U_2^2>0$. From the continuity of the azimuthal components $H_{\varphi m}=H_{\varphi d}$ in $r=a$, the following dispersion equations for TM modes could be obtained,

- TM Modes

$$\frac{\beta Bma^2}{U_1^2 r}\frac{I_m\left(\frac{U_1}{a}r\right)}{I_m\left(U_1\right)}+\frac{i\omega\varepsilon_0 n_1^2 Aa}{U_1^2}\frac{I'_m\left(\frac{U_1}{a}r\right)}{I_m\left(U_1\right)}=\frac{\beta Bma^2}{U_2^2 r}\frac{K_m\left(\frac{U_2}{a}r\right)}{K_m\left(U_2\right)}+\frac{i\omega\varepsilon_0 n_2^2 Aa}{U_2^2}\frac{K'_m\left(\frac{U_2}{a}r\right)}{K_m\left(U_2\right)} \tag{3.39}$$

- SPP Modes

If $m = 0$, and since $I'_0\left(x\right)=I_1\left(x\right)$ and $K'_0\left(x\right)=-K_1\left(x\right)$ then, the dispersion equations for TM modes can be written as (TE modes do not exist):

$$\frac{n_1^2}{U_2}\frac{I_1\left(U_1\right)}{I_0\left(U_1\right)}+\frac{n_2^2}{U_2}\frac{K_1\left(U_2\right)}{K_0\left(U_2\right)}=0 \quad \text{TM} \tag{3.40}$$

When $m\neq 0$ the following expressions are obtained for TM Modes,

$$\frac{\beta Bm}{U_1^2}-\frac{i\omega\varepsilon_0 n_1^2 A}{U_1}\frac{I_m\left(U_1\right)}{I_m\left(U_1\right)}=\frac{\beta Bm}{U_2^2}-\frac{i\omega\varepsilon_0 n_2^2 A}{U_2}\frac{K'_m\left(U_2\right)}{K_m\left(U_2\right)} \tag{3.41}$$

Solving for A/B and then simplifying, it is possible to obtain the following dispersion relation:

$$(\beta m)^2\left(\frac{1}{U_1^2}-\frac{1}{U_2^2}\right)^2=-k_0^2\left(n_1^2\xi_m-n_2^2\eta_m\right)\left(\xi_m-\eta_m\right) \tag{3.42}$$

where, $\xi_m=\frac{1}{U_1}\frac{I_m(U_1)}{I_m(U_1)}>0$ and $\eta_m=\frac{1}{U_2}\frac{K'_m(U_2)}{K_m(U_2)}<0$. Finally, as $\beta=n_{eff}k_0$ and solving for ξ_m the relation of dispersion could be set as follows:

$$\xi_m=\frac{n_1^2+n_2^2}{2n_1^2}\eta_m\pm\left[\left(\frac{n_1^2-n_1^2}{2n_1^2}\right)^2\eta_m^2+m^2\frac{n_{eff}^2}{n_1^2}\left(\frac{1}{U_1^2}-\frac{1}{U_2^2}\right)^2\right] \tag{3.43}$$

The negative sign corresponds to EH_m modes while the positive corresponds to HE_m modes, because the conditions set for ξ_m and η_m only HE_m modes are guided by the structure.

- Cutoff Radius

As the permittivity of the metal varies with the operating wavelength is not easy to obtain a wavelength λ_c cutoff (as usually is done for standard optical fibers) instead, it is better to define the cutoff radius a_c. For TM mode, the cut-off condition requires that $U_2\to 0$ and $V_c=V\to U_1$, consequently, the equation (3.44) has not an exact solution and the fundamental mode exists for any value of *a*.

The dispersion equation for HE_m modes at the cutoff condition is:

$$\left(\frac{n_1^2+n_2^2}{2n_2^2}\frac{1}{V_c}\frac{I'_m(V_c)U_2^2}{I_m(V_c)}+m\right)^2=U_2^4\left(\frac{n_1^2-n_1^2}{2n_2^2}\right)^2\left(\frac{1}{V_c}\frac{I'_m(V_c)}{I_m(V_c)}\right)+m\left(\frac{U_2^2}{U_1^2}-1\right)^2 \tag{3.44}$$

For each value of *m*, this expression can be resolved for $V_{c,m}$. Values of $a_{c,m}$ (cut of radius for each HE_m mode) are calculated using the following relation:

$$a_m=\frac{\lambda}{\sqrt{\pi}}\mathrm{Re}\left\{\sqrt{\frac{\varepsilon_m+\varepsilon_d}{\varepsilon_m\times\varepsilon_d}}\right\}J_{0,m} \tag{3.45}$$

where $J_{0,m}$ is the first zero of the Bessel function of first kind and order *m*.

From the above expressions, it is clear that the excited SPP modes are localized on the outer edge of the nanowire, and it acts as a kind waveguide only allowing the excitation of modes with a certain distribution of the electric field. The spatial distribution of the transverse

electric field for the first three modes is depicted in Figure 3-14 (a)-(c). Figure 3-15 shows the dependence of the Re{n_{eff}} and Im{ n_{eff} }on the radius of nanowire for the modes TM_{01} and TM_{11}. It is important to emphasize that the superior order modes are degenerate.

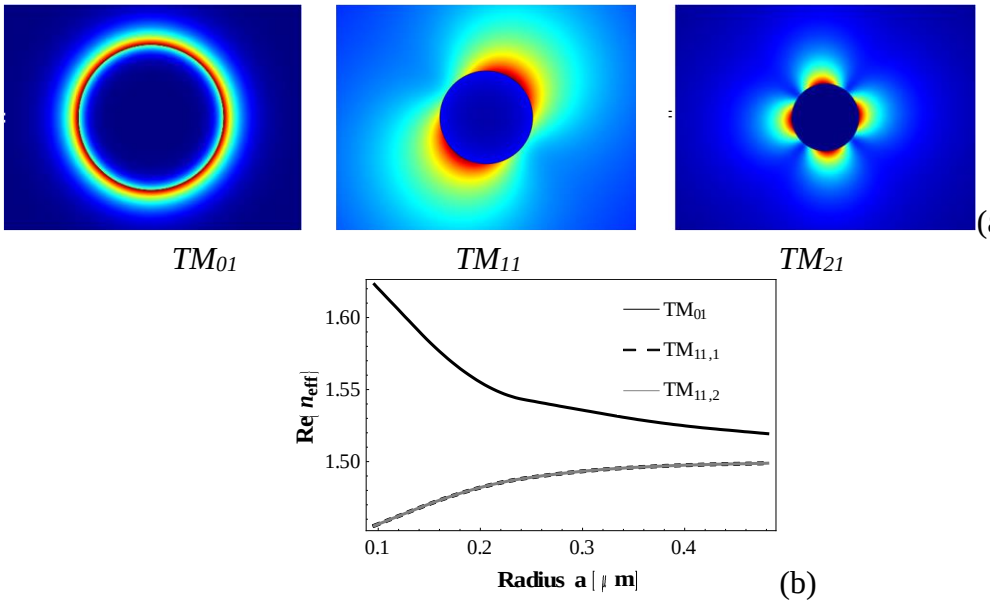

Figure 3-14. (a) Tarnsverse feld distribution of TM modes. (b) Dependence of Re{n_{eff}} on nanowire radius a. λ=1.0μm, n_a=1.3249, n_1=1.4504, n_2=1.4004, ε_m=-41.2838+2.4611i.

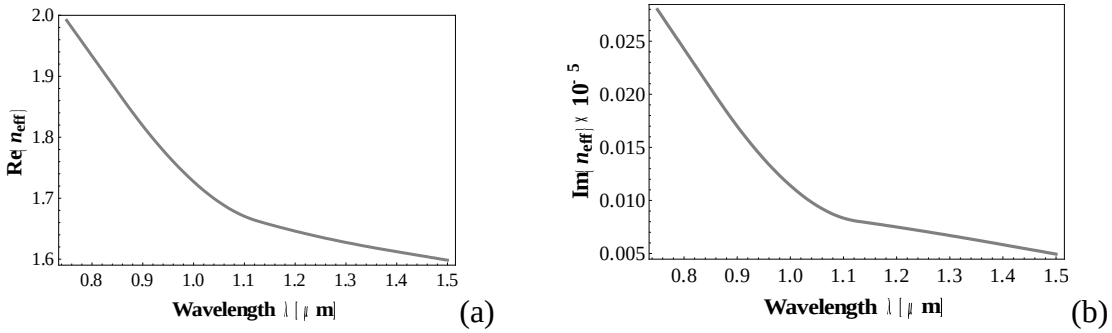

Figure 3-15. Dependence of (a) Re{n_{eff}} and (b) Im{n_{eff}} on wavelength λ. Values of n_1 and ε_m were calculated using the Sellmeier equation and Drude-Lorentz model [53] respectively.

3.10 SPR in D-shaped Optical Fibers

Optical fibers are generally circular dielectric waveguides composed of two concentric solid cylinders. The inner cylinder with radius a and refractive index n_{co} is the core, and the exterior cylinder with refractive index n_{cl} is denoted as cladding. In a single-mode optical fiber, the electric field has a single spacial shape, known as the fundamental mode. This feature

depends on the core radius, the refractive indices n_c and n_{cl}, and the light wavelength λ. In step-index guides, the single-mode operation occurs when the normalized frequency V, as defined in equation (3.46), is less to 2.405 [5]:

$$V = \frac{2\pi a}{\lambda}\sqrt{n_c^2 - n_{cl}^2}\,, \tag{3.46}$$

To find the spatial distribution of modes that can be propagated in the fiber, it is necessary to rewrite the wave equation in cylindrical coordinates. Making use of the cylindrical symmetry and considering implicit frequency dependence, the following expression is derived in terms of the longitudinal component E_z [5]:

$$\frac{\partial^2 E_z}{\partial \rho^2} + \frac{1}{\rho}\frac{\partial E_z}{\partial \rho} + \frac{1}{\rho^2}\frac{\partial^2 E_z}{\partial \phi^2} + \frac{\partial^2 E_z}{\partial z^2} + n^2 k_0^2 E_z = 0\,, \tag{3.47}$$

From equation (3.47) and after some mathematical considerations, the following eigenvalue equation is obtained [108]:

$$\left[\frac{J'_m(Ua)}{UJ_m(Ua)} + \frac{K'_m(Wa)}{WK_m(Wa)}\right]\left[\frac{J'_m(Ua)}{UJ_m(Ua)} + \frac{n_{cl}^2}{n_c^2}\frac{K'_m(Wa)}{WK_m(Wa)}\right] = \frac{m^2}{a^2}\left(\frac{1}{U^2} + \frac{1}{W^2}\right)\left(\frac{1}{U^2} + \frac{n_{cl}^2}{n_c^2}\frac{1}{W^2}\right), \tag{3.48}$$

Equation (3.48) can be solved to determine the propagation constant β_m for each propagation mode. To excite SPR in a single-mode (or a few-mode) optical fiber, a metallic film of nanometer thickness is deposited close to the core region. Some chemical techniques and physical methods are used to remove part of the fiber cladding, obtaining a flat surface close to the fiber core, thus the metal film is deposited. This new structure, shown in Figure 3-16, is known as D-shaped fiber.

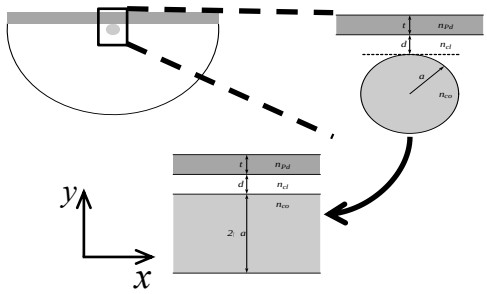

Figure 3-16. D-shaped fiber and its equivalent slab structure.

A simple method to find the response of the excitation of the SPR is to transform the cross-section of the D-shaped fiber into an equivalent slab waveguide structure, as shown in the same figure. The refractive indexes of the D-shaped fiber are [109], [110]:

$$n(y)=\begin{cases} n_{y1}=\left(n_{co}^2-\left(U^2-p^2\right)\right)^{1/2}\left(k_0a\right)^1, & |y|<\sigma a \\ n_{y1}=\left(n_{cl}^2-p^2\sec^2(p\sigma)\right)^{1/2}\left(k_0a\right)^1, & |y|>\sigma a \end{cases} \tag{3.49}$$

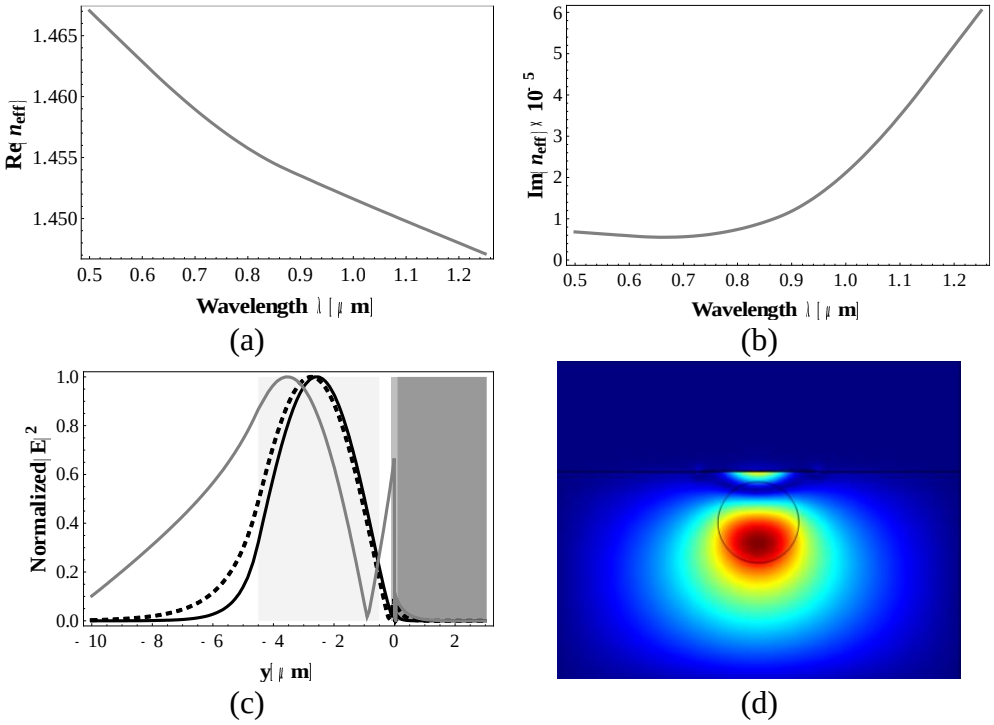

Figure 3-17. Optical properties of hybrid modes excited in a D-shaped optical fiber. (a) Re{n_{eff}}.(b) Im{n_{eff}}. (c) The normalized magnitude of the **E**. (c) Transverse field distribution.

Parameters p and σ are chosen in such a way that the spatial distributions along the y-direction of the D-shaped fiber and the slab waveguide are similar [55]. Using this methodology, it is possible to establish a transcendental equation for the electric field by the transfer matrix method [111]–[113]. Furthermore, the multiple solutions of this transcendental equation are achieved by methods of complex analysis (Cauchy integral based on the argument principle and the residue theorem).

4. MULTI-PLASMON RESONANCES IN MICROSTRUCTURED OPTICAL FIBERS

Content of this chapter is part of the peer-reviewed contribution:

N. D. Gomez-Cardona, E. Reyes-Vera, and P. I. Torres, *"Multi-Plasmon Resonances in Microstructured Optical Fibers: Extending the Detection Range of SPR Sensors and a Multi-Analyte Sensing Technique,"* IEEE Sens. J., vol. 18, pp. 7492–7498, 2018.

Related contributions presented at conferences with proceedings published:

N. Gomez-Cardona, E. Reyes-Vera, C. Jimenez-Durango, J. Usuga-Restrepo, and P. Torres, "Novel Wide-Bandwidth Polarization Filter Based on H-Shaped Micro-Structured Optical Fiber with Gold Nano-strip," in 2018 International Conference on Electromagnetics in Advanced Applications (ICEAA), Sep. 2018, pp. 538–541.

N. Gómez-Cardona and P. Torres, "Sensitivity Analysis of SPR Sensors Based on Suspended- core Microstructured Optical Fibers," in Latin America Optics and Photonics Conference, 2012, no. 1, pp. 12–14, doi: 10.1364/LAOP.2012.LS4C.2.

4.1 Motivation

The majority of studies on MOF-based SPR sensors have been framed to the case of a single resonance. However, the possibility of having several plasmonic excitations in the transmittance spectrum of the same MOF-based device has been demonstrated theoretically by Hassani and Skorobogatiy [114]. For example, multi-plasmon resonances in MOFs are used to achieve SPR sensors with a large refractive index (RI) detection range and as a multi-analyte sensing technique.

In this chapter, a theoretical study on multi-plasmon excitations in suspended core fibers SCFs with three and four holes, for sensing applications is presented. Numerical simulations are performed using the finite element method (FEM) by taking into account variations in the thickness of the metal film and analyte RI changes. This study addresses the influence of the fiber cross-sectional structure and multiple plasmon excitations on the performance of MOF-based SPR sensors. The results indicate that the excitation of higher-order SPP modes could be an alternative to achieve SPR sensors with a large dynamic RI range and competitive resolution. In addition, we show that multi-plasmon excitations have the potential for multi-analyte sensing applications or to be operated in self-reference mode.

4.2 Structure and Numerical Modeling

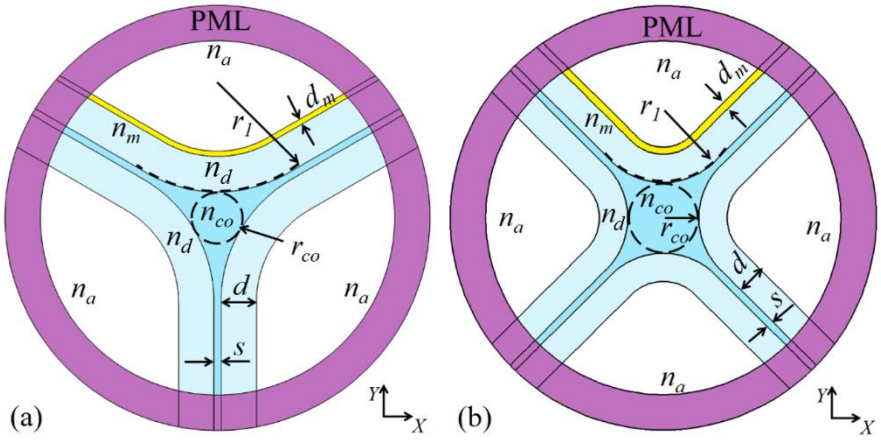

Figure 4-1. Structural parameters of the a) three-hole SCF and b) four-hole SCF.

Figure 4-1(a) and 1(b) show the two cross-sections of the SCFs under study. For sensor operation, we considered post-processed SCF with an exposed region of the core. Some chemical (wet etching) and physical (micro-machining) techniques have been widely used for side opening the SCF [115], or by creating an opening region in the preform stage during the manufacture of the fiber. This structure has been previously demonstrated in polymers [116], soft glass, and silica fibers [48], and it results in exposed regions of the fiber core. Then, a sequential deposition on the exposed region of SCF of a dielectric layer of thickness d via polymers or down-doped silica, and a gold layer of thickness d_m deposited by high-pressure chemical vapor deposition or physical vapor deposition [117]. The RI of the dielectric layer must be slightly smaller than the fiber to control the coupling strength between the core mode and the plasmon wave, thus regulating the propagation loss of the sensor.

In this new structure, the plasmonic waves are excited in the metalized hole as shown in Figure 4-1. Our study assumes that all the fiber holes are filled with the analyte. Sellmeier's equation was used to model the refractive index of silica n_s, while the Lorentz-Drude model reported in [118] was used for the gold dielectric constants. Such material is widely preferred for biological applications due to its relatively easier surface chemistry and chemical stability. The refractive index of the dielectric layer was taken as n_d=n_s-0.01. We used the commercially available software package COMSOL Multiphysics to calculate the complex propagation constants of the core-guided and plasmonic modes. To study the effect of the

cross-sectional structure of the fibers, we fixed the thickness of the core struts s= 0.2 μm and the fiber core radius r_{co} = 1 μm. For these, the core curvature radii are r_1 = 4 μm and r_1 = 2.0 μm for the three-hole and four-hole structures, respectively. In both cases, the thickness of the dielectric layer was fixed at d = 1 μm. A perfectly matched layer (PML) was used to match the outmost layer. Due to the symmetry of both structures (y-axis), only the y-polarized fundamental core mode is analyzed in this work.

As a first step for understanding the coupling properties of SCFs, Figure 4-2 shows the dispersion relations around the corresponding resonant wavelengths with d_m= 40 nm and n_a = 1.39. The real part of the effective RI, Re{n_{eff}}, is important because it determines the phase-matching conditions for the excitation of SPP modes by the fundamental core-guided mode. The fundamental SPP mode, excited on the opposite surface to the metal-analyte surface of the analyte channel does not interact with the analyte, has a much higher effective RI than the core-guided mode, and can never couple to it [27]. By contrast, the higher-order SPP modes -referred to as SPP1, SPP2, and SPP3- have much smaller effective refractive indices. The imaginary part of the effective RI, Im{n_{eff}}, to which the core mode loss is proportional [119], is also included in Figure 4-2.

Resonance is characterized by an obvious peak of the core-guided mode loss spectrum, as shown in Figure 4-2, which indicates the largest energy transfer from the core-guided mode to the plasmonic mode at a particular wavelength, where the Re{n_{eff}} of the core-guided mode and the plasmon mode coincide. For instance, in this case, three SPP modes supported by the cylindrical analyte channels are involved in the coupling properties of the SCFs in Figure 4-1. The insets in Figure 4-2 show the electric field distributions of the core-guided mode and SPP modes that indicate the nature of the coupling and the transfer of energy from the fundamental core mode to the plasmon modes.

It is important to note that the shape of the fiber core and metalized surface have a significant effect on the plasmonic excitation spectrum. In Figure 4-2, the Im{n_{eff}} of the core-guided mode in the wavelength range of 0.5–0.9 μm features three plasmonic excitation peaks at 714, 758, and 794 nm for the three-hole SCF and at 620, 662 and 716 nm for the four-hole SCF. One can observe that, with the double symmetry of the four-hole SCF (x and y-axes), the plasmonic excitation peaks are better defined and have a smaller spectral width. Conversely, with one symmetry axis in the three-hole SCF (y-axis), plasmonic excitation peaks are closer and present a higher spectral width. These characteristics strongly influence the performance of the sensor.

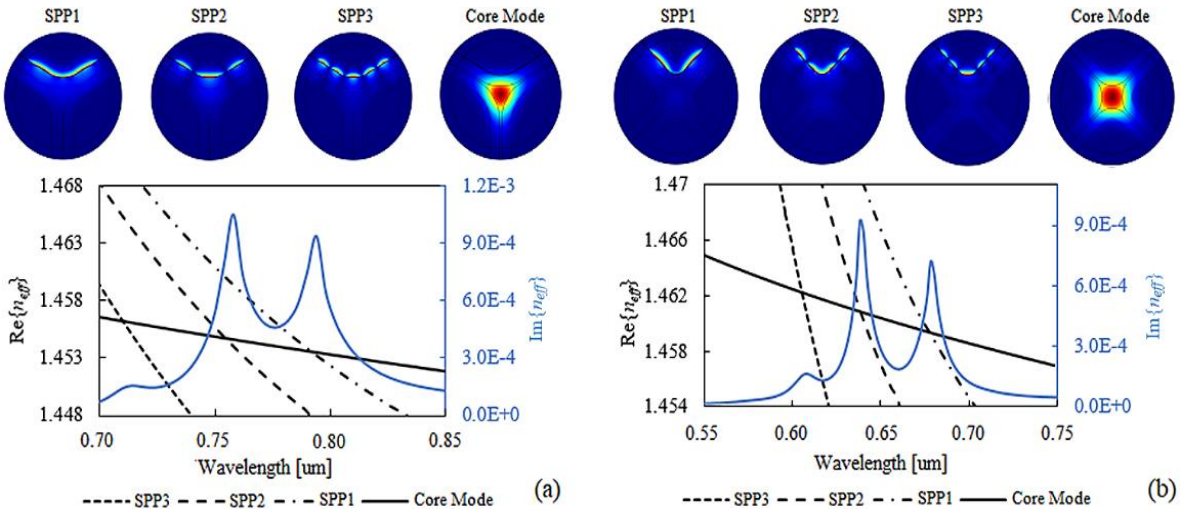

Figure 4-2. Dispersion relations of the core-guided mode (black solid line) and SPP modes (black dashed curves), and imaginary part of the effective refractive index Im{n_{eff}} (blue solid curve) of a) a three-hole SCF and b) a four-hole SCF, where d_m = 40 nm and n_a = 1.39.

4.3 Sensor Performance and Discussion

To study the performance of SCF-based SPR sensors, gold layers in a specific range of thicknesses and analytes with certain RI values were considered. The thickness of the gold layer varied from 50 nm to 70 nm while the refractive index of the analyte, from 1.33 to 1.39, as shown in Figure 4-3. In general, it can be seen in both structures that the peaks caused by resonances move towards a longer wavelength, and the loss of the core-guided mode gradually increases as the analyte RI rises. The growing analyte RI leads to a small difference between the fiber core and the surrounding medium, which results in a decreasing effective RI of the core-guided mode. Therefore, the resonant peaks shift to longer wavelengths and more core energy is transferred to the SPP mode, which leads to greater coupling efficiency. In addition, because the plasmonic wave is very sensitive to the thickness of the metal layer, it has been observed that the loss of the core-guided mode decreases and the resonance wavelengths shift towards longer wavelengths with the increase of the gold layer thickness.

Fiber-based SPR sensors are naturally suitable for a wavelength interrogation scheme [120]. Changes in the analyte RI are detected by measuring the displacement of a plasmonic peak λ_{RES}. As can be seen in Figure 4-3, a dominant loss peak is observed in both structures when the analyte RI is below 1.36. Besides, the coupling between the SPP1 mode and the core-guided mode is much stronger than between higher-order SPP modes and the core-guide mode (gray regions). However, when the analyte RI value increases, the coupling between higher-order (SPP2 and SPP3) modes and the core-guided mode is much stronger than between the SPP1 mode and the core-guide mode (clear regions). As shown in these figures,

the modified SCF-based SPR sensors have the potential for an even greater range of analyte refractive indices than the ones reported in the literature (see red dots, n_a > 1.36). In the case of the three-hole SCF, the SPP2 mode loss peak can be monitored when the gold layer is 50 and 70 nm thick, while the SPP3 mode loss peak can be monitored when such layer is 60 nm thick. On the other hand, in the case of the four-hole SCF, the results show that the SPP3 mode loss peak can be monitored over the entire range of gold thicknesses under study. This process enables the operation in an extended analyte RI range of the SPR sensors based on three- and four-hole SCFs, as shown in Figure 4-4.

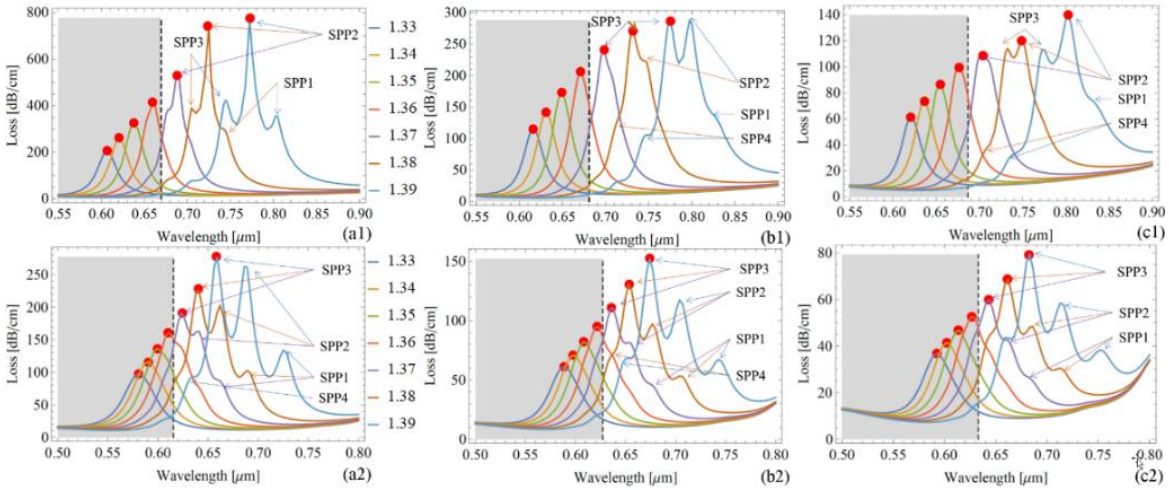

Figure 4-3. Calculated loss spectra of the core-guided mode of the three- and four-hole SCFs with analyte RI changes from 1.33 to 1.39. a) d_m = 50 nm, b) d_m = 60 nm, and c) d_m = 70 nm. The red dots indicate the resonant wavelengths. Top figures (a1, b1 and c1): three-hole SCF. Bottom figures (a2, b2 and c2): four-hole SCF.

Figure 4-4(a) shows that the resonant wavelength shift, with respect to the analyte variation, exhibits a nonlinear feature due to the strong mode coupling between the high order plasmon modes and the core-guided mode. Figure 4-4(b) illustrates the sensor sensitivity $S_n = d\lambda_{RES}/dn_a$ as a function of the analyte RI. The sensitivity ranges are 1500-6100 nm/RIU and 800-2300 nm/RIU for the SPR sensors based on three- and four-hole SCFs, respectively. On the assumption that a 0.1 nm resonance wavelength peak can be detected, the sensor resolution is $RES = 0.1/S_n$. Therefore, the minimum resolutions that can be achieved with the modified three- and four-hole PCFs in Figure 4-1 are 1.6×10-5 RIU and 4.3×10-5 RIU, respectively, as shown in Figure 4-4(c).

Table 4-1. Performance characteristics of MOF-based SPR sensors for analyte RI detection by wavelength interrogation.

Characteristics	Multi-analyte	*RI* Range	S_n (nm/RIU)	*RES Min.* (RIU^{-1})	Ref.

Exposed core three holes Ag coated	No	1.33-1.34	3000 @ n_a=1.34	3.3 x10^{-5}	[121]
D-shaped Au coated	No	1.33-1.34	2900 @ n_a=1.34	3.4 x10^{-5}	[122]
PCF Au coated	Yes	1.33-1.35	4600 @ n_a=1.35	2.0 x10^{-5}	[123]
PCF Au coated	No	1.33-1.38	3000 @ n_a=1.38	3.3 x10^{-5}	[124]
Exposed core grapefruit Ag coated	No	1.33-1.42	6200 @ n_a=1.39	4.9 x10^{-5}	[125]
U-shaped PCF Au	No	1.36-1.40	6000 @ n_a=1.39	1.3 x10^{-5}	[126]
Three hole PCF Au	No	1.33-1.42	4500 @ n_a=1.39	2.2 x10^{-5}	[48]
Three hole PCF Au	Yes	1.36-1.46	2000 @ n_a=1.39	6.5 x10^{-6}	[119]
Exposed core three holes Au coated	Yes	1.33-1.39	6100 @ n_a=1.39	4.0 x10^{-5}	This work
Exposed core four holes Au coated			2300 @ n_a=1.39	1.0 x10^{-5}	

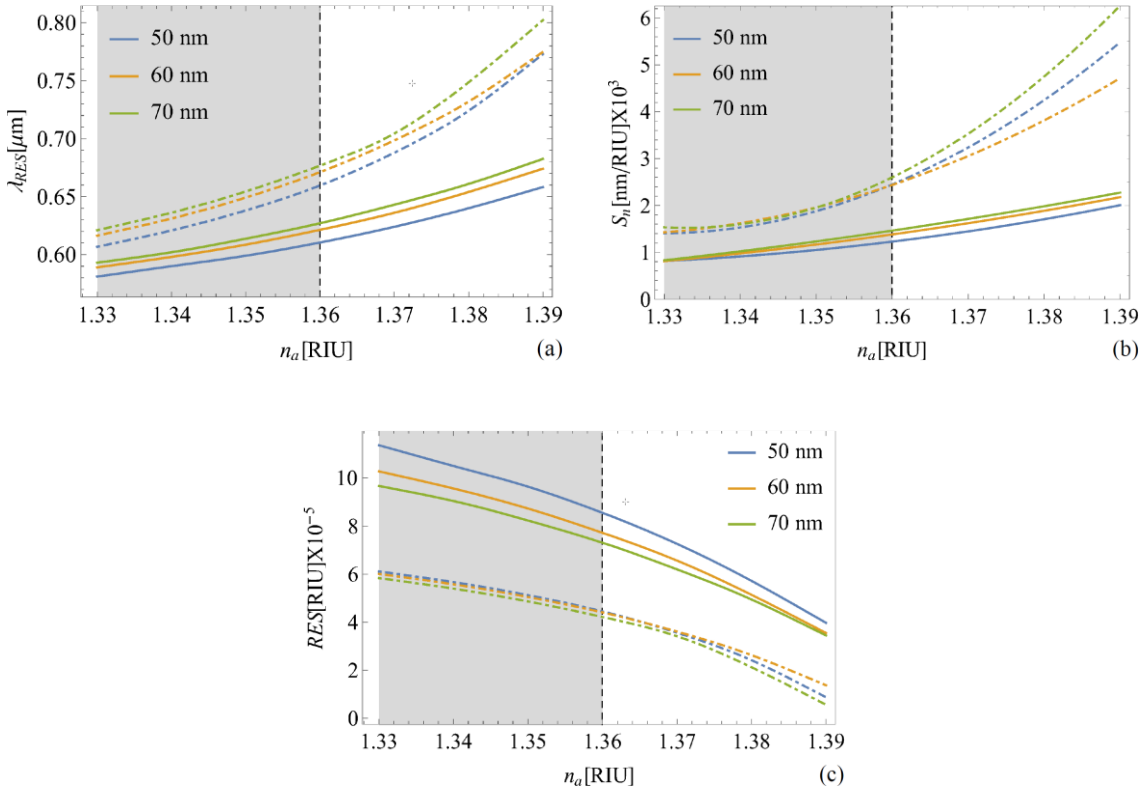

Figure 4-4. Operation of the SPR sensors based on three- and four-hole SCFs in an extended analyte RI range. a) Resonance wavelength, b) sensitivity, and c) resolution with dm = 50, 60 and 70 nm. Solid lines: Four-hole SCF. Dashed lines: Three-hole SCF.

Table 4-1 summarizes the performance characteristics of different MOF-based SPR sensors for analyte RI detection by wavelength interrogation. We believe that the excitation of higher-order SPP modes in modified SCF-SPR sensors proposed in this work is competitive and outstanding among numerous MOF-based SPR sensor alternatives because it offers a

large dynamic detection range and competitive resolution without intricate designs whose manufacture is limited to achievable metal structures.

In addition to the study of the detection range, we also investigated the potential of multi-plasmon excitations for multi-analyte sensing applications. For example, in this work, we considered the case of a four-hole SCF in which the channels in the vertical axis were coated with a 50-nm gold layer, as shown in Figure 4-5(a). In the first condition, Channel 1 and Channel 2 were filled with analytes n_{a1} = 1.33 and n_{a2} = 1.38, respectively, while maintaining the same structural parameters as those previously used. In the second condition, a different set of refractive indices was considered: n_{a1} = 1.34 and n_{a2} = 1.39. Figure 4-5(b) illustrates the simulation results from the two conditions of the *y*-polarized field and for n_{a1} = 1.33+0.001 and n_{a2} = 1.38+0.001.

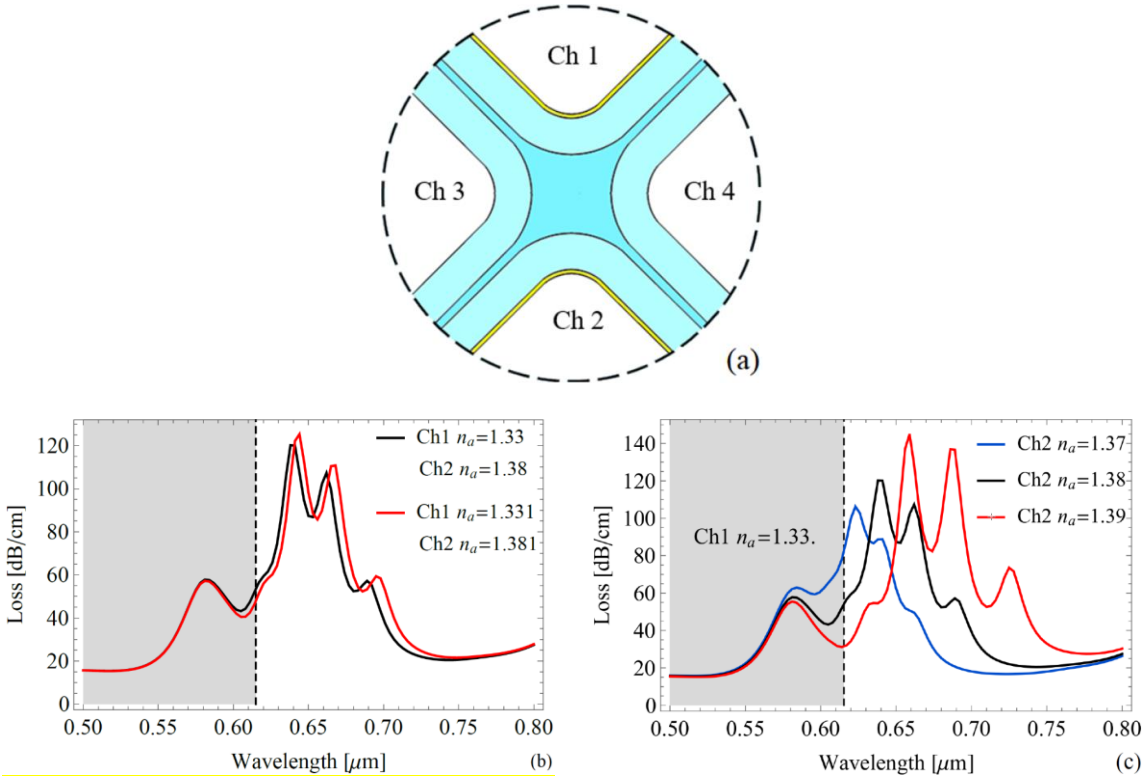

Figure 4-5. Multi-analyte sensing and self-referencing in the four-hole SCF. a) Four-hole SCF with two uniformly coated air holes; b) multi-analyte operation in which the attenuation peaks are caused by the presence of two different analytes; c) self-referencing operation.

It should be noted that the resonance features are dissimilar in different channels. In agreement with Figure 4-4(b), the shifts of the peaks are larger when n_a > 1.36. In Channel 1, the strongest coupling occurs with the SPP1 mode while on Channel 2, it occurs with the SPP3 mode. Hence, each channel exhibits a spectrally differentiable plasmonic loss peak.

Eventually, the multi-plasmon resonance method proposed in this work can be improved by adding a thin high-refractive-index dielectric layer on top of the gold surface [127], [128]. The fiber may be configured, for example, with four holes optimized for multi-analyte detection by combining the two techniques. This analysis is subject to future work. On the other hand, the four-hole SCF in Figure 4-5(a) can be operated in a self-referencing mode, where Channel 1 is chosen as the reference channel, and Channel 2 works as the sensing channel. The operation of the device is shown in Figure 4-5(c); n_{a1} is set at 1.33 on Channel 1 while n_{a2} ranges from 1.37 to 1.39 in Channel 2. As it can be seen in this figure, the variation of the analyte refractive index in Channel 2 causes a red shift in the sensing signal while no shifts are detected in the reference channel containing the fixed analyte. Hence, instead of a single resonance peak, the spectral separation between two resonance peaks can be used to correct the effect of temperature variations [29].

Finally, although this work is numerical, the generalized sensing setup using the proposed sensor is shown in Figure 4-6. As it is evident from the figure, we propose the use of a broadband light source to launch the optical power into a conventional single-mode fiber (SMF). A splicing technique can be used to connect the SMF with the proposed SC-MOF sensor. The output spectra can be recorded over a large range of wavelengths using an optical spectrum analyzer. The inset shows the design of a simple double v-groove holder with a small chamber reservoir in the center, which could be fabricated in glass, Teflon or other inert material to avoid chemical reactivity. The use of ceramic ferrules on the output ends of SC-MOF facilitates the manipulation and interrogation of the device.

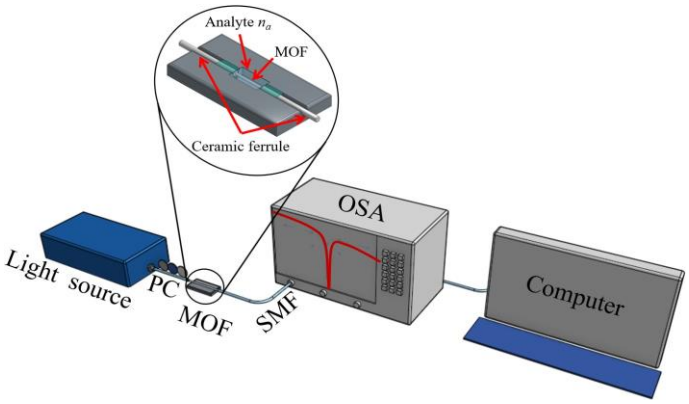

Figure 4-6. Schematic diagram of the proposed sensor setup for practical sensing PC: Polarization controller; SMF: Single mode fiber; OSA: Optical spectrum analyzer.

4.4 Summary

In summary, we presented a theoretical investigation on multi-plasmon excitations in the spectrum of SPR sensors based on modified SCFs with three and four holes. A dominant

plasmonic loss peak in both structures was found when the analyte RI was less than 1.36, a condition that occurs when the coupling between the SPP1 mode and the core-guided mode is stronger than with higher-order SPP modes. In contrast, when the analyte RI was greater than 1.36, the coupling between the SPP2 and SPP3 modes and the core-guided mode was detected to be stronger than with the SPP1 mode. It has been shown that with multi-plasmon excitations in the three- and four-hole PCFs, an analyte RI range from 1.33 to 1.39 can be achieved as well as sensitivities of up to 6 100 and 2 300 nm/RIU, respectively. Furthermore, the proposed multi-plasmon excitations could be configured to implement two functionalities: multi-analyte sensing and self-referencing. The results of this work can have a significant impact on the design of MOF-based SPR sensors aimed at striking a good balance between sensor sensitivity and ease of manufacture.

5. EXCITATION OF LONG-RANGE SURFACE PLASMON POLARITONS IN H-SHAPED OPTICAL FIBER

Content of this chapter is part of the peer-reviewed contribution:

N. Gomez-Cardona, E. Reyes-Vera, and P. Torres, "High Sensitivity Refractive Index Sensor Based on the Excitation of Long-Range Surface Plasmon Polaritons in H-Shaped Optical Fiber," Sensors, vol. 20, no. 7, p. 2111, Apr. 2020, doi: 10.3390/s20072111.

Related contributions presented at conferences with published proceedings.

N. D. Gómez-Cardona, E. Reyes-Vera, P. Torres, E. Reyes-Vera, and P. Torres, "Multi-analyte refractive index sensor based on hybrid long range plasmon modes in H-shaped optical fiber," in Latin America Optics and Photonics Conference, Nov. 2018, p. Tu5B.4

N. D. Gómez-Cardona, E. Reyes-Vera, R. A. Herrera, P. Torres, and P. Torres, "Novel refractive index sensor based on hybrid long range plasmon in H-shaped optical fiber," in Frontiers in Optics / Laser Science, Sep. 2018, p. JTu2A.97, doi: 10.1364/FIO.2018.JTu2A.97.

5.1 Motivation

The long-range surface plasmon polariton (LRSPP) modes have been observed experimentally [28], [129]–[133], and due to their low loss properties, they have a high potential for the development of applications based on planar waveguides, such as couplers, polarizers, perfect absorbers, sensors, nonlinear optics and solar energy [118], or LRSPP refractive index (RI) sensors based on prism-coupling, which use angular interrogation schemes [134] that use bulky optical components and require fine-tuning, which makes remote sensing and miniaturization difficult. Optical fibers with appropriate metal coating have also been demonstrated to be an SPP-sensing device. In most of the above cases, theoretical analysis is performed using analytical or semi-analytical mathematical models that exploit the characteristics of the simplified model of the planar waveguide, for instance, transfer matrix [135] or perturbation theory [136]. On the other hand, the emergence of microstructured optical fibers (MOFs) was one of the most important breakthroughs in the optical fiber sensor technology, since the optical characteristics of the propagating light into this kind of optical fibers and the evanescent field depend on the fiber microstructure and its geometrical parameters. Thus, the response of the devices based on MOFs can be controlled and improved through the variation of the geometrical structure, which allows more flexibility in the designs [137], [138]. In recent years, many MOF-SPP sensors with different

structures have been proposed to increase the sensitivity of these type of sensors, some of the alternatives are based on the selective filling of the fiber microstructure with an analyte or with a metal nanowire [139]–[142]. In other alternatives, metallic layers are deposited on the inner walls of the microstructure holes then filled with analytes [118]. For an updated review of MOF-based SPP sensors see, e.g. [124], [143]. Considering the limitations of the internal sensing mechanism (the metal coating and analyte are placed inside the fiber), SPP sensors based on D-shaped or exposed core structures provide a possible solution to internal sensing as the SPP is in direct contact with the external medium [144].

In this chapter, a simple structure to achieve LRSPP modes using an H-shaped optical fiber, on which it is possible to deposit a dielectric-metal-dielectric waveguide (DMDW) structure using physical or chemical methods [117], is proposed and numerically analyzed. In this new configuration, the LRSPP modes interact directly with the analyte. Besides, the resonance wavelengths of LRSPP modes are shorter than SRSPP modes. Based on this approach, we present and discuss the performance of a novel design of high sensitivity, multi-analyte RI sensor by LRSPP mode excitation in an H-shaped MOF with two symmetrical DMDWs deposited on the inner walls of its two side holes. Numerical simulations were performed using the finite element method (FEM) by taking into account the variations in the refractive index of the dielectric films, the thickness of the thin metal film, and the analyte RI changes. Our results indicate that the excitation of LRSPP modes in both open holes, but with different resonance wavelengths, have the potential to be operated either in self-reference mode or multi-analyte sensing applications. In addition, we found that varying the DMDW parameters is possible to obtain higher, narrower plasmonic peaks with similar intensities. Finally, we demonstrate that the deposition of the DMDW structure leads to operating at longer wavelengths, which is one of the main constraints of conventional plasmonic devices [29]. Thus, the proposed configuration based on DMDW improves significantly the key parameters of the device, such as the resolution (RES), sensitivity (Sn), full width at half maximum (FWHM) and figure of merit (FOM).

5.2 Sensor Structure and Theory

The proposed RI sensing device is based on the structure shown in Figure 5-1a. It consists of an H-shaped silica MOF formed by a solid cladding of silica with refractive index ns, a solid core of refractive index n_{co} and radius r_{co} = 2.5 µm, surrounded by two side holes of radius r_{ho} = 15 µm, each one of them filled with a liquid analyte of refractive index $n_{a,j}$, j = 1, 2. Moreover, a symmetrical DMDW, formed by a thin gold layer of thickness d_m and two dielectric layers of thickness d_{d1} and d_{d2}, is deposited on the inner wall of the two open side holes at a distance d. Figure 5-2 shows a schematic of the sensor fabrication process.

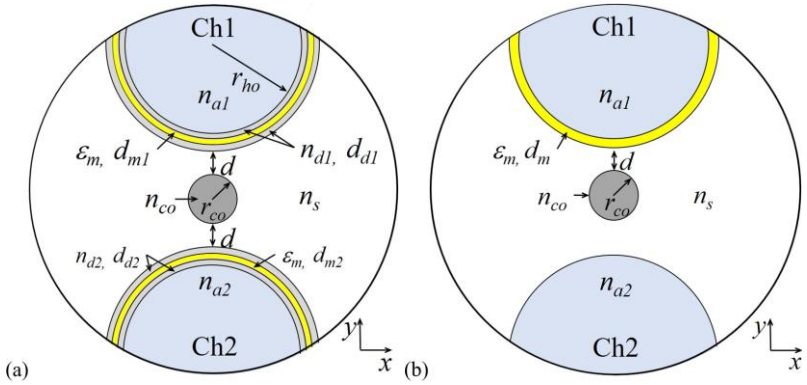

Figure 5-1. Structural parameters of the microstructured optical fiber (MOF): (**a**) with dielectric–metal–dielectric waveguide (DMDW) and (**b**) without DMDW.

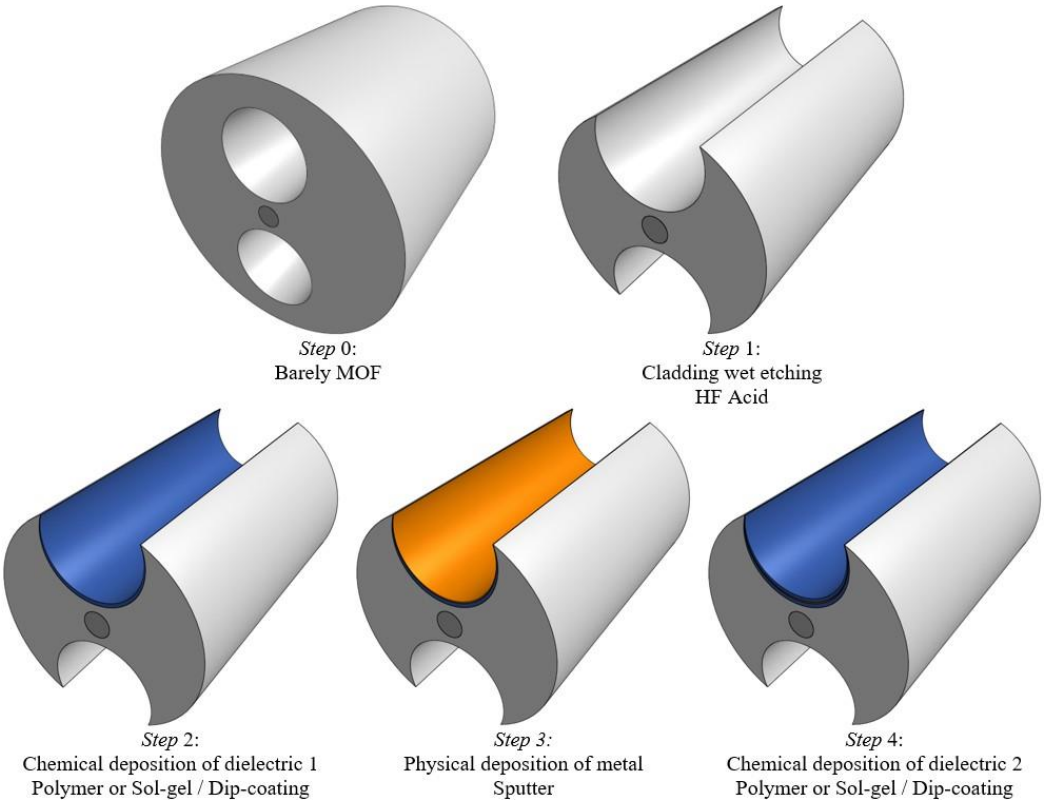

Figure 5-2. Schematic of the sensor fabrication process.

The RI of dielectric layers must be slightly higher than the fiber to control the coupling strength between the core mode and the plasmon wave, thus regulating the propagation loss of the sensor. The structure without DMDW, depicted in Figure 5-1(b), is used as a reference and retains the optical properties of the fiber core, cladding, and thin metal layer.

Since the sensing region is exposed to the external environment in our design, the sensors can achieve rapid response and real-time sensing.

The modeling and numerical analysis were carried out using finite-element-method-based software COMSOL 5.1 The electromagnetic waves, frequency-domain solver, with extremely fine element size, was used to obtain improved element quality. Quadratic triangular elements were chosen for improving the convergence and reducing the error. The maximum size element for the fiber core and dielectric layers was established as $\lambda/5$ (λ is the operating wavelength) and $d_d/5$, respectively, while in the metallic layer this parameter was established as $d_m/7$. A Cartesian perfectly matched layer (PML) with a width of 1.5 µm, a maximum mesh size of $\lambda/5$, and an outer scattering boundary condition were used to avoid unwanted numerical reflections from the outer edge to the region under study. These provide the simulation accuracy of the analysis carried out for the proposed sensor.

The refractive indexes of the silica cladding n_s and the doped silica core n_{co} were modeled using the Sellmeier's equation [30], while the Lorentz-Drude model [50] was used to model the electrical permittivity of metal ε_m. In this work the refractive indexes of dielectrics of DWDM n_{d1} and n_{d2}, and the analyte n_a were considered variables.

In the DMDW structure, the symmetric plasmonic mode is localized near the dielectric with the lowest permittivity while the anti-symmetric mode is near dielectric with the highest permittivity [145]. On the other hand, the H-shaped fiber supports only one linearly polarized mode [95]. The propagation constants of the DMDW modes can be approximated using the following equation [146]:

$$\beta = \frac{2\pi}{\lambda}\sqrt{\frac{\varepsilon_m \varepsilon_d}{\varepsilon_m + \varepsilon_d}} \tag{5.1}$$

where $\varepsilon_d = n_{2d}$ is the relative permittivity of the dielectric films of DWDM. Since these films are very thin and in contact with different media, ε_d values can be considered averaged or weighted values [147], [148], or effective values that are described in the effective-medium theory [48], [118], [136], [141], [149], [150]; furthermore, the analyte RI is always lower than the cladding RI and hence, the symmetric plasmonic mode will be excited at the interface close to the analyte.

In accordance with the previous description, the operation principle of the sensor is based on the resonance of plasmonic modes excited by the fundamental core-guided mode. Clearly, the proposed structure is naturally suitable for a wavelength interrogation scheme [142]. Changes in the analyte RI are detected by measuring the shift of a resonance peak, λ_{RES}, in the loss spectrum of the core-guided mode, which can be obtained from the following equation [151]:

$$Loss = 8.6856 \times \frac{2\pi}{\lambda} \times \mathrm{Im}\left\{ n_{eff} \right\} \tag{5.2}$$

Since the losses of the *x*-polarized mode are relatively low, only the *y*-polarized mode was considered in this study. For example, Figure 5-3(a) shows the resonance peaks under different conditions on the surface of the inner walls of the MOF. From this Figure 5-it is evident that the deposition of the DMDW improves the energy transfer from the core-guided mode to the symmetric plasmonic mode; consequently, higher resonant peaks with smaller spectral width are obtained.

Also, the MOF with DMDW operates at larger wavelengths compared to the MOF without DMDW, which makes this sensor more promising as it will find significant applications in the field of biomedical at near IR region [47]. Figure 5-3(b) illustrates the normalized electric field distribution close to the resonance condition. The insets in this figure confirm the largest energy transfers from the core-guided mode to the plasmonic mode with the DMDWs.

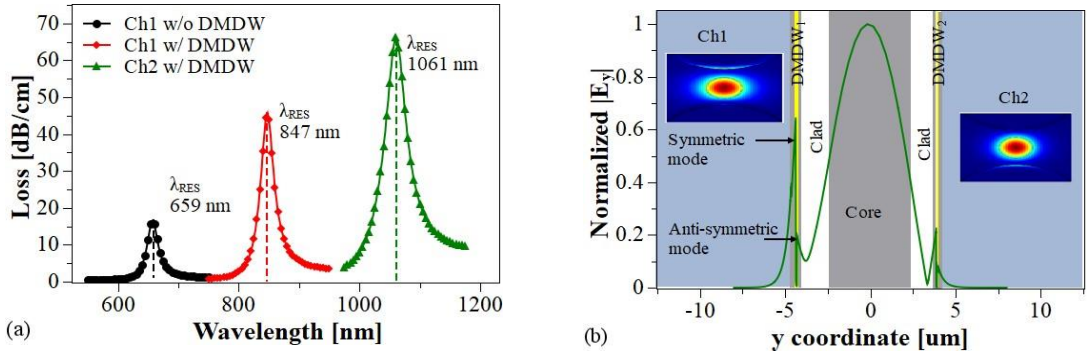

Figure 5-3. (a) Calculatedloss spectra for the fiber core mode with n_a = 1.36, d = 1 µm, d_m= 60 nm, d_{d1} = 0.1 µm (Ch1), d_{d1} = 0.2 µm (Ch2). (b) Normalized electric field.

5.3 Sensor Performance and Discussion

Sensor performance was evaluated in terms of the resolution, $RES = \delta\lambda_{DR}/S_n$, sensitivity, $S_n = \delta\lambda_{RES}/\delta n_a$, full width at half maximum (FWHM) of the resonant peaks, $\Delta\lambda_{\mathrm{FWHM}}$, and figure of merit, $FOM = S_n/\Delta\lambda_{FWHM}$. δn_a describes the changes in the analyte refractive index, $\Delta\lambda_{RES}$ represents the shift in resonance wavelength, and $\Delta\lambda_{DR}$ is the minimal spectral resolution of the spectrometer used to acquire the transmission loss spectrum. Figure 5-4(a) depicts the behavior of the loss spectra for two different configurations of the DMDW having different values of Δn and d_d1, while the thickness of the gold layer dm was varied from 35 nm to 75 nm; n_a = 1.36 was assumed to be constant. As can be seen, in both cases the increase in dm decreases the strength of the resonance peak and shifts the resonance wavelength towards longer wavelengths. On the other hand, Figure 5-4(b) shows the loss spectra for two different

values of d_d. Here, n_d was changed from $n_d = n_{co}$ to $n_d = n_{co} + 0.006$ RIU in steps of 0.002 RIU, while n_a and d_m were kept constant at 1.36 RIU and 45 nm, respectively. In both cases, we observe a redshift in the resonance wavelength with the increase in Δn, however, this shift is greater in the structure with the highest value of d_d. It is important to note that the variations in Δn did not generate changes in the shape of the loss spectrum, unlike what is observed when the thickness of the gold layer was varied.

In addition, the potential of the structure in self-referenced or multi-analyte operation was investigated. Two different cases were considered. In the first one, the DMDWs deposited inside each side hole of the MOF maintain their geometrical and optical parameters. As is shown in Figure 5-5(a), in this case, the shift in the resonant wavelength is only a few dozen nanometers and, therefore, the two loss spectra overlap, making it difficult to resolve the resonance-wavelength shifts. In the other case, the DMDWs deposited have similar geometries, i.e., $d_{d1} = d_{d2}$ and $d_{m1} = d_{m2}$, but the RI of the DMDW dielectric n_{d1} and n_{d2} are different. In this case, depicted in Figure 5-5(b), the peaks of loss spectra appear sufficiently separated, about ten times the shift of the previous condition, and therefore could easily be resolved.

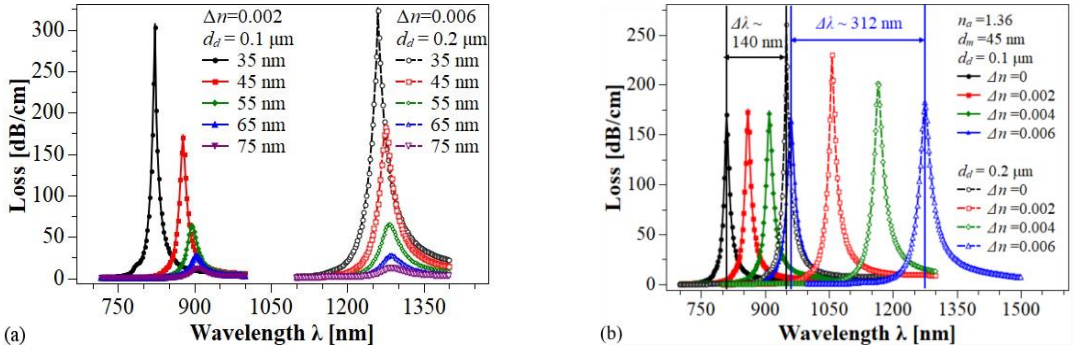

Figure 5-4. Loss spectra of the fiber core mode having a DMDW in each hole. (a) Two different values of n_d and d_d, while varying the thickness dm of the gold layer. (b) Two different values of d_d, with d_m = 45 nm, while increasing the refractive index (RI) of the DMDW dielectrics. d = 1 µm and n_a = 1.36 were constant for all cases. Solid lines: Ch1. Dashed lines: Ch2.

Also, the strength of resonance peaks was similar, which facilitates their detection. This characteristic in the sensor spectral response allows multi-analyte detection since the shifts of the loss peak in Ch1, controlled by variations of n_{a1}, are independent of the shifts of the loss peak in Ch2, controlled by variations of n_{a2}. In both cases, the fiber holes were filled with analytes n_{a1} = 1.33 and n_{a2} = 1.35, respectively.

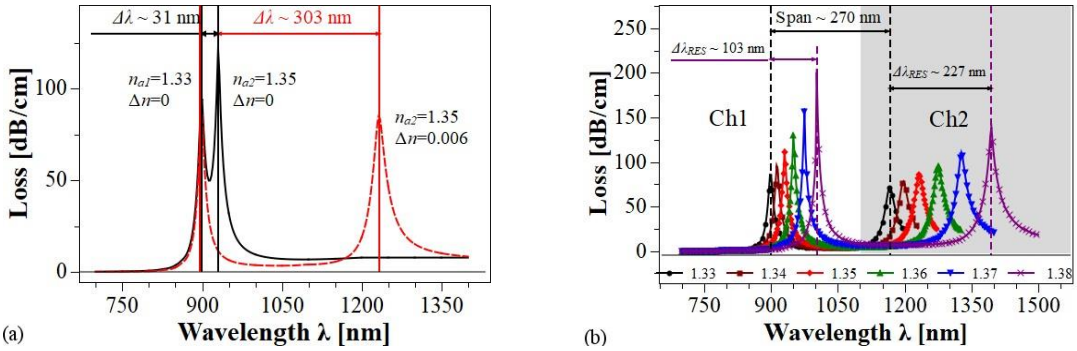

Figure 5-5. (a) Self-referencing and/or multi-analyte operation with d_m = 45 nm, d = 1µm. Black line: d_{d1} = d_{d2}= 0.1µm. Red line*:* d_{d1} = 0.1 µm, d_{d2} = 0.2 µm. (b) Loss spectra with different values of n_a in Ch1 and Ch2. d_m =45 nm, d = 1 µm, d_{d1} = 0.1 µm, Δn_1 = 0; d_{d2} = 0.2 µm, Δn_2 = 0.006

As it is shown in Figure 5-5(b), by combining the effects caused by the variations in the geometrical and optical parameters of the DMDWs, mainly in thicknesses dd_1 and dd_2, and increases in the values of refractive index Δn_1 and Δn_2 of the dielectric layers, it is possible to obtain configurations in which two LRSPPs are excited at different ranges of wavelength and, consequently, for each value of n_a two well-defined loss peaks appear in the loss spectrum. Note that the separation between the two resonance wavelengths for the lower value of n_a is larger than $\Delta\lambda_{RES}$ that occur when n_a changes from a lower to a higher value. Moreover, this behavior could be used to develop an auto-referenced sensor, in which the analyte RI inside one of the side holes, for example, n_{a1} is maintained at a value constant, while the analyte RI inside the other side hole n_{a2} is varied.

Based on the above, the sensor performance for each hole was analyzed separately. Figure 5-6(a) shows that for all the cases studied, the resonant wavelength shifts exhibit a nonlinear feature due to the higher value of n_a enable a strong mode coupling between the fundamental core-guided mode and the LRSPP mode.

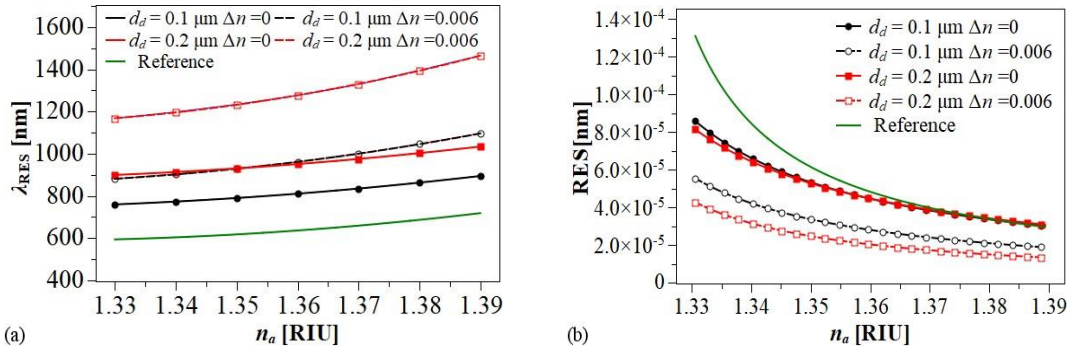

Figure 5-6. (a) λ_{RES}, (b) S_n with d_m = 30, nm, d = 1µm. Black lines: Ch1. Red lines: Ch2. Green line: Ch1 without DMDW (Reference).

Figure 5-6(b) illustrates the sensor sensitivity S_n as a function of the analyte RI. The sensitivity ranges are 1170 nm/RIU to 3300 nm/RIU and 2370 nm/RIU to 7540 nm/RIU for the DMDW with $n_d = n_{co}$ and for the DMDW with $n_d = n_{co} + 0.006$, respectively. In addition, from Figure 5-6(b) it is evident that the sensitivity of the proposed structure depends on the value of the refractive index of dielectric layer n_d in the DMDW.

On the assumption that a 0.1 nm resonance wavelength peak can be detected, the sensor resolution is $RES = 0.1/S_n$. Therefore, the minimum resolutions that can be achieved for the above conditions are 3.0×10−5 RIU and 1.3×10−5 RIU, respectively, as shown in Figure 5-7(a). Although the attained maximum sensitivity is not as high as the refractive index sensors based on sophisticated MOFs [20,21,23,24], which as mentioned above demand great technical efforts for their fabrication, we aim to provide new ideas for the development of optical fiber SPP sensors.

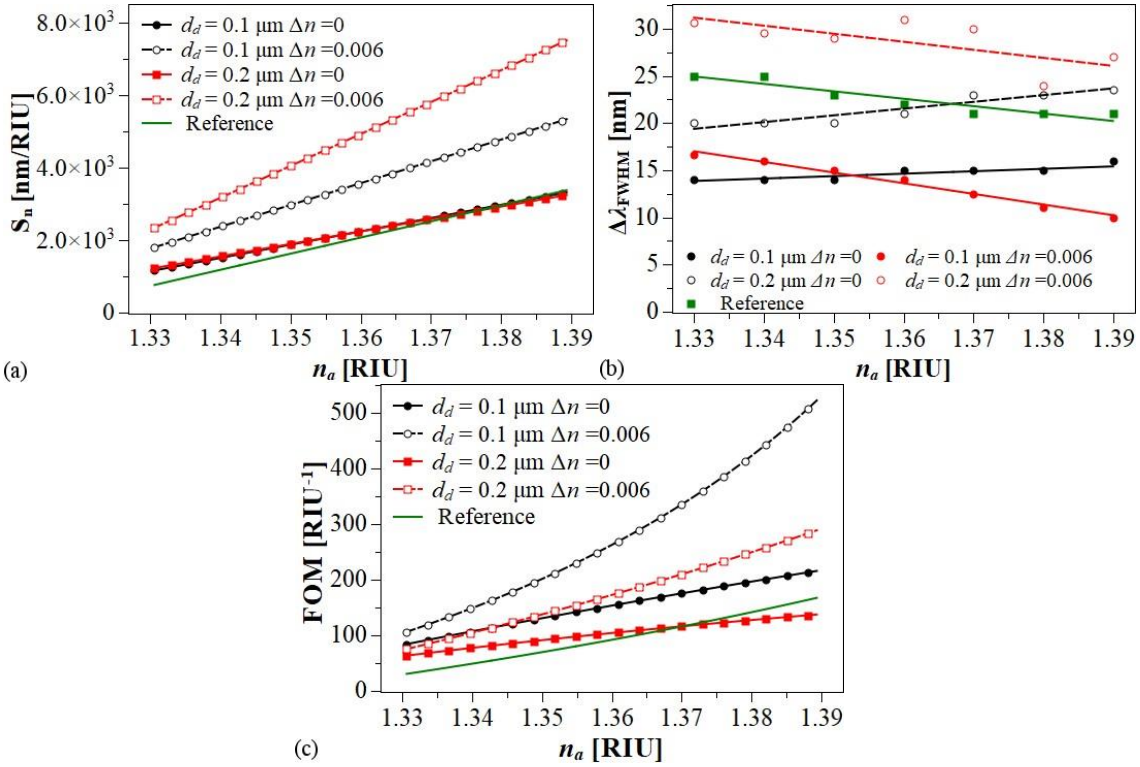

Figure 5-7. Performance of the RI sensor based on LRSPP. (a) S_n, (b) *FWHM* and (c) *FOM* with d_m = 30, nm, d = 1μm. Black lines: Ch1. Red lines: Ch2. Green line: Ch1 without DMDW (Reference).

Here, alternatively, we present a sensor characterized by its simplified microstructure based on the long-range surface plasmon excitation, which may be meaningful for the SPP sensor research. Figure 5-7(b) illustrates the simulation results obtained for the $\Delta\lambda_{FWHM}$. In each case, they were estimated by fitting the spectral loss to a Gaussian function. The behavior of

this parameter has an apparent dependence on the thickness of DMDW dielectric layer d_d. The lowest calculated values were 15.3 nm and 10.3 nm. Despite the fact that thicker films increase the $\Delta\lambda_{FWHM}$, it is also clear that by increasing the refractive index of dielectric films it is possible to significantly improve the S_n values and, consequently, as shown in Figure 5-7(c), the *FOM* is significantly enhanced. According to the above results, it is important to emphasize that variations on the values of n_d and d_d have important effects on sensor performance and, therefore, by controlling them is possible to tune the response of the sensors.

Table 5-1. Comparison of recently reported fiber- optic refractive index sensors based on SPP and LRSPP.

Description	RI Range	S_n (nm/RIU)	*FWHM* (nm)	*RES* (RIU)	*FOM* (RIU^{-1})	Ref Year
SPR sensor based on H-shaped fiber with high RI dielectric layer (TiO_2) on top of the metal layer.	1.32 to 1.33	5 100	NA*	NA*	NA*	[141] 2011
LRSPR sensor based on dielectric/silver-coated hollow fiber.	1.518 to 1.576	6 600	100	1.51×10^{-5}	78	[152]2015
Fiber optic SPR sensor based on MMF-FBG-MMF structure.	1.333 to 1.380	2 557	170	0.2×10^{-6}	15	[153] 2016
SPR-based PCF sensor with NLC core.	1.33 to 1.34	3 900	NA*	2.56×10^{-5}	NA*	[154] 2017
LRSPR sensor using a side polished fiber with the buffer layer of magnesium fluoride.	1.33 to 1.38	3 628	34	2.75×10^{-5}	154	[155] 2017
RI sensor based on a D-shaped PCF with a nanoscale gold belt.	1.2 to 1.4	3 751	NA*	1×10^{-5}	NA*	[156] 2018
SPR-based D-shaped single-mode fiber sensor with a gold grating over the polished fiber surface.	1.33 to 1.34	7 590	NA*	1.31×10^{-5}	NA*	[157] 2019
LRSPR sensor based on GK570/Silver coated hollow fiber (HF) with an asymmetric layer structure.	1.4772 to 1.5116	12 500	83	0.8×10^{-5}	150	[158] 2019
A D-shaped Fiber LRSPR Sensor with High Q-factor.	1.332 to 1.382	3 627.51	81	2.76×10^{-7}	53	[159] 2019
A fiber-based symmetrical LRSPR biosensor with high Q-Factor.	1.33 to 1.38	3 499	76	2.86×10^{-7}	46	[160], [161] 2019

LRSPR in H-shaped MOF with symmetrical dielectric–metal-dielectric waveguide.	1.33 to 1.39	7540	27	1.3×10^{-5}	280	This work

*The authors do not provide this information.

As can be seen in Table 5-1, the results obtained in this work show that sensors based on LRSPP are competitive and outstanding among numerous MOF-based SPP sensor alternatives because it offers a large dynamic detection range, competitive resolution, and improvements in sensitivity and *FOM* without intricate designs and whose manufacture is limited to achievable DMDW structure.

5.4 Summary

In summary, a novel high sensitivity RI sensor based on LRSPP resonance in H-shaped MOF with symmetrical DMDW has been proposed and analyzed. The presence of the DMDW enables the excitation of symmetric and antisymmetric plasmonic modes and facilitates the coupling between the fiber core mode and the symmetric plasmonic mode, improving the sensor parameters. It has been shown that an analyte RI range from 1.33 to 1.39 can be achieved as well as sensitivities of up to 7540 nm/RIU, with *RES* values as low as $1.3\times10-^{5}$RIU and a *FOM* value of 522 RIU−1 at n_a= 1.39. Also, the proposed structure could be used to implement two functionalities: multi-analyte sensing and self-referencing. The operation in the multi-analyte mode enables the detection of two analytes in one aqueous sample. It can also be used in the identification of two different liquid samples with high sensitivity. The results of this work can have a significant impact on the design of MOF-based SPP sensors aimed at striking a good balance between sensor performance and ease of manufacture.

6. THERMO-OPTICALLY TUNABLE POLARIZATION BEAM SPLITTER BASED ON SELECTIVELY GOLD-FILLED DUAL-CORE PHOTONIC CRYSTAL FIBER WITH INTEGRATED ELECTRODES

The content of this chapter is a part of the submitted contribution:

N. D. Gómez-Cardona, C. Jiménez-Durango, J. Usuga-Restrepo, P. Torres, E. Reyes-Vera, Thermo-Optically Tunable Polarization Beam Splitter Based on Selectively Gold-Filled Dual-Core Photonic Crystal Fiber with Integrated Electrodes, Under-Review, November 2020.

6.1 Motivation

In the last two decades, optical fibers have been the preferred transmission medium of metropolitan networks for long-haul terrestrial and transoceanic links, as they have several advantages, such as low loss, large bandwidth, or electromagnetic immunity, in comparison with other technologies. Since 2000, the traffic in optical communications networks has presented an exponential growth, near 50% to 60% per year [161]. Some technological breakthroughs were developed to satisfy the great demand for information and increase transmission rates [162]. One alternative was the implementation of polarization division multiplexing (PDM) in combination with coherent optical systems [163]. To carry out this technique, one of the most important components is the polarization beam splitter (PBS), which is the central element of polarization handling since it split the random polarization state of the input light into two orthogonal polarization states. Several PBS alternatives have been explored in recent years, some of them use multi-mode interference couplers (MMIs) [164], gratings [165]–[169], and symmetric and asymmetrical directional couplers [6] as the core splitting elements. A promising alternative is to use architectures based on dual-core photonic crystal fibers (DC-PCFs). This option offers an additional degree of freedom because by modifying the geometrical parameters of the microstructure it is possible to optimize the optical properties of these devices [165], [170]–[172].

Recently, PBSs based on PCFs with integrated metallic nanowires have been investigated [165], [170]–[172]. In these devices, the excitation of plasmon modes affects both the propagation and losses of the guided modes of the PCF, improving the main characteristics of the PBS, for example, shorter coupling lengths and lower extinction ratios [173].

On the other hand, the ability to split diverse wavelengths of incident lights by using the same PBS provides a great advantage for compact optical systems. Recently, Cheng et al. studied

numerically a PBS based on DC-PCF with a liquid crystal (LC) modulation core [174]. The simulation results reveal that this PBS can reach a bandwidth of 250 nm, which allows operating into the E+S+C+L optical communication bands. Likewise, the temperature sensitivity of the LC helps to tune the operating band of the PBS when the temperature increases from 15°C to 50°C. Wang et al. proposed a PBS based on a DC-PCF filled with nematic LC in [175], which exhibits a bandwidth of 150 nm and a total length of only 890.5 µm. In addition, the capability to tune the response of this device with the electric field and temperature changes was studied. The obtained results show that their configuration is insensitive to electric field changes, but the extinction ratio could be tuned with thermal changes. Next, Wang et al. proposed the first magnetically tunable PBS in [168]. It was designed using a DC-PCF filled with magnetic fluids into the air-holes of the fiber microstructure. It was proven that the magnetic field could be used to control the operation of a PBS with a total length of 8.13 mm and an extinction ratio better than -20 dB. Finally, Wang et al. studied the optical performance of a PBS based on a DC-PCF with elliptical cores, which was controlled through the variation of the refractive index of the hole placed between the two cores [176]–[178]. The performance of this device was analyzed when the central hole was filled with air, water, and glycerol solution at different concentrations. As a result, a PBS is designed with a length of 78 µm when glycerol solution (concentration of 37%) is filled in the central hole. Thus, they achieve a photonic device that operates with good performance at 1550 nm wavelength.

In this chapter, a thermo-optically tunable PBS based on selectively gold-filled DC-PCF with internal electrodes is described and analyzed. The surface plasmon modes excited in the gold-filled holes interact with the guided modes of the DCPCF, thus modifying the main optical parameters of the PBS. Indium was chosen as a metal electrode because of its large thermal expansion coefficient, which allows inducing major changes in the optical properties of PCF compared with other metals [179]. A full-vector finite element method (FEM) is used to investigate the optical properties of the proposed PBS. The tunability capability is achieved by the thermal-stress field induced by the expansion of internal electrodes. The numerical results show that a device with a total length of 1.890 mm can operate at a central wavelength of 1550 nm with a bandwidth of 9 nm. In addition, the thermo-optical analysis shows that the central wavelength can be tuned with sensitivities of -67 pm/°C and 66 pm/°C when the electrodes are arranged horizontally and vertically, respectively. Note that our proposed PBS has remarkable advantages such as ease of implementation and high tuning sensitivity, which ensure its potential applications in compact optical systems, optical switching, and sensing applications.

6.2 Proposed structure and operating principle

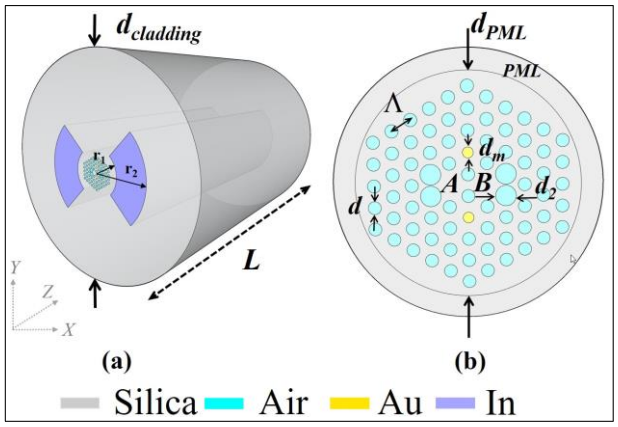

Figure 6-1. (a) Cross-section of the proposed tunable polarization splitter based on gold-filled DC-PCF with internal electrodes. (b) Close view of the central region of the structure. The schematic shows the PBS configuration with the electrodes arranged horizontally,i.e., the electrodes are placed on the x-axis.

Figure 6-1 shows the cross-section of the proposed PBS based on gold-filled DC-PCF with internal stress rods. The cladding central region consists of circular holes arranged in a regular hexagonal lattice with a pitch Λ of 2 µm and a hole diameter d of 1.2 µm. Two air holes on the horizontal line and near to the center of the lattice were removed to create cores *A* and *B*. In addition, two holes, along the vertical axis and in the proximity of the cores, were modified in their diameters and then selectively filled with gold nanowires (with a diameter denoted as d_m, which is initially equal to 0.5 µm). For this purpose, the splicing-based pressure-assisted melt-filling technique can be used, which allows selective filling of individual channels with diameters as small as 120 nm [177], [180]. On the other hand, the lateral air holes on both sides of cores were modified with a diameter d_2 equal to 1.9 µm in order to increase both the confinement of light in the cores and the fiber asymmetry. The bow-tie shaped Indium stress rods, having an inner radius r_1 of 14 µm and an outer radius r_2 of 33 µm, are arranged symmetrically with respect to the center of the fiber. The bow-tie structure, together with its geometric parameters and the thermo-mechanical properties of the different regions of the PCF, entirely determine the nature of the fiber's birefringence [181]. The fiber cladding, with a total diameter of 125 µm, is made of pure silica, facilitating its integration with standard optical fibers, for which both ends of the metal-filled PCF are metal-free to allow for convenient low-loss splicing [182]. The material dispersion of silica is given by Sellmeier's equation [93], while the optical properties of gold are obtained by using the Lorentz-Drude model [177], [180], [181]. The optical properties of Indium are not considered in the model because of the large separation between cores and stress rods.

However, as stated above, Indium has a larger thermal expansion coefficient and when heated it induces thermo-mechanical stress in the center region of the structure, modifying the optical properties of the DC-PCF through elasto-optic phenomenon, as has been experimentally demonstrated in previous studies [178], [180], [183], [184]. Table 6-1 summarized the thermal and mechanical properties of materials used to model the proposed PBS.

The proposed design is based on the use of a PCF with two internal stress rods, which are used to obtain a thermo-optical tuning in the optical response of the PBS. The performance of this PBS is controlled by exploiting the mechanical stresses induced by the thermal expansion of stress rods when they are heated. Therefore, it is possible to induce refractive index changes in the structure and thus controlling the optical response of the PBS [180]. The change of refractive index with the applied thermo-mechanical stress is given by the Neumann–Maxwell equation as [185]:

$$n_x = n_{ox} + C_1\sigma_x + C_2\left(\sigma_y + \sigma_z\right) \tag{6.1a}$$

$$n_y = n_{oy} + C_1\sigma_y + C_2\left(\sigma_x + \sigma_z\right) \tag{6.1b}$$

$$n_z = n_{oz} + C_1\sigma_z + C_2\left(\sigma_x + \sigma_y\right) \tag{6.1c}$$

where n_{0i} and σ_i, with $i = x, y, z$, are the principal refractive indices for the unstressed material and the principal stress components that depend on the applied temperature, respectively. C_1 and C_2 are the stress optic coefficients of silica [177], [180], [181]. The details of all the material parameters can be found in Table 6-1.

Table 6-1. Thermal and mechanical properties of materials used to model the tunable PBS [20].

Properties	Silica	Indium	Gold	Air
Thermal expansion coefficient (K^{-1})	0.5×10^{-6}	32.1×10^{-6}	14.2×10^{-6}	3.23
Young modulus (GPa)	69	12.74	70	10
Poisson ratio	0.17	0.4478	0.44	0.3
Density (Kg/m^3)	2200	73000	19300	1.225
Thermal conductivity (W/m°C)	1.5	81.4	315	0.2624
Stress optical coefficients (m^2/N)	$C1=0.65\times10^{-12}$ $C2=4.20\times10^{-12}$			
Melting Point (°C)	1713	156.6	1064	NA

Note that for using the equations (1) it is necessary to obtain the principal stress components in each point of the entire structure. The two-step computational multiphysics approach

implemented to solve this complex problem was previously detailed and experimentally validated in Refs. [166], [186], considering that the different physical phenomena (thermal, mechanical, and optical) are weakly coupled. The thermo-mechanical analysis is used to estimate the principal stress components, and then using (1), an optical study is conducted using COMSOL Multiphysics v.5.1 to calculate the effective refractive indices of both the DC-PCF supermodes and the excited surface plasmon modes. Likewise, a circular Perfectly Matched Layer (PML) boundary condition was applied to absorb the scattered electromagnetic waves towards the surface [187], [188]. The PML is the most efficient absorption boundary condition and its circular shape is defined in order to improve calculation modes in this type of structure. Therefore, we carry out the convergence test and found that the optimal results were obtained with a PML that has a thickness of 2 μm and an inner diameter (d_{PML}) of 20.8 μm . The whole procedure is performed for different values of the operation temperature T of the device and, for each case, a new set of effective refractive index values is obtained.

The supermode approach of the coupled-mode theory (CMT) is employed to analyze the performance of the polarization beam splitter [188]. When a beam is injected into one core of the PBS, the *x* and *y*-polarization modes of this beam light are coupled separately to the other core of the structure through the evanescent field during light propagation, resulting in the formation of so-called supermodes, so that the mode field of a DC-PCF can be regarded as the superposition of even and odd supermodes [187]. The coupling length, $L_{c,i}$, defined as the length of the fiber in which a complete transfer of power between core A and core B occurs, can be determined as [13, 14]:

$$L_{c,i} = \frac{\lambda}{2\left(n_i^{even} - n_i^{odd}\right)} \tag{6.2}$$

where λ is the free space wavelength of the incident light; n_i^{even} and n_i^{odd} are the effective refractive indices of even and odd supermodes, respectively, and *i* denotes *x*- or *y*-polarization.

Owing to the high asymmetry of the proposed structure, which it is induced by the presence of the metallic nanowire and by the pseudo-elliptical geometry of the two cores, $L_{c,x}$ and $L_{c,y}$ are different. To achieve efficient separation between the two polarization modes in a short physical length *L*, the device must satisfy the condition $L = mL_{c,x} = nL_{c,y}$ (*m* and *n* are positive integers with opposite parity, while *L* is the length of the splitter) [187], [189]. Under the above condition, at the output end of the PBS the orthogonal polarization components of the light will be separated from each other, only the *y*-polarized light will remain in core *A*, while only *x*-polarized light will be coupled into core *B*. In order to obtain a compact PBS, the optimal coupling length ratio (*CLR*), defined as

$$CLR = \frac{L_{c,y}}{L_{c,x}} = \frac{m}{n} \tag{6.3}$$

should be close to 2 ($L_{c,y} > L_{c,x}$), which can be reached by setting appropriate geometrical parameters of the DC-PCF structure.

Because cores A and B are identical and symmetrical with respect to the vertical axis, the normalized output powers, $P_{out,A}$ and $P_{out,B}$, at the output end of the DC-PCF can be calculated as [189]:

$$P^{i}_{out,A}(z) = P^{in}\left[\cos^2\left(\frac{\pi z}{2L_{c,i}}\right)\right]\exp\left(-\alpha^{i}_{l}\right) \tag{6.4}$$

$$P^{i}_{out,B}(z) = P^{in}\left[\sin^2\left(\frac{\pi z}{2L_{c,i}}\right)\right]\exp\left(-\alpha^{i}_{l}\right) \tag{6.5}$$

Finally, the extinction ratio (*ER*) can be calculated as follows [170]:

$$ER = 10\log_{10}\left(\frac{P^{x}_{out}}{P^{y}_{out}}\right) \tag{6.6}$$

where P^{y}_{out} and P^{x}_{out} are the output powers of the *x*- and *y*-polarization at the output end of the input core. Values of *ER* lower (higher) than -20 dB (+20 dB) ensure that the two different polarization states are completely separated.

6.3 Numerical results and discussion

In order to investigate the polarization properties of the proposed DC-PCF splitter, the real part of the effective refractive index, Re{n_{eff}}, and the imaginary part of the effective refractive index, Im{n_{eff}}, are numerically calculated for the second-order SPP modes and the four supermodes. As we can see in Figure 6-2(a), for wavelengths shorter than 860 nm, the *x*- and *y*-polarized supermodes are nearly degenerate. However, at 860 nm, a strong coupling between the even modes and the second SPP modes can be observed, which leads to a split of the effective refractive index of these modes, and the *x*- and *y*-even modes separate more and more as increase the wavelength [190], [191].

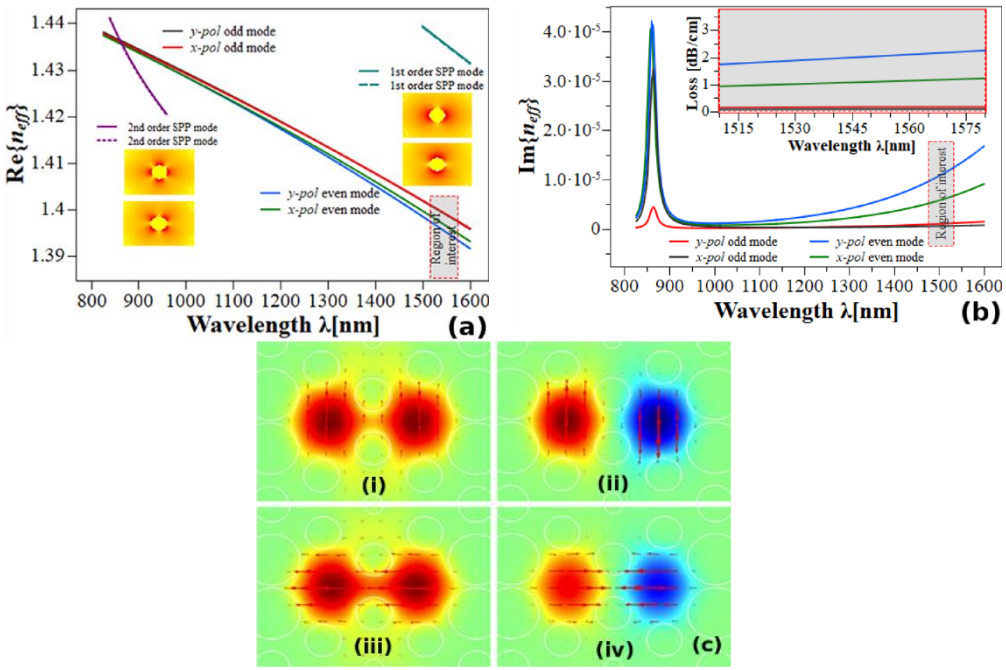

Figure 6-2. (a) Dispersion relations and (b) imaginary part of effective refractive index for the proposed DC-PCF PBS at room temperature. (c) Electric field distributions of the (i, iii) even and (ii, iv) odd modes at 1550 nm. The inset in (b) shows the calculated loss spectra in the wavelength range of interest.

The odd modes are not strongly affected by the 2nd SPP modes [see Figure 6-2(b)] because they are significantly better confined in cores *A* and *B*, as evidenced in Figure 6-2(c). Note that in the region of interest in Fig. 2(a) (1515-1575 nm), where the *y*-even mode achieves a maximum loss of approximately 2.2 dB/cm, as can be seen from the loss spectra of the inset in Figure 6-2 (b), the difference in the effective refraction indices of the *y*-even and *y*-odd modes is much greater than that of the *x*-polarized one, which will greatly change the coupling characteristic between two guided core modes. This feature can be used for polarization beam splitters. It is important to note that the effective refractive index of the first SPP mode is much higher than that of the core supermodes, so that it is quite difficult for the resonance coupling from the SPP mode to the core supermodes. Besides, third and higher-order SPP modes are not shown in this figure due to their weak interaction with the core supermodes

Figure 6-3(a) shows the wavelength dependence of the coupling length of the *x*- and *y*-polarized modes in the gold-filled DC-PCF with the Indium stress rods arranged horizontally. It is clear that the coupling between both cores is stronger for the *x*-polarized mode than for the *y*-polarized mode. This figure also shows the thermal-optics effect induced by the expansion of the stress rods when the PBS is submitted to thermal changes in the range from 25°C to 125°C (only results for three temperature values are shown for clarity). Note that,

within the evaluated spectral range, the coupling lengths for *x* and *y* polarizations are slightly affected by the thermal changes. As a consequence, the proposed configuration does not present significant changes in the coupling length ratio (*CLR*) parameter, keeping values near 1.5, as is shown in Figure 6-3(b). Likewise, the device length could be kept constant, which facilitates its implementation in compact optical systems.

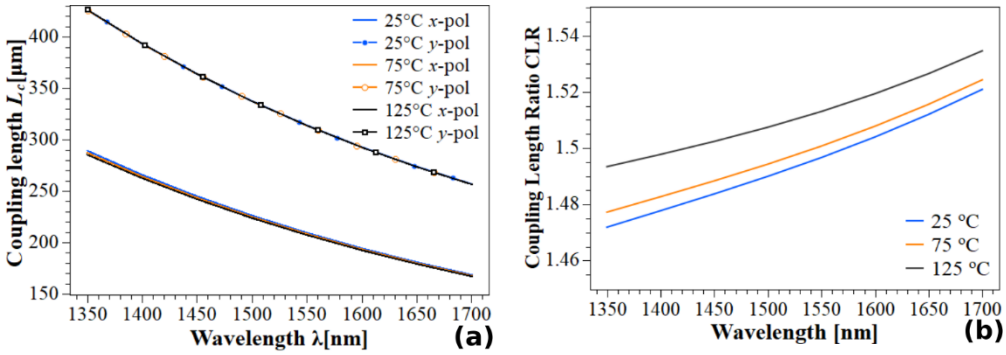

Figure 6-3. Wavelength dependence of (a) coupling length and (b) *CLR* parameter of the proposed PBS with the internal stress rods arranged horizontally as a function of temperature.

Equations (7) and (8) were used to obtain the optimal length of the proposed PBS at 1550 nm. For calculating the output powers, it was assumed that the incident light was launched into core *A*. Figure 6-4(a) shows the normalized power transmission for the input core as a function of the wavelength for the proposed PBS at room temperature. Figure 6-4(b) shows that at room temperature (T = 25°C) the normalized power difference between both *x*- and *y*-polarized light are effectively separated from each other by a distance *L* of 1.890 mm (highlighted by the grey dashed line). Thus, the proposed structure was optimized (for more details see [15]) to operate at 1550 nm since at this wavelength both polarization states are completely split.

For example, when the light is injected into core *A*, note that the *x*-polarization component is completely in the core *B*, while the *y*-polarization component is in core *A*. Thus, we can evidence that at this wavelength the device can split the two polarization states.

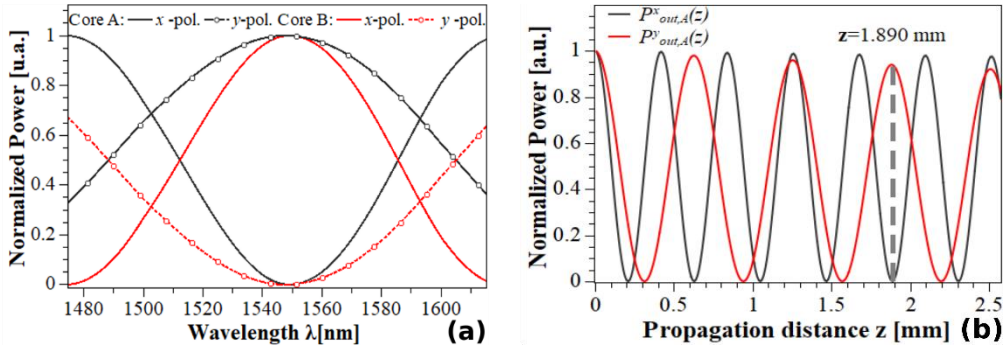

Figure 6-4. (a) Wavelength dependence of the normalized power for a device with a length of 1.890 mm at room temperature with the Indium stress rods arranged horizontally. (b) Normalized power variation along with the propagating distance at λ=1550 nm.

The *ER* is one of the most important parameters in this kind of photonic device, then the results of Figure 6-4 in combination with Equation (6) are employed to evaluate this parameter. Figure 6-5(a) shows the *ER* at different temperatures in the *C*-band for a device with a total length of 1.890 mm and two Indium stress rods arranged horizontally. The results evidence that the proposed PBS operates at 1549.05 nm and the extinction ratio can reach -83.2 dB at room temperature. Moreover, the PBS exhibits a well-defined bandwidth of 9 nm, which makes it suitable to be employed as a tunable device. The results illustrated in Figure 6-5(a) also reveal that the operating wavelength shifts to shorter wavelengths when the temperature increases, demonstrating the tuning capacity of this PBS. Likewise, the bandwidth and the *ER* are not significantly affected by the thermal expansion of the internal stress rods, for example, the bandwidth in all cases remains almost constant with a variation of just 0.2 nm, while the *ER* presents a variation of 16.5 dB. The same analysis was carried out for a PBS with the Indium stress rods arranged vertically. In this case, one can evidence that the PBS presents a similar behavior, however, the operating wavelength shifts to larger wavelengths as the temperature increases. In comparison with the configuration with the stress rods arranged horizontally; see Figure 6-5(b), this configuration presents variations of 0.2 nm and 18.1 dB for the bandwidth and the *ER*, respectively. This small difference between the simulation results evidence that both configurations are very stable in the studied temperature range, which was expected due that, as previously demonstrated in Figure 6-4(b), the *CLR* is slightly affected by thermal changes.

As already explained, Equation (1) allows obtaining the distribution of the refractive index change within PCFs with integrated stress rods. As an example, the distributions of the refractive index change, Δn, of the selectively gold-filled DC-PCFs at 125°C and operating at a wavelength of 1550 nm are illustrated in Figure 6-6(a). Figure 6-6(a) shows that the refractive index change is governed by the distribution of the holes in the microstructure. Likewise, it is evident the strong dependence of the refractive index changes with the position of both stress rods (vertical and horizontal).

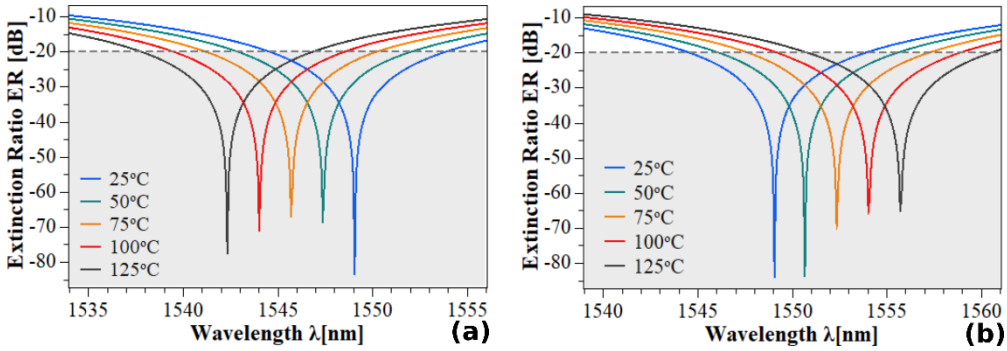

Figure 6-5. Wavelength dependence of the extinction ratio (ER) for the proposed polarization splitter with internal stress rods arranged (a) horizontally and (b) vertically. In both cases, the analysis was carried out in the C-band for a 1.890 mm long device while undergoing thermal changes from 25°C to 125°C.

To assess the relationship between refractive index change and PBS operation, Fig 6(b) shows the Δn over the entire operating temperature range of a test point p corresponding to the center of core *A*, see Fig. 6(a). Note that the $\Delta n_{x,y}$ in each case presents a linear dependence with the temperature. The Δn of the electrode axis (slow axis) has an opposite sign to the Δn exhibited by the fast axis (straight line perpendicular to the electrode axis).

Thus, we corroborate that the operation of the PBS based on gold-filled DC-PCF with integrated stress rods depends on the arrangement of the stress rods. Note that we have restricted ourselves to configurations in which the Indium stress rods are arranged horizontally and vertically.

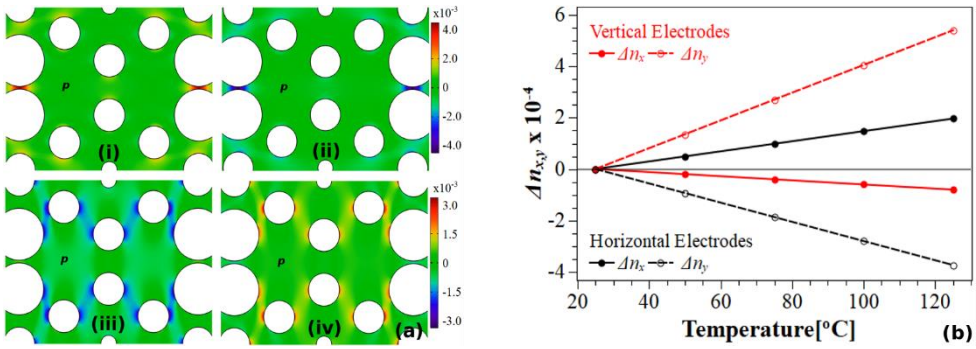

Figure 6-6. (a) Refractive index change within the DC-PCF with In stress rods: (i) Δn_x and (ii) Δn_y for the PCF with horizontal stress rods; (iii) Δn_x and (iv) Δn_y for the PCF with vertical stress rods. b) $\Delta n_{x,y}$ as a function of the temperature of the point p corresponding to the center of core *A*.

When the stress rods have an angular orientation with respect to the main axes, see Figure 6-1, new precautions must be taken in that the principal axes of the fiber must be accurately aligned with certain transverse device axes to avoid polarization cross-coupling [171].

The temperature dependence of the operating wavelength for both configurations is depicted in Figure 6-7. Clearly, the response of the configuration with the internal stress rods arranged horizontally presents a linear dependence with the temperature. In this case, the device has a temperature sensitivity of -67 pm/°C. On the other hand, the PBS configuration with the internal stress rods arranged vertically has a temperature sensitivity of approximately 66 pm/°C. This feature makes it a thermo-optically tunable PBS very interesting to be employed in optic communications systems that employ PDM technique, as can be seen from Table 6-2, which summarizes the different all-fiber PBS configurations with the capacity to be controlled to develop flexible networks. From this table, it is clear that the proposed tunable PBS is competitive with previously reported PBS.

Table 6-2. Comparison of recently reported polarization beam splitters based on dual-core PCFs

Tunable	Length (mm)	λ [um]	Bandwidth [nm]	CLR	Reference
No	1.746	1327/15um50	55 (>12 dB)	1.166	[173]
No	0.175	1405/1550	250 (<-20 dB)	2.000	[170]
No	0.255	1550	560 (>20 dB)	1.997	[174]
Yes	0.890	1550	150 (>20 dB)	1.992	[192]
No	1.079	1550	70 (>20 dB)	2.000	[175]
Yes	8.130	1550	NA	1.250	[168]
No	0.078	1550	44 (>15 dB)	1.310	[168]
Yes	1.890	1550	9 (<-20 dB)	1.500	This Work

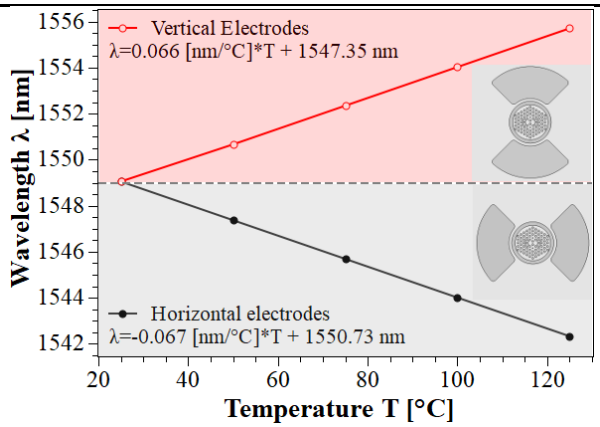

Figure 6-7. Dependence of the operating wavelength as a function of the applied temperature for the PBS based on gold-filled dual-core PCF controlled by integrated stress rods arranged horizontally and vertically.

6.4 Summary

In summary, we have proposed the first thermo-optically tunable polarization beam splitter based on selectively gold-filled DC-PCF with internal stress rods by exploiting the thermal-stress field induced by the expansion of Indium stress rods. Two gold wires have been added selectively to fill two holes in the fiber to produce a compact length with high-performance polarization splitter. The optical properties of the proposed polarization splitter were investigated by using a full-vector finite element method. The splitter exhibits a coupling length ratio of 1.5 with slight changes when the temperature is increased, so the bandwidth and extinction ratio of the device are not significantly affected during the tuning process. The novel polarization splitter has a short length of 1.890 mm and a bandwidth of about 9 nm with a high extinction ratio of -83.2 dB and tuning sensitivities of -67 pm/°C and 66 pm/°C when the internal stress rods are arranged horizontally and vertically, respectively. Because of its excellent performance, we believe that this type of polarization splitter could be widely useful in compact optical systems, optical switching, and sensing applications, respectively.

7. CONCLUSIONS AND FUTURE WORK

7.1 Conclusion

Some of the proposed MOFs have properties that allow easy integration with standard optical fibers, among other reasons because their structures match the geometry as well as the propagation parameters of the light of an SMF fiber. This match is reached because the MOFs have been designed to have a solid core and large holes around it. As shown in preceding chapters, these geometrical and optical characteristics facilitate the post-processing of these kinds of optical fibers, providing new and simple ways to excitation surface plasmon polaritons. This all-around phenomenon was used for recasting regular MOFs into devices that can modify the propagation properties of the light. Moreover, in contrast with other structures, the dimensions of the proposed and analyzed devices, turning these into platforms for the design of photonic circuits on a millimetric-scale.

To reach this goal, it is important either the excitation of high order SPP modes or long-range SPPs, primarily because the propagation length of these is larger than other surface plasmons. Some configurations and strategies for doing it are discussed in the sections of the third chapter of this thesis. There, the main configurations to excite surface plasmon polaritons in dielectric-metallic interfaces or dielectric-meatal-dielectric waveguides. The last concept is broadened to include multilayer stacks, a promising configuration that allows the excitation of LRSPPs and facilitates the interaction of them with the external medium. The next sections deal with the excitation of SPPs in metallic nanostrips and metallic nanowires, two well known and interesting structures, which unlike infinite width films, support a finite number of SPP modes. This chapter concludes with a first approximation to the excitation of SPPs in circular optical waveguides, by the deposition of a metallic layer on the flat side of a D-shaped optical fiber. The theoretical models here discussed, as a whole, open up the possibility to propose new designs and a best understood of the involved phenomena.

Although the excitation of surface plasmon polariton has indeed been used in a substantial number of devices, the majority of proposed structures based on optical waveguides and optical fibers addresses this phenomenon considering that there is only one possible interaction between the fundamental mode of the dielectric waveguide and only one surface polariton mode. However, as shown in the fourth chapter of this thesis, modifying the optical properties of the material that surround the metal layer or the optical properties of the dielectric waveguide, in our cases the MOF, it is possible to achieve conditions that facilitate the interaction between the fundamental mode of the MOF and the superior surface plasmon modes. This approach shows that the optical properties of the fundamental mode of the MOF could be modified by multiple resonances leading, for instance, to the occurrence of several

loss peaks in the optical transmission spectrum of the device. Following this approach, the performance of a refractive index sensor based on suspended core MOF with large holes was evaluated but analyzing the shifts in the resonance peaks for superior order plasmon modes. Obtained results showed that, under adequate conditions, the main parameters of the device are improved. Furthermore, it could be operated in multi-analyte sensing and self-referencing mode.

As stated above, the properties of the materials that surround the metal layer determine how the surface plasmon modes are excited and how their evanescent fields interact with the most external regions of the structure. As established in the fifth chapter, using multilayer structures underneath and on top of the metal layer, it is possible to tune the resonant wavelength, and shifting it towards large wavelengths, which are of interest in optical communications and biological sensing. Furthermore, in the third chapter, it was showed that this kind of structure is very attractive because it provides an easy way for manipulating the hybrid modes, choosing the side of the metal layer in which the plasmon mode will be excited. For example, in the devices analyzed in the fifth chapter, adding a symmetric dielectric-metal-dielectric waveguide on top of the surface of the MOF side holes, the transmission spectra obtained show narrower and well-defined peaks. Consequently, the resolution and sensitivity were improved, and the figure of merit (Q-factor) of the device was enhanced significantly.

Another structure analyzed consists of a MOF with internal metal nanowires. This structure, proposed and analyzed in the sixth chapter, have large differences from those analyzed in the previous chapters because the plasmon modes excited in the metal-filled holes affect the polarized modes of the two cores of the MOF selectively. Besides, the bow-tie shaped Indium thermal-stress rods, located symmetrically on both sides of the lattice, provide a way to modify the optical properties of the guides modes into the cores, and subsequently, how these interact with the plasmon modes. This structure was then used as the base for designing a thermo-optically tunable polarization beam splitter with a length of 1.89 mm and a bandwidth of 9 nm, a wavelength operating range of 16 nm, an extinction ratio close to -83dB, and average tuning sensitivities of 66.5pm/ºC.

Overall, this doctoral thesis considered three different ways for facilitating the excitation of hybrid modes, all these, based on increasing the coupling between the guided modes of a MOF and the plasmon modes excited on a metal-dielectric interface. In the first of them, the geometry and optical properties of the MOF were modified in order to facilitate the interaction of the fundamental mode of MOF with the superior order plasmon modes. The second facilitates the interaction with plasmon modes using a dielectric-metallic-dielectric waveguide. Finally, in the third case, the main geometrical parameters of the lattice that form the cores of the MOF and the position of metal-filled holes were chosen so that all the mode

coupling occurs far from the resonance condition. To show the effectiveness of the proposed strategies, these were used as a base for designing and numerically analyzing several devices, which showed improvements in the key parameters and performance when compared with similar devices.

7.2 Future Work

Despite the results reported in this thesis are in general promising, it is imperative to make experimental progress that allows for demonstrating the real use of the proposed strategies. In particular, the implementation and use of chemical wet techniques for post-processing commercial microstructured optical fibers could be a way for getting structures that facilitate the deposition of dielectric layers underneath and on top of the metal layer. Understanding these techniques would allow possible to carry out the experimental evidence of the proposed structure in chapter 4. In fact, our research group is working along with other research groups on chemical routes and techniques based on dip coating methods for the deposition of polymeric layers and sol-gel processes to deposit dielectric layers of metal oxides.

About computational methods used in this doctoral thesis, although the FEM is the best numerical technique to accurately analyze and found the modes supported by the transversal section of structures of arbitrary shapes (such as MOFs), this by itself, does not appear to be the best method to describe the propagation of light into 3D structures. Therefore, it is imperative combining FEM with other numerical techniques that allow a better understanding of the behavior of the propagation of hybrid modes, especially in those devices in which the light is continuously transferred between modes.

Based on the above, the hybrid modes are an interesting area of study and a promising platform for the development of photonic devices. Therefore, the research group expects to continue on this research line, and thus, to contribute to the best understanding of these.

8. REFERENCES

[1] T. Takano and J. Hamasaki, “Propagating modes of a metal-clad dielectric-slab waveguide for integrated optics,” *IEEE Journal of Quantum Electronics*, vol. 7, no. 6, p. 1964, 1971, doi: 10.1109/JQE.1971.1076693.

[2] V. V. Cherny, “Confined guided modes in W-fibre with square core,” *Electronics Letters*, vol. 15, no. 10, p. 281, 1979, doi: 10.1049/el:19790200.

[3] F. P. Kapron, “Erratum: Maximum information capacity of fibre-optic waveguides,” *Electronics Letters*, vol. 13, no. 9, p. 272, 1977, doi: 10.1049/el:19770197.

[4] D. Marcuse, *Theory of Dielectric Optical Waveguides*. 1991.

[5] G. P. Agrawal, *Fiber-Optic Communication Systems: Fourth Edition*, Third Edit., vol. 6. John Wiley & Sons, 2011.

[6] A. Ihaya, H. Furuta, and H. Noda, “Thin-film Optical Directional Coupler.,” *Proceedings of the IEEE*, vol. 60, no. 4, pp. 470–471, 1972, doi: 10.1109/PROC.1972.8676.

[7] M. G. F. Wilson and G. A. Teh, “Tapered Optical Directional Coupler,” *IEEE Transactions on Microwave Theory and Techniques*, vol. 23, no. 1, 1975, doi: 10.1109/TMTT.1975.1128508.

[8] T. Matsumoto, “Polarisation-independent optical circulator coupled with multimode fibres,” *Electronics Letters*, vol. 16, no. 1, p. 8, 1980, doi: 10.1049/el:19800007.

[9] A. Shibukawa and M. Kobayashi, “Compact optical circulator for near-infrared region,” *Electronics Letters*, vol. 14, no. 25. p. 816, 1978, doi: 10.1049/el:19780551.

[10] a. Yi-Yan, J. a. H. Wilkinson, and C. D. W. Wilkinson, “Optical waveguide filters for the visible spectrum,” *IEE Proceedings H Microwaves, Optics and Antennas*, vol. 127, no. 6, p. 335, 1980, doi: 10.1049/ip-h-1.1980.0071.

[11] Z. K. Ioannidis, I. P. Giles, and C. Bowry, “Liquid crystal all-fibre optical polariser,” *Electronics Letters*, vol. 24, no. 23. p. 1453, 1988, doi: 10.1049/el:19880993.

[12] K. Rollke and W. Sohler, “Metal-clad waveguide as cutoff polarizer for integrated optics,” *IEEE Journal of Quantum Electronics*, vol. 13, no. 4, 1977, doi: 10.1109/JQE.1977.1069317.

[13] M. Papuchon and S. Vatoux, “Integrated optical polariser on LiNbO3:Ti channel waveguides using proton exchange,” *Electronics Letters*, vol. 19, no. 16. p. 612, 1983, doi: 10.1049/el:19830417.

[14] W. Lin, H. Li, Y. J. Chen, M. Dagenais, and D. Stone, “Dual-channel-spacing phased-array waveguide grating multi/demultiplexers,” *IEEE Photonics Technology Letters*, vol. 8, no. 11, pp. 1501–1503, 1996, doi: 10.1109/68.541563.

[15] W. Tomlinson and G. Aumiller, “Optical multiplexer for multimode fiber transmission systems,” *IEEE Journal of Quantum Electronics*, vol. 13, no. 9, p. 1976, 1977, doi: 10.1109/JQE.1977.1069593.

[16] A. Neyer, “Integrated-optical multichannel wavelength multiplexer for monomode systems,” *Electronics Letters*, vol. 20, no. 18, p. 744, 1984, doi: 10.1049/el:19840509.

[17] S. K. Khijwania and B. D. Gupta, “Maximum achievable sensitivity of the fiber optic evanescent field absorption sensor based on the U-shaped probe,” *Optics Communications*, vol. 175, no. 1, pp. 135–137, 2000, doi: 10.1016/S0030-4018(00)00465-X.

[18] A. D. Kersey and A. Dandridge, “Applications of fiber-optic sensors,” *IEEE transactions on components, hybrids, and manufacturing technology*, vol. 13, no. 1, pp. 137–143, 1990, doi: 10.1109/33.52861.

[19] B. Culshaw, “Optical Fiber Sensor Technologies: Opportunities and - Perhaps - Pitfalls,” in *Journal of Lightwave Technology*, 2004, vol. 22, no. 1, pp. 39–50, doi: 10.1109/JLT.2003.822139.

[20] H. Ishigaki, T. Oya, M. Itoh, a. Hida, and K. Iwata, “New measuring system for the distribution of a magnetic force by using an optical fiber,” *Review of Scientific Instruments*, vol. 64, no. 1, pp. 243–246, 1993, doi: 10.1063/1.1144444.

[21] A. Wang, S. Member, S. He, X. Fang, X. Jin, and J. Lin, “Optical Fiber Pressure Sensor Based on Pho toelasticity and its Application,” *Journal of Lightwave Technology*, vol. 10, no. 10, 1992.

[22] H. Golnabi, “Design and operation of different optical fiber sensors for displacement measurements,” *Review of Scientific Instruments*, vol. 70, no. 6, p. 2875, 1999, doi: 10.1063/1.1149812.

[23] a. Buffa, G. Perrone, and a. Vallan, “A Plastic Optical Fiber Sensor for Vibration Measurements,” *2008 IEEE Instrumentation and Measurement Technology Conference*, pp. 1–5, 2008, doi: 10.1109/IMTC.2008.4547259.

[24] J. Homola and J. Dot’lek, *Surface plasmon resonance based sensors*, vol. 4. Springer, 2006.

[25] V. M. Shalaev and S. Kawata, *Nanophotonics with Surface Plasmons*. 2007.

[26] R. F. Oulton, G. Bartal, D. F. P. Pile, and X. Zhang, “Confinement and propagation characteristics of subwavelength plasmonic modes,” *New Journal of Physics*, vol. 10, pp. 0–14, 2008, doi: 10.1088/1367-2630/10/10/105018.

[27] A. v Krasavin and A. v Zayats, “Silicon-based plasmonic waveguides.,” *Optics express*, vol. 18, no. 11, pp. 11791–11799, 2010, doi: 10.1364/OE.18.011791.

[28] Y. Song, J. Wang, Q. Li, M. Yan, and M. Qiu, “Broadband coupler between silicon waveguide and hybrid plasmonic waveguide,” *Opt. Express*, vol. 18, pp. 13173–13179, 2010.

[29] S. I. Bozhevolnyi, V. S. Volkov, E. Devaux, J.-Y. Laluet, and T. W. Ebbesen, “Channel plasmon subwavelength waveguide components including interferometers and ring resonators.,” *Nature*, vol. 440, no. 7083, pp. 508–511, 2006, doi: 10.1038/nature04594.

[30] S. Wang, V. Vaidyanathan, and B. Borden, “Polymer optical channel waveguide components fabricated by using a laser direct writing system,” *Journal of Applied Science & …*, pp. 47–52, 2009, [Online]. Available: https://library.rit.edu/oajournals/index.php/jaset/article/view/215.

[31] V. S. Volkov, S. I. Bozhevolnyi, E. Devaux, and T. W. Ebbesen, “Compact gradual bends for channel plasmon polaritons.,” *Optics express*, vol. 14, no. 10, pp. 4494–4503, 2006, doi: 10.1364/OE.14.004494.

[32] S. I. Bozhevolnyi, “Effective-index modeling of channel plasmon polaritons.,” *Optics express*, vol. 14, no. 20, pp. 9467–9476, 2006, doi: 10.1364/OE.14.009467.

[33] A. Boltasseva, V. S. Volkov, R. B. Nielsen, E. Moreno, S. G. Rodrigo, and S. I. Bozhevolnyi, “Triangular metal wedges for subwavelength plasmon-polariton guiding at telecom wavelengths.,” *Optics express*, vol. 16, no. 8, pp. 5252–5260, 2008, doi: 10.1364/OE.16.005252.

[34] Y. Bian, Z. Zheng, Y. Liu, J. Liu, J. Zhu, and T. Zhou, “Hybrid wedge plasmon polariton waveguide with good fabrication-error-tolerance for ultra-deep-subwavelength mode confinement,” *Optics Express*, vol. 19, no. 23, p. 22417, 2011, doi: 10.1364/OE.19.022417.

[35] A. Chandran, E. S. Barnard, J. S. White, and M. L. Brongersma, “Metal-dielectric-metal surface plasmon-polariton resonators,” *Physical Review B - Condensed Matter and Materials Physics*, vol. 85, no. 8, pp. 1–9, 2012, doi: 10.1103/PhysRevB.85.085416.

[36] F. Liu *et al.*, “Hybrid three-arm coupler consisted of long range surface plasmon polariton and dielectric waveguides,” *Journal of Lightwave Technology*, vol. 26, no. 24, pp. 3872–3882, 2008, doi: 10.1109/JLT.2008.928397.

[37] R. Wan, F. Liu, X. Tang, Y. Huang, and J. Peng, “Vertical coupling between short range surface plasmon polariton mode and dielectric waveguide mode,” *Applied Physics Letters*, vol. 94, no. 14, 2009, doi: 10.1063/1.3111001.

[38] L. Gao, L. Tang, F. Hu, R. Guo, X. Wang, and Z. Zhou, “Active metal strip hybrid plasmonic waveguide with low critical material gain,” *Optics Express*, vol. 20, no. 10, p. 11487, 2012, doi: 10.1364/OE.20.011487.

[39] M. Z. Alam, F. Bahrami, J. S. Aitchison, and M. Mojahedi, “Analysis and optimization of hybrid plasmonic waveguide as a platform for biosensing,” *IEEE Photonics Journal*, vol. 6, no. 4, 2014, doi: 10.1109/JPHOT.2014.2331232.

[40] B. Fan *et al.*, “Integrated sensor for ultra-thin layer sensing based on hybrid coupler with short-range surface plasmon polariton and dielectric waveguide,” *Applied Physics Letters*, vol. 102, no. 6, pp. 244–246, 2013, doi: 10.1063/1.4792319.

[41] G. Wang *et al.*, “Highly sensitive D-shaped photonic crystal fiber biological sensors based on surface plasmon resonance,” *Optical and Quantum Electronics*, vol. 48, no. 1, p. 46, Jan. 2016, doi: 10.1007/s11082-015-0346-4.

[42] G. Osowiecki, E. Barakat, A. Naqavi, and H. P. Herzig, “Localized biomolecular sensing enabled through plasmonic nanocavities,” in *Biophotonics: Photonic Solutions for Better Health Care IVProc. SPIE 9129, Biophotonics: Photonic Solutions for Better Health Care IV, 91292B (May 8, 2014)*, 2014, vol. 9129, p. 91292B, doi: 10.1117/12.2052822.

[43] F. F. Lu *et al.*, “Surface plasmon polariton enhanced by optical parametric amplification in nonlinear hybrid waveguide.,” *Optics express*, vol. 19, no. 4, pp. 2858–2865, 2011, doi: 10.1364/OE.19.002858.

[44] a. Melikyan *et al.*, “High-speed plasmonic phase modulators,” *Nature Photonics*, vol. 8, no. 3, pp. 229–233, 2014, doi: 10.1038/nphoton.2014.9.

[45] T. Nikolajsen, K. Leosson, and S. I. Bozhevolnyi, “Surface plasmon polariton based modulators and switches operating at telecom wavelengths,” *Applied Physics Letters*, vol. 85, no. 24, pp. 5833–5835, 2004, doi: 10.1063/1.1835997.

[46] R. S. Windeler, J. L. Wagener, and D. J. DiGiovanni, “Silica-air microstructured fibers: properties and applications,” *OFC/IOOC . Technical Digest. Optical Fiber Communication Conference, 1999, and the International Conference on Integrated Optics and Optical Fiber Communication*, vol. 4, no. 908, pp. 106–107, 1999, doi: 10.1109/OFC.1999.766009.

[47] M. Erdmanis, D. Viegas, M. Hautakorpi, S. Novotny, J. L. Santos, and H. Ludvigsen, “Comprehensive numerical analysis of a surface-plasmon-resonance

sensor based on an H-shaped optical fiber," *Opt. Express*, vol. 19, pp. 13980–13988, 2011.

[48] Y. Zhang, C. Zhou, L. Xia, X. Yu, and D. Liu, "Wagon wheel fiber based multichannel plasmonic sensor," *Opt. Express*, vol. 19, p. 22863, 2011.

[49] N. Gómez-cardona and P. Torres, "Sensitivity Analysis of SPR Sensors Based on Suspended- core Microstructured Optical Fibers," in *Latin America Optics and Photonics Conference*, 2012, no. 1, pp. 12–14, doi: 10.1364/LAOP.2012.LS4C.2.

[50] P. Berini, "Plasmon-polariton waves guided by thin lossy metal films of finite width: Bound modes of symmetric structures," *Physical Review B*, vol. 61, no. 15, pp. 10484–10503, 2000, doi: 10.1103/PhysRevB.61.10484.

[51] P. Berini, "Plasmon-polariton waves guided by thin lossy metal films of finite width: Bound modes of asymmetric structures," *Phys. Rev. B*, vol. 63, p. 125417, 2001.

[52] A. Méndez, T. F. Morse, C. R. Kurkjian, and M. John Matthewson, *Specialty Optical Fibers Handbook*. 2007.

[53] D. Marcuse, *Light Transmission Optics*. VAN NOSTRAND REINHOLD COMPANY, 1982.

[54] T. a Birks, J. C. Knight, and P. S. Russell, "Endlessly single-mode photonic crystal fiber.," *Optics letters*, vol. 22, no. 13, pp. 961–963, 1997, doi: 10.1364/OL.22.000961.

[55] A. Varshney, "Propagation Characteristics of Photonic Crystal Fiber: Scalar Effective Index Method and Fully Vectorial Effective Index Method," *Adv. Studies Theor. Phys*, vol. 1, no. 2, pp. 75–85, 2007, [Online]. Available: http://www.m-hikari.com/astp/astp2007/astp1-4-2007/varshneyASTP1-4-2007.pdf.

[56] A. Varshney, "Propagation Characteristics of Photonic Crystal Fiber: Scalar Effective Index Method and Fully Vectorial Effective Index Method," *Adv. Studies Theor. Phys*, vol. 1, no. 2, pp. 75–85, 2007.

[57] K. Saitoh and M. Koshiba, "Numerical modeling of photonic crystal fibers," *Journal of Lightwave Technology*, vol. 23, no. 11, 2005, doi: 10.1109/JLT.2005.855855.

[58] I. a. Goncharenko and M. Marciniak, "Photonic crystal fibre characterisation with the method of lines," *Journal of Telecommunications and Information Technology*, vol. 1, pp. 106–111, 2004, [Online]. Available: http://www.itl.waw.pl/czasopisma/JTIT/2004/1/106.pdf.

[59] D. Mogilevtsev, T. a. Birks, and P. S. J. Russell, “Localized function method for modeling defect modes in 2-D photonic crystals,” *Journal of Lightwave Technology*, vol. 17, no. 11, pp. 2078–2081, 1999, doi: 10.1109/50.802997.

[60] T. L. Wu and C. H. Chao, “An efficient approach for calculating the dispersions of photonic-crystal fibers: Design of the nearly zero ultra-flattened dispersion,” *Journal of Lightwave Technology*, vol. 23, no. 6, pp. 2055–2061, 2005, doi: 10.1109/JLT.2005.849929.

[61] F. Brechet, “Complete Analysis of the Characteristics of Propagation into Photonic Crystal Fibers, by the Finite Element Method,” *Optical Fiber Technology*, vol. 6, no. 2, pp. 181–191, 2000, doi: 10.1006/ofte.1999.0320.

[62] P. Crystal, K. Saitoh, M. Koshiba, and S. Member, “Full-Vectorial Imaginary-Distance Beam Propagation Method Based on a Finite Element Scheme :,” *IEEE Journal of Quantum Electronics*, vol. 38, no. 7, pp. 927–933, 2002, doi: 10.1109/JQE.2002.1017609.

[63] “Comsol Multiphysics.” www.comsol.com (accessed Apr. 24, 2015).

[64] P. Berini, “Long-range surface plasmon polaritons,” *Adv. Opt. Photon.*, vol. 1, pp. 484–588, 2009.

[65] N. Skivesen, *Metal-Clad Waveguide Sensors*, vol. 15, no. September. 2005.

[66] P. Berini, “Plasmon-polariton modes guided by a metal film of finite width bounded by different dielectrics,” *Opt. Express*, vol. 7, pp. 329–335, 2000.

[67] P. Berini, “Plasmon-polariton waves guided by thin lossy metal films of finite width: Bound modes of symmetric structures,” *Physical Review B*, vol. 61, no. 15, pp. 10484–10503, 2000, doi: 10.1103/PhysRevB.61.10484.

[68] M. Liu *et al.*, “A graphene-based broadband optical modulator.,” *Nature*, vol. 474, no. 7349, pp. 64–67, 2011, doi: 10.1038/nature10067.

[69] A. Boltasseva and S. I. Bozhevolnyi, “Directional Couplers Using Long-Range Surface Plasmon Polariton Waveguides,” *IEEE Journal of Selected Topics in Quantum Electronics*, vol. 12, no. 6, pp. 1233–1241, 2006, doi: 10.1109/JSTQE.2006.882659.

[70] D. Sarid, “Long-Range Surface-Plasma Waves on Very Thin Metal Films,” *Physical Review Letters*, vol. 47, no. 26, pp. 1927–1930, 1981, doi: 10.1103/PhysRevLett.47.1927.

[71] L. Wendler and R. Haupt, “Long-range surface plasmon-polaritons in asymmetric layer structures,” *Journal of Applied Physics*, vol. 59, no. 9, pp. 3289–3291, May 1986, doi: 10.1063/1.336884.

[72] J. M. Montgomery and S. K. Gray, “Enhancing surface plasmon polariton propagation lengths via coupling to asymmetric waveguide structures,” *Physical Review B - Condensed Matter and Materials Physics*, vol. 77, no. 12, pp. 1–9, 2008, doi: 10.1103/PhysRevB.77.125407.

[73] F. Liu, Y. Rao, Y. Huang, W. Zhang, and J. Peng, “Coupling between long range surface plasmon polariton mode and dielectric waveguide mode,” *Applied Physics Letters*, vol. 90, no. 14, pp. 1–4, 2007, doi: 10.1063/1.2719169.

[74] R. F. Oulton, V. J. Sorger, D. a. Genov, D. F. P. Pile, and X. Zhang, “A hybrid plasmonic waveguide for subwavelength confinement and long-range propagation,” *Nature Photonics*, vol. 2, no. 8, pp. 496–500, 2008, doi: 10.1038/nphoton.2008.131.

[75] R. Salvador, A. Martínez, C. García-Meca, R. Ortuño, and J. Martí, “Analysis of hybrid dielectric plasmonic waveguides,” *IEEE Journal on Selected Topics in Quantum Electronics*, vol. 14, no. 6, pp. 1496–1501, 2008, doi: 10.1109/JSTQE.2008.920035.

[76] P. Berini and I. de Leon, “Surface plasmon-polariton amplifiers and lasers,” *Nature Photonics*, vol. 6, no. 1. pp. 16–24, Jan. 2012, doi: 10.1038/nphoton.2011.285.

[77] M. Z. Alam, J. S. Aitchison, and M. Mojahedi, “Compact and silicon-on-insulator-compatible hybrid plasmonic TE-pass polarizer,” *Optics Letters*, vol. 37, no. 1, p. 55, 2012, doi: 10.1364/OL.37.000055.

[78] O. Hess, J. B. Pendry, S. A. Maier, R. F. Oulton, J. M. Hamm, and K. L. Tsakmakidis, “Active nanoplasmonic metamaterials,” *Nature Materials*, vol. 11, no. 7. Nature Publishing Group, pp. 573–584, 2012, doi: 10.1038/nmat3356.

[79] M. T. Hill, “Electrically pumped metallic and plasmonic nanolasers,” *Chinese Physics B*, vol. 27, no. 11. Institute of Physics Publishing, p. 114210, 2018, doi: 10.1088/1674-1056/27/11/114210.

[80] J. Cuerda, F. Ruting, F. J. Garcia-Vidal, and J. Bravo-Abad, “Lasing action in active plasmonic structures,” in *2015 9th International Congress on Advanced Electromagnetic Materials in Microwaves and Optics, METAMATERIALS 2015*, Nov. 2015, pp. 34–36, doi: 10.1109/MetaMaterials.2015.7342449.

[81] F. Rüting, J. Cuerda, J. Bravo-Abad, and F. J. Garcia-Vidal, “Lasing action assisted by long-range surface plasmons,” *Laser and Photonics Reviews*, vol. 8, no. 5, 2014, doi: 10.1002/lpor.201400052.

[82] B. Sun, Y. Wang, Y. Liu, S. Liu, C. Liao, and M.-Y. Chen, “Compact device employed a hybrid plasmonic waveguide for polarization-selective splitting,” *Optics Communications*, vol. 334, pp. 240–246, 2015, doi: 10.1016/j.optcom.2014.08.014.

[83] B. Fan *et al.*, “Integrated refractive index sensor based on hybrid coupler with short range surface plasmon polariton and dielectric waveguide,” *Sensors and Actuators, B: Chemical*, vol. 186, pp. 495–505, 2013, doi: 10.1016/j.snb.2013.06.005.

[84] T. Holmgaard and S. I. Bozhevolnyi, “Theoretical analysis of dielectric-loaded surface plasmon-polariton waveguides,” *Physical Review B - Condensed Matter and Materials Physics*, vol. 75, no. 24, pp. 1–12, 2007, doi: 10.1103/PhysRevB.75.245405.

[85] E. Marcatili, “Improved coupled-mode equations for dielectric guides,” *IEEE Journal of Quantum Electronics*, vol. 22, no. 6, pp. 988–993, 1986, doi: 10.1109/JQE.1986.1073042.

[86] A. Degiron and D. Smith, “Numerical simulations of long-range plasmons.,” *Optics express*, vol. 14, no. 4, pp. 1611–1625, 2006, doi: 10.1364/OE.14.001611.

[87] P. Crystal, K. Saitoh, M. Koshiba, and S. Member, “Full-Vectorial Imaginary-Distance Beam Propagation Method Based on a Finite Element Scheme :,” *IEEE Journal of Quantum Electronics*, vol. 38, no. 7, pp. 927–933, 2002, doi: 10.1109/JQE.2002.1017609.

[88] Z. X. Chen, Z. J. Wu, Y. Ming, X. J. Zhang, and Y. Q. Lu, “Hybrid plasmonic waveguide in a metal V-groove,” *AIP Advances*, vol. 4, no. 1, pp. 0–7, 2014, doi: 10.1063/1.4861582.

[89] V. a. Zenin, V. S. Volkov, Z. Han, S. I. Bozhevolnyi, E. Devaux, and T. W. Ebbesen, “Directional coupling in channel plasmon-polariton waveguides,” *Optics Express*, vol. 20, no. 6, p. 6124, 2012, doi: 10.1364/OE.20.006124.

[90] E. Ozbay, “Plasmonics: merging photonics and electronics at nanoscale dimensions.,” *Science (New York, N.Y.)*, vol. 311, no. 5758, pp. 189–193, 2006, doi: 10.1126/science.1114849.

[91] Q. Wang, G. Farrell, and T. Freir, “Theoretical and experimental investigations of macro-bend losses for standard single mode fibers,” *Optics Express*, vol. 13, no. 12, p. 4476, Jun. 2005, doi: 10.1364/OPEX.13.004476.

[92] G. Ghosh, “Sellmeier coefficients and dispersion of thermo-optic coefficients for some optical glasses,” *Applied Optics*, vol. 36, no. 7, p. 1540, Mar. 1997, doi: 10.1364/ao.36.001540.

[93] P. G. Etchegoin, E. C. le Ru, and M. Meyer, “An analytic model for the optical properties of gold,” *The Journal of Chemical Physics*, vol. 125, no. 16, p. 164705, Oct. 2006, doi: 10.1063/1.2360270.

[94] J. N. Reddy, “An Introduction to the Finite Element Method, 3rd Edition-McGraw-Hill Education (ISE Editions).” McGraw-Hill Education: New York, Chicago, San Francisco, Athens, London, Madrid, Mexico City, Milan, New Delhi, Singapore, Sydney, Toronto, p. 763, 2005, Accessed: May 12, 2020. [Online].

[95] J. Zhang, L. Zhang, and W. Xu, “Surface plasmon polaritons: physics and applications,” *J. Phys. D: Appl. Phys.*, vol. 45, p. 113001, 2012.

[96] D. R. Tilley, “Surface Polaritons: Electromagnetic Waves at Surfaces and Interfaces,” *Optica Acta: International Journal of Optics*, vol. 30, no. 11, pp. 1501–1501, Nov. 1983, doi: 10.1080/713821096.

[97] E. Kretschmann and H. Raether, “Radiative Decay of Non Radiative Surface Plasmons Excited by Light,” 1968. Accessed: Apr. 19, 2020. [Online].

[98] A. Otto, “Excitation of nonradiative surface plasma waves in silver by the method of frustrated total reflection,” *Zeitschrift für Physik*, vol. 216, no. 4, pp. 398–410, Aug. 1968, doi: 10.1007/BF01391532.

[99] L. Lévesque and B. E. Paton, “Detection of defects in multiple-layer structures by using surface plasmon resonance,” *Applied Optics*, vol. 36, no. 28, p. 7199, Oct. 1997, doi: 10.1364/ao.36.007199.

[100] J. Homola, S. S. Yee, and G. Gauglitz, “Surface plasmon resonance sensors: review,” *Sensors and Actuators, B: Chemical*, vol. 54, no. 1, pp. 3–15, 1999, doi: 10.1016/S0925-4005(98)00321-9.

[101] J. Grandidier *et al.*, “Dielectric-loaded surface plasmon polariton waveguides on a finite-width metal strip,” *Applied Physics Letters*, vol. 96, no. 6, pp. 2010–2013, 2010, doi: 10.1063/1.3300839.

[102] E. K. Sharma and M. P. Singh, “Multilayer waveguide devices with absorbing layers: An exact analysis,” *Journal of Optical Communications*, vol. 14, no. 4, pp. 134–137, 1993, doi: 10.1515/JOC.1993.14.4.134.

[103] E. Anemogiannis, E. N. Glytsis, and T. K. Gaylord, “Efficient Solution of Eigenvalue Equations of Optical Waveguiding Structures,” *Journal of Lightwave Technology*, vol. 12, no. 12, pp. 2080–2084, 1994, doi: 10.1109/50.350624.

[104] a a Stratonnikov, a P. Bogatov, a E. Drakin, and F. F. Kamenets, “A semianalytical method of mode determination for a multilayer planar optical

waveguide," *Journal of Optics A: Pure and Applied Optics*, vol. 4, no. 5, pp. 535–539, 2002, doi: 10.1088/1464-4258/4/5/308.

[105] M. S. Kwon, "A numerically stable analysis method for complex multilayer waveguides based on modified transfer-matrix equations," *Journal of Lightwave Technology*, vol. 27, no. 20, pp. 4407–4414, 2009, doi: 10.1109/JLT.2009.2024089.

[106] M. S. Kwon and S. Y. Shin, "Simple and fast numerical analysis of multilayer waveguide modes," *Optics Communications*, vol. 233, no. 1–3, pp. 119–126, Mar. 2004, doi: 10.1016/j.optcom.2004.01.037.

[107] Z. Wang, X. Cao, A. Ma, Y. Li, and Q. Zhou, "Analytical solution of metal nanowires at visible and near-infrared wavelength," *Progress In Electromagnetics Research M*, vol. 63, pp. 47–58, 2018, doi: 10.2528/PIERM17091403.

[108] R. K. Verma and B. D. Gupta, "Surface plasmon resonance based U-shaped fiber optic sensor with enhanced sensitivity," 2009.

[109] X. Wang, C. Yin, and Z. Cao, "Transfer Matrix Method and the Graded-Index Waveguide," 2016, pp. 17–42.

[110] A. K. Ghatak, K. Thyagarajan, and M. R. Shenoy, "Numerical Analysis of Planar Optical Waveguides Using Matrix Approach," *Journal of Lightwave Technology*, vol. 5, no. 5, pp. 660–667, 1987, doi: 10.1109/JLT.1987.1075553.

[111] A. Hassani and M. Skorobogatiy, "Design criteria for microstructured-optical-fiber-based surface-plasmon-resonance sensors," *Journal of the Optical Society of America B*, vol. 24, no. 6, p. 1423, 2007, doi: 10.1364/JOSAB.24.001423.

[112] A. Hassani, B. Gauvreau, M. F. Fehri, A. Kabashin, and M. Skorobogatiy, "Photonic Crystal Fiber and Waveguide-Based Surface Plasmon Resonance Sensors for Application in the Visible and Near-IR," *Electromagnetics*, vol. 28, no. 3, pp. 198–213, 2008, doi: 10.1080/02726340801921627.

[113] A. Hassani and M. Skorobogatiy, "Design of the microstructured optical fiber-based surface plasmon resonance sensors with enhanced microfluidics," *Optics Express*, vol. 14, no. 24, p. 11616, 2006, doi: 10.1364/oe.14.011616.

[114] T. M. Monro *et al.*, "Sensing with suspended-core optical fibers," *Optical Fiber Technology*, vol. 16, no. 6, pp. 343–356, Dec. 2010, doi: 10.1016/j.yofte.2010.09.010.

[115] F. M. Cox, R. Lwin, M. C. J. Large, and C. M. B. Cordeiro, "Opening up optical fibres," *Optics Express*, vol. 15, no. 19, p. 11843, Sep. 2007, doi: 10.1364/oe.15.011843.

[116] R. Kostecki, H. Ebendorff-Heidepriem, C. Davis, G. McAdam, S. C. Warren-Smith, and T. M. Monro, “Silica exposed-core microstructured optical fibers,” *Optical Materials Express*, vol. 2, no. 11, p. 1538, Nov. 2012, doi: 10.1364/ome.2.001538.

[117] P. G. Etchegoin, E. C. le Ru, and M. Meyer, “An analytic model for the optical properties of gold,” *Journal of Chemical Physics*, vol. 125, no. 16, p. 164705, Oct. 2006, doi: 10.1063/1.2360270.

[118] D. J. J. Hu and H. P. Ho, “Recent advances in plasmonic photonic crystal fibers: design, fabrication and applications,” *Adv. Opt. Photon.*, vol. 9, pp. 257–314, 2017.

[119] A. Csaki *et al.*, “Nanoparticle layer deposition for plasmonic tuning of microstructured optical fibers,” *Small*, vol. 6, no. 22, pp. 2584–2589, Nov. 2010, doi: 10.1002/smll.201001071.

[120] N. Luan and J. Yao, “Surface plasmon resonance sensor based on exposed-core microstructured optical fiber placed with a silver wire,” *IEEE Photonics Journal*, vol. 8, no. 1, Feb. 2016, doi: 10.1109/JPHOT.2015.2514038.

[121] N. Luan, R. Wang, W. Lv, and J. Yao, “Surface plasmon resonance sensor based on D-shaped microstructured optical fiber with hollow core.,” *Optics express*, vol. 23, no. 7, pp. 8576–82, Apr. 2015, doi: 10.1364/OE.23.008576.

[122] R. Otupiri, E. K. Akowuah, and S. Haxha, “Multi-channel SPR biosensor based on PCF for multi-analyte sensing applications,” *Optics Express*, vol. 23, no. 12, p. 15716, Jun. 2015, doi: 10.1364/oe.23.015716.

[123] N. M. Y. Zhang *et al.*, “Design and analysis of surface plasmon resonance sensor based on high-birefringent microstructured optical fiber,” *Journal of Optics*, vol. 18, no. 6, p. 065005, May 2016, doi: 10.1088/2040-8978/18/6/065005.

[124] X. Yang, Y. Lu, M. Wang, and J. Yao, “An Exposed-Core Grapefruit Fibers Based Surface Plasmon Resonance Sensor,” *Sensors*, vol. 15, pp. 17106–17114, 2015.

[125] S. Ge, F. Shi, G. Zhou, S. Liu, Z. Hou, and L. Peng, “U-Shaped Photonic Crystal Fiber Based Surface Plasmon Resonance Sensors,” *Plasmonics*, vol. 11, no. 5, pp. 1307–1312, Oct. 2016, doi: 10.1007/s11468-015-0176-z.

[126] C. Liu *et al.*, “Design and theoretical analysis of a photonic crystal fiber based on surface plasmon resonance sensing,” *Journal of Nanophotonics*, vol. 9, no. 1, p. 093050, Sep. 2015, doi: 10.1117/1.jnp.9.093050.

[127] T. Nikolajsen, K. Leosson, and S. I. Bozhevolnyi, “In-line extinction modulator based on long-range surface plasmon polaritons,” *Opt. Comm.*, vol. 244, pp. 455–459, 2005.

[128] J. T. Kim, J. J. Ju, S. Park, M. Kim, S. K. Park, and S.-Y. Shin, “Hybrid plasmonic waveguide for low-loss lightwave guiding,” *Opt. Express*, vol. 18, pp. 2808–2813, 2010.

[129] M. Z. Alam, J. S. Aitchison, and M. Mojahedi, “Compact and silicon-on-insulator-compatible hybrid plasmonic TE-pass polarizer,” *Optics Letters*, vol. 37, no. 1, p. 55, 2012, doi: 10.1364/OL.37.000055.

[130] B. Fan, F. Liu, R. Wan, Y. Huang, Y. Miura, and D. Ohnishi, “Hybrid Coupler with Short Range Surface Plasmon Polariton and Dielectric Waveguide,” in *Passive Components and Fiber-Based Devices*, 2011, p. 830708.

[131] J. K. Li *et al.*, “Broadband solar energy absorber based on monolayer molybdenum disulfide using tungsten elliptical arrays.,” *Mater. Today Energy*, vol. 16, p. 100390, 2020.

[132] A. v Dyshlyuk, O. B. Vitrik, and U. A. Eryusheva, “Waveguide-Based Refractometers Using Bulk, Long-and Short-Range Surface Plasmon Modes: Comparative Study,” *J. Lightwave Technol.*, vol. 36, pp. 5319–5326, 2018.

[133] R. Osgood *et al.*, “Nonlinear Plasmonics,” *Nat. Photon.*, vol. 6, no. October, pp. 737–748, 2009.

[134] X. Wang, C. Yin, and Z. Cao, *Progress in Planar Optical Waveguides*. Berlin, Heidelberg: Springer Berlin Heidelberg, 2016.

[135] A. W. Snyder and J. D. Love, *Optical Waveguide Theory*. Boston, MA: Springer US, 1984.

[136] N. Gomez-Cardona, E. Reyes-Vera, C. Jimenez-Durango, J. Usuga-Restrepo, and P. Torres, “Novel Wide-Bandwidth Polarization Filter Based on H-Shaped Micro-Structured Optical Fiber with Gold Nano-strip,” in *2018 International Conference on Electromagnetics in Advanced Applications (ICEAA)*, Sep. 2018, pp. 538–541.

[137] D. K. C. Wu, B. T. Kuhlmey, and B. J. Eggleton, “Ultrasensitive photonic crystal fiber refractive index sensor,” *Opt. Lett.*, vol. 34, pp. 322–324, 2009.

[138] Y. Peng, J. Hou, Y. Zhang, Z. Huang, R. Xiao, and Q. Lu, “Temperature sensing using the bandgap-like effect in a selectively liquid-filled photonic crystal fiber,” *Opt. Lett.*, vol. 38, pp. 263–265, 2013.

[139] C. Du, Q. Wang, H. Hu, and Y. Zhao, “Highly Sensitive Refractive Index Sensor Based on Four-Hole Grapefruit Microstructured Fiber with Surface Plasmon Resonance,” *Plasmonics*, no. February 2018, 2016, doi: 10.1007/s11468-016-0468-y.

[140] X. Yang, Y. Lu, B. Liu, and J. Yao, “Analysis of Graphene-Based Photonic Crystal Fiber Sensor Using Birefringence and Surface Plasmon Resonance,” *Plasmonics*, vol. 12, pp. 489–496, 2017.

[141] Y.-X. Jiang, B.-H. Liu, X.-S. Zhu, X.-L. Tang, and Y.-W. Shi, “Long-range surface plasmon resonance sensor based on dielectric/silver coated hollow fiber with enhanced figure of merit,” *Opt. Lett.*, vol. 40, pp. 744–747, 2015.

[142] N. D. Gomez-Cardona, E. Reyes-Vera, and P. I. Torres, “Multi-Plasmon Resonances in Microstructured Optical Fibers: Extending the Detection Range of SPR Sensors and a Multi-Analyte Sensing Technique,” *IEEE Sens. J.*, vol. 18, pp. 7492–7498, 2018.

[143] A. A. Rifat, R. Ahmed, G. A. Mahdiraji, and F. R. M. Adikan, “Highly Sensitive D-Shaped Photonic Crystal Fiber-Based Plasmonic Biosensor in Visible to Near-IR,” *IEEE Sens. J.*, vol. 17, pp. 2776–2783, 2017.

[144] N. D. Gómez-Cardona, E. Reyes-Vera, P. Torres, E. Reyes-Vera, and P. Torres, “Multi-analyte refractive index sensor based on hybrid long range plasmon modes in H-shaped optical fiber,” in *Latin America Optics and Photonics Conference*, Nov. 2018, p. Tu5B.4.

[145] N. D. Gomez-Cardona, E. Reyes-Vera, and P. I. Torres, “Multi-Plasmon Resonances in Microstructured Optical Fibers: Extending the Detection Range of SPR Sensors and a Multi-Analyte Sensing Technique,” *IEEE Sensors Journal*, vol. 18, no. 18, pp. 7492–7498, Sep. 2018, doi: 10.1109/JSEN.2018.2861709.

[146] E.-Georg. Neumann, *Single-Mode Fibers : Fundamentals*. Springer Berlin Heidelberg, 1988.

[147] S. Tang *et al.*, “Effective-medium theory for one-dimensional gratings,” *Phys. Rev. B*, vol. 91, p. 174201, 2015.

[148] P. Lalanne, “Effective medium theory applied to photonic crystals composed of cubic or square cylinders,” *Appl. Opt.*, vol. 35, pp. 5369–5380, 1996.

[149] J.-Y. Jing, Q. Wang, W.-M. Zhao, and B.-T. Wang, “Long-range surface plasmon resonance and its sensing applications: A review,” *Opt. and Lasers Eng.*, vol. 112, pp. 103–118, 2019.

[150] S. Jetté-Charbonneau, R. Charbonneau, N. Lahoud, G. Mattiussi, and P. Berini, “Demonstration of Bragg gratings based on long-ranging surface plasmon polariton waveguides.,” *Opt. Express*, vol. 13, pp. 4674–4682, 2005.

[151] Md. S. Islam *et al.*, “Dual-polarized highly sensitive plasmonic sensor in the visible to near-IR spectrum,” *Opt. Express*, vol. 26, pp. 30347–30361, 2018.

[152] T. Hu, Y. Zhao, and A. Song, “Fiber optic SPR sensor for refractive index and temperature measurement based on MMF-FBG-MMF structure,” *Sensors and Actuators B: Chem*, pp. 521–525, 2016.

[153] M. Y. Azab, M. Farhat. O. Hameed, and S. S. A. Obayya, “Multi-functional optical sensor based on plasmonic photonic liquid crystal fibers,” *Opt. Quantum Electron*, vol. 49, p. 49, 2017.

[154] X. Feng *et al.*, “Multi-functional optical sensor based on plasmonic photonic liquid crystal fibers,” *Opt. Quantum Electron.*, vol. 49, pp. 1–12, 2017.

[155] W. Zhang, Z. Lian, T. Benson, X. Wang, and S. Lou, “A refractive index sensor based on a D-shaped photonic crystal fiber with a nanoscale gold belt.,” *Opt. Quantum Electron.*, vol. 50, pp. 1–12, 2018.

[156] T. Khanikar and V. K. Singh, “Gold grating assisted SPR based D-shaped single mode fiber for detection of liquid refractive index.,” *Opt. Quantum Electron.*, vol. 51, pp. 1–10, 2019.

[157] X. Zhao, X. Zhang, X.-S. Zhu, and Y.-W. Shi, “Long-range surface plasmon resonance sensor based on the GK570/Ag coated hollow fiber with an asymmetric layer structure.,” *Opt. Express*, vol. 27, p. 9550, 2019.

[158] Q. Wang, J.-Y. Jing, X.-Z. Wang, L.-Y. Niu, and W.-M. Zhao, “A D-shaped Fiber Long-range Surface Plasmon Resonance Sensor with High Q-factor and Temperature Self-compensation.,” *IEEE Trans. Instrum. Meas.*, vol., p. 1, 2019.

[159] Q. Wang, J. Y. Jing, W. M. Zhao, X. C. Fan, and X. Z. Wang, “A Novel Fiber-Based Symmetrical Long-Range Surface Plasmon Resonance Biosensor with High Quality Factor and Temperature Self-Reference.,” *IEEE Trans. Nanotechnol.*, vol. 18, pp. 1137–1143, 2019.

[160] R. W. Tkach, “Scaling optical communications for the next decade and beyond,” *Bell Labs Technical Journal*, vol. 14, no. 4, pp. 3–9, Feb. 2010, doi: 10.1002/bltj.20400.

[161] D. J. Richardson, J. M. Fini, and L. E. Nelson, “Space-division multiplexing in optical fibres,” *Nature Photonics*, vol. 7, no. 5, pp. 354–362, May 2013, doi: 10.1038/nphoton.2013.94.

[162] X. Fang and R. O. Claus, “Polarization-independent all-fiber wavelength-division multiplexer based on a Sagnac interferometer,” *Optics Letters*, vol. 20, no. 20, p. 2146, Oct. 1995, doi: 10.1364/OL.20.002146.

[163] W. Xiong, C. W. Hsu, Y. Bromberg, J. E. Antonio-Lopez, R. Amezcua Correa, and H. Cao, “Complete polarization control in multimode fibers with polarization and

mode coupling," *Light: Science and Applications*, vol. 7, no. 1, pp. 1–10, 2018, doi: 10.1038/s41377-018-0047-4.

[164] C.-C. Huang, "Numerical investigations of an ultra-compact polarization beam splitter based on augmented low-index guiding and subwavelength grating structures," *Scientific Reports*, vol. 8, no. 1, p. 17338, Dec. 2018, doi: 10.1038/s41598-018-35841-2.

[165] S. Zhang, W. Zhang, P. Geng, X. Li, and J. Ruan, "Design of single-polarization wavelength splitter based on photonic crystal fiber," *Applied Optics*, vol. 50, no. 36, p. 6576, Dec. 2011, doi: 10.1364/AO.50.006576.

[166] K. Saitoh, Y. Sato, and M. Koshiba, "Polarization splitter in three-core photonic crystal fibers," *Optics Express*, vol. 12, no. 17, p. 3940, 2004, doi: 10.1364/OPEX.12.003940.

[167] T. Zhao, S. Lou, X. Wang, M. Zhou, and Z. Lian, "Ultrabroadband polarization splitter based on three-core photonic crystal fiber with a modulation core," *Applied Optics*, vol. 55, no. 23, p. 6428, Aug. 2016, doi: 10.1364/AO.55.006428.

[168] J. Wang, L. Pei, S. Weng, L. Wu, J. Li, and T. Ning, "Ultrashort polarization beam splitter based on liquid-filled dual-core photonic crystal fiber," *Applied Optics*, vol. 57, no. 14, p. 3847, May 2018, doi: 10.1364/AO.57.003847.

[169] Z. Zhang, Y. Tsuji, M. Eguchi, and C. Chen, "Design of polarization converter based on photonic crystal fiber with anisotropic lattice core consisting of circular holes," *Journal of the Optical Society of America B*, vol. 34, no. 10, p. 2227, Oct. 2017, doi: 10.1364/JOSAB.34.002227.

[170] A. Khaleque and H. T. Hattori, "Ultra-broadband and compact polarization splitter based on gold filled dual-core photonic crystal fiber," *Journal of Applied Physics*, vol. 118, no. 14, p. 143101, Oct. 2015, doi: 10.1063/1.4932659.

[171] Z.-K. Fan, S.-G. Li, Y.-Q. Fan, W. Zhang, G.-W. An, and Y.-J. Bao, "Designing analysis of the polarization beam splitter in two communication bands based on a gold-filled dual-core photonic crystal fiber," *Chinese Physics B*, vol. 23, no. 9, p. 94212, Sep. 2014, doi: 10.1088/1674-1056/23/9/094212.

[172] C. Jimenez-Durango, E. Reyes-Vera, and N. Gomez-Cardona, "Ultra-short polarization beam splitter to operate in two communication bands based on a gold-filled dual-core photonic crystal fiber," in *Latin America Optics and Photonics Conference*, 2018, no. c, p. Tu4A.16, doi: 10.1364/LAOP.2018.Tu4A.16.

[173] H. L. Chen, S. G. Li, Z. K. Fan, G. W. An, J. S. Li, and Y. Han, "A Novel Polarization Splitter Based on Dual-Core Photonic Crystal Fiber With a Liquid

Crystal Modulation Core," *IEEE Photonics Journal*, vol. 6, no. 4, pp. 1–9, Aug. 2014, doi: 10.1109/JPHOT.2014.2337874.

[174] E.-L. Wang, H.-M. Jiang, K. Xie, C. Chen, and Z.-J. Hu, "Polarization splitter based on dual core liquid crystal-filled holey fiber," *Journal of Applied Physics*, vol. 120, no. 11, p. 114501, Sep. 2016, doi: 10.1063/1.4962449.

[175] J. Wang *et al.*, "A Tunable Polarization Beam Splitter Based on Magnetic Fluids-Filled Dual-Core Photonic Crystal Fiber," *IEEE Photonics Journal*, vol. 9, no. 1, pp. 1–10, Feb. 2017, doi: 10.1109/JPHOT.2017.2656248.

[176] E. Reyes-Vera, N. D. Gómez-Cardona, G. Chesini, C. M. B. Cordeiro, and P. Torres, "Temperature sensibility of the birefringence properties in side-hole photonic crystal fiber filled with Indium," *Applied Physics Letters*, vol. 105, no. 20, p. 201101, Nov. 2014, doi: 10.1063/1.4902157.

[177] E. Reyes-Vera and P. Torres, "Influence of filler metal on birefringent optical properties of photonic crystal fiber with integrated electrodes," *Journal of Optics*, vol. 18, no. 8, p. 85804, Aug. 2016, doi: 10.1088/2040-8978/18/8/085804.

[178] S. H. Lee, B. H. Kim, and W.-T. Han, "Effect of filler metals on the temperature sensitivity of side-hole fiber," *Optics Express*, vol. 17, no. 12, p. 9712, Jun. 2009, doi: 10.1364/OE.17.009712.

[179] H. W. Lee *et al.*, "Pressure-assisted melt-filling and optical characterization of Au nano-wires in microstructured fibers," *Optics Express*, vol. 19, no. 13, p. 12180, Jun. 2011, doi: 10.1364/OE.19.012180.

[180] T. Muñoz-Hernández, E. Reyes-Vera, and P. Torres, "Tunable Whispering Gallery Mode Photonic Device Based on Microstructured Optical Fiber with Internal Electrodes," *Scientific Reports*, vol. 9, no. 1, p. 12083, Dec. 2019, doi: 10.1038/s41598-019-48598-z.

[181] E. Reyes-Vera, C. M. B. Cordeiro, and P. Torres, "Highly sensitive temperature sensor using a Sagnac loop interferometer based on a side-hole photonic crystal fiber filled with metal," *Applied Optics*, vol. 56, no. 2, p. 156, Jan. 2017, doi: 10.1364/AO.56.000156.

[182] N. P. Bansal, *Handbook of Glass Properties*, First Edit. Orlando, Florida: Academic Press, 1986.

[183] G. Chesini, J. H. Osorio, V. A. Serrao, M. A. R. Franco, and C. M. B. Cordeiro, "Metal-Filled Embedded-Core Capillary Fibers as Highly Sensitive Temperature Sensors," *IEEE Sensors Letters*, vol. 2, no. 2, pp. 1–4, Jun. 2018, doi: 10.1109/LSENS.2018.2815586.

[184] M. Fokine *et al.*, “Integrated fiber Mach–Zehnder interferometer for electro-optic switching,” *Optics Letters*, vol. 27, no. 18, p. 1643, Sep. 2002, doi: 10.1364/OL.27.001643.

[185] V. H. Arístizabal, F. J. Vélez, E. Rueda, N. D. Gómez, and J. A. Gómez, “Numerical modeling of fiber specklegram sensors by using finite element method (FEM),” *Optics Express*, vol. 24, no. 24, p. 27225, Nov. 2016, doi: 10.1364/OE.24.027225.

[186] K. Saitoh, Y. Sato, and M. Koshiba, “Coupling characteristics of dual-core photonic crystal fiber couplers.,” *Optics express*, vol. 11, no. 24, pp. 3188–3195, Dec. 2003, [Online]. Available: http://www.ncbi.nlm.nih.gov/pubmed/19471444.

[187] D. L. Lee, *Electromagnetic Principles of Integrated Optics*, 1st Editio. Wiley, 1986.

[188] A. W. Snyder and J. D. Love, *Optical Waveguide Theory*. Boston, MA: Springer US, 1984.

[189] E. Reyes-Vera, J. Usuga-Restrepo, C. Jimenez-Durango, J. Montoya-Cardona, and N. Gomez-Cardona, “Design of Low-loss and Highly Birefringent Porous-Core Photonic Crystal Fiber and Its Application to Terahertz Polarization Beam Splitter,” *IEEE Photonics Journal*, vol. 10, no. 4, pp. 1–13, Aug. 2018, doi: 10.1109/JPHOT.2018.2860251.

[190] S. L. A. Carrara, B. Y. Kim, and H. J. Shaw, “Elasto-optic alignment of birefringent axes in polarization-holding optical fiber,” *Optics Letters*, vol. 11, no. 7, p. 470, Jul. 1986, doi: 10.1364/OL.11.000470.

[191] J. F. Botero-Cadavid, J. D. Causado-Buelvas, and P. Torres, “Spectral properties of locally pressed fiber bragg gratings written in polarization maintaining fibers,” *Journal of Lightwave Technology*, vol. 28, no. 9, 2010, doi: 10.1109/JLT.2010.2040804.

[192] X. Wang, S. Li, Q. Liu, Z. Fan, G. Wang, and Y. Zhao, “High-extinction ratio and short-length polarization splitter based on microstructured optical fiber with tellurite glass,” *Optical Materials*, vol. 66, pp. 542–546, Apr. 2017, doi: 10.1016/j.optmat.2017.02.024.